Title
Magnetic Resonance - Ultrasound Fusion of the Prostate: Imaging for Cancer Diagnosis

Author
Natarajan, Shyam

Publication Date
2012

Peer reviewed|Thesis/dissertation

University of California
Los Angeles

Magnetic Resonance – Ultrasound Fusion of the Prostate: Imaging for Cancer Diagnosis

A dissertation submitted in partial satisfaction
of the requirements for the degree
Doctor of Philosophy in Biomedical Engineering

by

Shyam Natarajan

2012

Shyam Natarajan

2012

Abstract of the Dissertation

Magnetic Resonance – Ultrasound Fusion of the Prostate: Imaging for Cancer Diagnosis

by

Shyam Natarajan

Doctor of Philosophy in Biomedical Engineering

University of California, Los Angeles, 2012

Professor Warren Grundfest, Chair

Methods to diagnosis prostate cancer, a disease affecting approximately 240,000 men in the U.S. annually, have remained largely unchanged in the last several decades. An increased level of prostate specific antigen (PSA) is the usual initiating event followed by an ultrasound-guided biopsy. Such biopsies are performed in a systematic, but blind manner, and tumor discovery is often fortuitous. Furthermore, such biopsies often cannot differentiate between serious, potentially lethal forms of prostate cancer and insignificant, indolent forms. This inadequate method of diagnosis has led to over-treatment of indolent disease, a major concern due to the quality-of-life issues of impotence and incontinence associated with curative treatment.

Targeted biopsy utilizing multi-parametric magnetic resonance (MR) imaging may comprise an important advance in prostate cancer diagnosis. MR-guided biopsies, while effective, suffer from high cost, limited availability, and long procedure times. MR-Ultrasound (MR-US) fusion, marrying the predictive accuracy of MR and the real-time capabilities of ultrasound, offers an alternative that can be performed in most outpatient settings, while potentially retaining the cancer detection accuracy of MR-guided biopsy.

This thesis presents comprehensive research studies that validate targeted biopsy using MR-US fusion. We found that the use of image fusion in targeted prostate biopsy yielded an improved cancer detection rate in a low-risk population. Further, we discover that fusion is appropriate for men with prior negative biopsies and elevated levels of prostate specific antigen (PSA), some of whom may be screened using MRI. In men undergoing repeat biopsy to rule out cancer, we observed a cancer detection rate of almost four times that usually reported (37% vs. 10%).

We also discover that significant components to errors in targeting are volume accuracy and registration between MR and TRUS. To this end, this thesis presents a novel method of real-time 3D prostate imaging suitable for image fusion, transurethral ultrasound (TUUS). A number of engineering challenges have been addressed to bring this concept to realization: a catheter-based transducer theoretically capable of volumetric imaging of the prostate was fabricated and evaluated; reconfigurable hardware was designed to provide flexibility in imaging techniques; and image reconstruction techniques were developed and implemented for MR-US fusion.

The dissertation of Shyam Natarajan is approved.

Denise Aberle

Daniel Ennis

E. Carmack Holmes

Leonard Marks

Rahul Singh

Warren Grundfest, Committee Chair

University of California, Los Angeles

2012

This thesis is dedicated to Mom, Dad, Deepak, and Thatha, who have given me endless encouragement and love, and have provided me with the motivation and skills to achieve the very best in life.

Table of Contents

List of Figures

List of Tables

List of Abbreviations

aADC Average Apparent Diffusion Coefficient

AAF Anti-Aliasing Filter

ADC Analog-to-Digital Converter

BPF Band Pass Filter

BPH Benign Prostatic Hyperplasia

CaP Prostate Cancer

CT Computed Tomography

DCE Dynamic Contrast Enhancement

DOF Degree of Freedom

DRE Digital Rectal Exam

DWI Diffusion Weighted Imaging

EC Endorectal Coil

FIFO First-In First-Out

FLE Fiducial Localization Error

FNAB Fine Needle Aspiration Biopsy

FPGA Field Programmable Gate Array

IMRT Intensity-Modulated Radiation Therapy

IVUS Intravascular Ultrasound

LNA Low Noise Amplifier

LPF Low Pass Filters

LVDS Low-Voltage Differential Signaling

MEMS Microelectromechanical Systems

mpMRI Multi-Parametric MRI

MRI Magnetic Resonance Imaging

MR-US Magnetic Resonance - Ultrasound

MUX Multiplexer

NURD Non-Uniform Rotational Distortion

PDMS Polydimethylsiloxane

PET-CT Positron Emission Tomography / Computed Tomography

PET Positron Emission Tomography

PRF Pulse Repetition Frequency

PSA Prostate Specific Antigen

PZT Lead Zirconate Titanate

RALP Robot-Assisted Laparoscopic Radical Prostatectomy

RDIP Reconfigurable Diagnostic Imaging Platform

ROI Region(s) of Interest

SNR Signal-to-Noise Ratio

SPDT Single-Pole Double-Throw

STA Synthetic Transmit Aperture

TNM Tumor, Nodes, Metastases Cancer Staging System

TRE Target Registration Error

T/R Transmit/Receive

TRUS Transrectal Ultrasound

TURP Transurethral Resection of the Prostate

TUUS Transurethral Ultrasound

T2WI T2 Weighted Imaging

USB Universal Serial Bus

Acknowledgments

I would like to thank my advisors, Dr. Warren Grundfest and Dr. Leonard Marks, whose support, knowledge, and vision have been integral to both this project and my graduate education.

I am indebted to Dr. Martin Culjat and Dr. Rahul Singh for their continuous support and guidance on the direction of my research. I am also grateful to Drs. Denise Aberle, Daniel Ennis, E. Carmack Holmes, Hua Lee, Daniel Margolis, Jiaoti Huang, Fred Dorey, Steve Raman, and Robert Reiter for their valuable insights and input on my research.

The outstanding team of clinicians, staff and collaborators, including Malu, Liz, Patricia, Shelena, Dinesh, Ram, Dave, Nelly, Karim, and Geoff.

My fellow graduate students (CASIT and otherwise), including Richard, Pria, Amit, Meg, Chris, Qing, Ken, Omeed, Helena, Neal, Sushini, Drew, Kuo, Kevin, Colin, Dave, Ji, Zach, and Aaron whom have kept me sane during grad school.

The undergraduates and other team members that contributed to the systems development have been invaluable in the completion of this work, including Brian, Anton, Jonathan, Vanessa, Matt, and Apoorva.

Finally, I would like to thank my family as I would have not been able to get this far without their endless encouragement.

Funding for this work was provided by the National Institutes of Health (NIH) under award number 1R01CA158627-1, the Prostate Cancer Research Program (PCRP) award number W81XWH-10-R-0132, the Telemedicine and Advanced Technology Research Center (TATRC) award numbers W81XWH-07-1-0672 and W81XWH-07-1-0668, the Beckman Coulter Foundation, the Stephen C. Gordon Family Foundation, and the Jean Perkins Foundation.

Vita

2004	**Quality Engineering Intern** Hyperion Corp., Sunnyvale, California
2005	**Exchange Research Student**, Dept. of Computer and Mathematical Sciences Tohoku University, Sendai, Japan
2006	**Research Intern**, Dept. of Mechanical Engineering KAIST, Daejeon, Republic of Korea
2007	**B.S. (Computer Engineering)** and **B.A. (Japanese)** Honors: Phi Beta Kappa, Eta Kappa Nu University of California, Santa Barbara
2009	M.S. (**Biomedical Engineering**) Thesis: *Signaling, Detection, and Imaging in Medical Ultrasound using Flexible Transducer Arrays* University of California, Los Angeles
2007–present	**Graduate Student Researcher**, Dept. of Bioengineering University of California, Los Angeles

Publications and Presentations

Natarajan S, Marks LS, Margolis DM, Huang J, Macairan M, Lieu P, Fenster A, *Clinical application of a 3D ultrasound-guided prostate biopsy system.* Urologic Oncology, 29(4), 2011.

Shkel A, **Natarajan S**, Schimpf S, Culjat MO, Brose A, Boese A, Schmidt B, Schulam PG, Lee H, Grundfest WS, Singh RS, "A transurethral catheter-based ultrasound system for multi-modal fusion," Medicine Meets Virtual Reality 19, 8 - 11 February 2012, Newport Beach, CA, 2012.

Natarajan S, Narayanan R, Kumar D, Margolis D, Ward A, Fenster A, Marks LS, 'MR-TRUS registration accuracy for targeted biopsy of the prostate," Engineering and Urology, 14 - 19 May 2011, Washington, DC, 2011.

Natarajan S, Singh RS, Lee M, Cox BP, Culjat MO, Grundfest WS, Lee H, "Accurate step-FMCW ultrasound ranging and comparison with pulse-echo signaling methods," SPIE Medical Imaging, 13 - 18 February 2010, San Diego, CA, 2010.

Natarajan S, Singh RS, Lee M, Cox BP, Culjat MO, Lee H, Grundfest WS, "Step-FMCW signaling and target detection for ultrasound imaging systems with conformal transducer arrays," SPIE BIOS: Advanced Biomedical and Clinical Diagnostic Systems VIII, 23 - 28 January 2010, San Francisco, CA, 2010.

Singh RS, **Natarajan S**, Lee M, Dann AE, Cox BP, Lee H, Grundfest WS, Culjat MO, "Development of an ultrasound imaging system for needle guidance," IEEE Ultrasonics Symposium, 20 - 23 September 2009, Rome, Italy, 2009.

Singh RS, Culjat MO, Lee M, Bennett DB, **Natarajan S**, Cox BP, Brown ER, Grundfest WS, Lee H, "Conformal ultrasound imaging system," Acoustical Imaging 30, 1 - 4 March 2009, Monterrey, CA, 2009.

Chapter 1

Introduction

Prostate cancer (CaP) is the commonest internal malignancy among U.S. males. During 2011, an estimated 240,890 patients were diagnosed with cancer, and 33,720 deaths occurred [1]. In contrast, more than 50% of men with newly diagnosed cancers appear to have 'insignificant' lesions of no clinical impact, yet 90% choose active treatment [2]. Treatment decisions are often based on anxiety and perceived threat rather than on a factual assessment of disease potential [3–5]. Thus, due to present diagnostic shortcomings, an important challenge in CaP management has emerged. Today, over-diagnosis and over-treatment of low-risk CaP are as concerning as diagnosing and treating cancer too late [6].

Today, virtually all diagnoses of CaP are accomplished in the same way: a blood test for prostate specific antigen (PSA), a rectal examination (DRE), and tissue-confirmed pathology through an ultrasound-guided biopsy. While fatal when far advanced, CaP is currently diagnosed in an indolent form which may not require treatment. Moreover, a paradox exists between the poor methods of diagnosis, and the over-treatment of non-lethal disease. Together, they contribute to over $1 billion in direct costs annually in the US alone.

Medical imaging, while heralded for its superior diagnostic ability in other forms of cancer, remains underutilized in the prostate. Transrectal ultrasound (TRUS), which has been investigated for nearly half a century, is currently the main imaging tool available to urologists. Yet, TRUS suffers from poor diagnostic sensitivity and is

used primarily for needle guidance during biopsy and therapeutic seed placement. The poor accuracy has lead to a large and growing group of men, who face the possibility of repeat biopsy in the future. In order for an accurate diagnosis to be made, both the *location* and *severity* of any cancer should be known. Recent advances in magnetic resonance imaging (MRI), show promise as a cancer diagnosis method, but clinical use of multi-parametric MRI has remained limited.

This thesis presents a method, MR-Ultrasound (MR-US) fusion, for using imaging to improve CaP diagnosis through targeted biopsy. Validation studies of this fusion technique are presented, as well as clinical studies which use targeted biopsy in a low-risk patient population (n=171). Advantages and limitations of this method are discussed, and an alternative method of imaging which aims to improve fusion is explored.

This imaging technique, transurethral (TUUS) is directly compared with existing ultrasound technology. Finally, the design and validation of an optimal prostate imaging system is described. This system builds off the knowledge gained in both the clinical targeted biopsy and the TUUS validation studies, and aims to improve the utility of MR-US fusion of the prostate.

1.1 Overview of Chapters

This thesis investigates a new method of CaP diagnosis, targeted biopsy. A clinical trial is is conducted and analyzed for improvements in targeted diagnosis of cancer. The current limitations of this method are explored and culminate in a new imaging system, utilizing transurethral ultrasound, designed for MR-US fusion of the prostate.

Chapter Two: Prostate Cancer Diagnosis

Chapter two begins by detailing the history of CaP diagnosis. Each method is introduced and their relative effectiveness is discussed. The current challenges of CaP diagnosis are then presented, with an introduction to imaging techniques which may be used to improve accuracy. While each prostate imaging method has a purpose, there is no single test or scan that can definitely give a positive or negative diagnosis. In the case of MRI, any number of principle components, or *parameters*, are acquired, which can include diffusion-weighted imaging, dynamic contrast enhancement, T1- and T2-weighted imaging, and spectroscopy. Rather than restrict interpretation to a single parameter, the aggregate is analyzed, defined by the term *multi-parametric* MRI (mpMRI). Use of mpMRI can give a more complete picture in the aid of diagnosis. This is in essence the basis for this thesis; data from multiple images, when fused together, can provide clinical information which is more meaningful than any single imaging method alone.

Next, the use of multiple imaging modalities to target suspicious areas is discussed. The use of multi-modal image fusion only requires some way of co-localizing information in each image. This co-localization, or *registration*, can be achieved either through visual inspection of corresponding landmarks (called "mental registration"), or more commonly, through the use of software. This chapter also introduces existing systems that facilitate targeted cancer diagnosis.

Building off previous discussions of the advantages of MRI, direct MR-guided biopsy systems are introduced, along with their relative effectiveness. MR-Ultrasound registration is discussed which fuses real-time ultrasound with a previously-acquired MRI. A number of systems that employ MR-US fusion currently exist, each with a different needle tracking method. The various types of tracking are compared with each other, as well the insertion method: transrectal or transperineal.

Chapter Three: Image Fusion for CaP Diagnosis

This chapter introduces the methods with which to perform MR-US fusion during prostate biopsy. This chapter begins by introducing the basis for improving CaP diagnosis through image fusion, specifically with MR-US software registration. Currently, diagnosis requires a physical tissue sample through biopsy. In MR-US fusion, we target suspicious areas which are assigned prospective grades based on MR characteristics. 12-core systematic biopsy is also acquired which allows direct comparison between traditional, random systematic and targeted biopsy. Prior to implementation in a clinical trial, we examine each component of MR-US fusion and test its accuracy and limitations, including the MR imaging technique and MR-US registration.

Chapter Four: A Clinical Implementation of MR-US fusion

The main part of this section is the various clinical studies performed using image fusion to target CaP. Overall efficacy of MR-TRUS fusion in CaP diagnosis is given, with results from human trials (n=171). Cancer detection rates are examined with relation to clinical factors (age, PSA, prior biopsy, prostate volume, etc), MR characteristics of suspicious areas, and 3D targeting methods. True cancer incidence in this patient population is derived from data on patients who eventually received prostate surgery. The prostate specimens were processed using a technique which allows for the entire gland to fit on large-form glass slides, enabling anatomical correlation with MRI.

Finally, the chapter explores the contributing sources of error and discusses how improvements could potentially improve the efficiency of the fusion technique. A case is made for fusion as an effective and accurate diagnosis tool, noting how many treatments could be avoided through the use of this technology.

Chapter Five: Transurethral Prostate Ultrasound

Previous findings associated with poor transrectal ultrasound (TRUS) visualization are reexamined in this chapter. Calculi, rectal tissue, and large prostatic volumes are barriers to accurate TRUS imaging. This chapter explores the limitations of TRUS imaging in visualization and image fusion, and proposes a new method of prostate imaging using transurethral ultrasound (TUUS). We hypothesized that TUUS improves prostatic visualization, registration accuracy, and clinical utility over TRUS. In this mode, imaging is performed by a catheter-based probe from within the prostatic urethra.

After prior explorations of intraprostatic imaging are summarized, this chapter presents TUUS studies using an existing intravascular ultrasound (IVUS) system, comprising of a 64 element radially-phased transducer array contained within 8.2F catheter. Feasibility of 3D imaging, using a reconstruction technique developed in MATLAB, is presented in comparison to 3D TRUS *in vitro* using tissue-mimicking prostate phantoms. Feasibility of MR-TUUS fusion is explored and the potential advantages over TRUS are discussed. The section concludes by evaluating what parameters for the catheter-based device need to be improved, and establishes benchmarks for an optimal system.

Chapter Six: An Improved Prostate Imaging System

This chapter expands on the previous discussion of TUUS imaging and describes the development of an improved TUUS system for the prostate, using a multi-row, multi-column catheter-based ultrasound transducer. Research on the clinical requirements for MR-US imaging has informed the design of the prostate imaging system.This transducer, designed and fabricated in collaboration with the University of Magdeburg, is constructed using a polyimide substrate, with patterned copper leads. Imag-

ing electronics were also designed to address the issues of versatility and parameter selection with the IVUS system. The design and fabrication of this imaging system are given along with results from validation tests. Signaling, ranging, and then imaging capability is tested using an existing linear transducer array. Characterization of the multi-row, multi-column array transducer is then undertaken and discussed. Finally, results from in-vitro testing of the prototype system is presented along with a comparison with initial design benchmarks, along with a discussion of the error sources.

Chapter 2

Prostate Cancer Diagnosis

In this chapter, imaging techniques are presented, along with anatomical and physiological context. The aim of this chapter is to acquaint the reader with the advantages of each technique and the current and potential clinical uses of each. The fusing of multiple methods are presented as well, along with current devices that perform fusion. There are a number of technologies that aim to directly sample the prostate under MR guidance. This technique is discussed in comparison with a new prostate cancer diagnosis method, MR-Ultrasound fusion.

2.1 Historical Methods of Diagnosis

Prostate cancer, first described in the early 1800's, was initially diagnosed post-mortem as evaluation of the prostate only occurred after death [7]. Diagnosis has historically employed rectal examination, palpating for discrete nodule. Access to the prostate, which is located beneath the bladder, was limited to cases of surgical intervention [7]. However, the past century has given birth to countless CaP screening methods employing tissue sampling, imaging, and blood tests. By tracing the history of newer diagnostic methods, we can gain perspective on current advances.

2.1.1 Digital Rectal Exam

In the early days of prostate cancer diagnosis, screening was performed primarily through the digital rectal examination (DRE). This involved placing a finger against the rectal wall and applying pressure, feeling for any palpable nodules. This method was only capable of identifying large, advanced cancers, and treatment was generally palliative. One study found that the DRE cancer detection rate was poor for both cancer diagnosis and cancer staging [8, 9]. However, the DRE has persisted until the present day, where it remains a clinical indication for further diagnostic procedures. One problem is that DRE results are not very reproducible [10]. This was tested on 116 men with two separate DREs spaced 6 months apart from different physicians. Even when a DRE was found to be suspicious by both, 25% of men had cancer. When at least one found it suspicious, 5/21 (24%) had cancer [10]. Thus, DRE remains a crude test for detection of curable prostate cancer.

2.1.2 Biopsy

While the DRE is an unreliable method of diagnosis, the needle biopsy gives true histologic confirmation of cancer. It is currently the only method of definitive diagnosis of prostate cancer, through sampling of prostatic tissue.

Development of cytological (cell-based) and histological (tissue-based) sampling of the prostate, was pursued simultaneously, with aspiration biopsy of the prostate first described by Ferguson in 1930 [11]. Franzén et al described an improved technique in 1960 with the addition of a transrectal needle guide [12]. Fine needle aspiration biopsy (FNAB) involves placing a needle, guided by finger, into a palpable nodule, and extracting cells using a separate syringe.

Histological sampling of the prostate through transrectal needle biopsy was first

described in 1937 [13]. This technique was proven to be a safe and effective procedure, and was subsequently improved as a standardized technique [14, 15]. Despite the development of this relatively straightforward procedure, successful sampling varied greatly, with diagnostic material only obtained in 50–95% of cases [16].

A direct comparison of both techniques originally found needle biopsy to be a more effective procedure, detecting cancer at a 95% success rate, compared to a 82% success rate for FNAB [17]. Although there was initial controversy in the use of FNAB versus needle biopsy [18,19], they were eventually found to be equivalent, and complementary in certain cases [20]. Today, the widely-adopted of biopsy involves bilateral sampling with tissue cores obtained from the medial and lateral aspects of the apex, mid-portion, and base of the prostate (typically 12 cores) [21].

2.1.3 Gleason Grading

The rapid increase in needle biopsies during the mid-20th century, necessitated a standardized method of pathology interpretation of prostatic tissue. Initially, several grading systems existed, all of which involved some notation about cancer morphology and severity. This lack of consensus caused variation in reported cancer positivity rates. [22] In 1966, a new cancer grading system emerged, which included clear descriptions of cancer morphology and, for the first time, directly correlated them with actual specimens. Furthermore, this new diagnostic method could be standardized and taught to others.

The Gleason grading method, originally described in 1966, was based on experience from the VA and Mayo Clinic [23]. This system uses a 1-5 score to denote the level or pattern of cancer de-differentiation, with 1 being indistinguishable from benign tissue, and 5 representing undifferentiated cancer cells. In an effort to easily disseminate the system to pathologists, Gleason presented an instructive diagram on

the levels of cancer de-differentiation [23].

When giving a Gleason grade, two numbers are given, that sum up to a final score. The first number, or primary score, signifies the predominant Gleason pattern in the tissue sample, while the second number, or secondary score, represents the second most prevalent grade represented in the sample. If the two numbers are the same, only one type of cancer is present within the specimen.

Originally, the system called for scoring solely based on the level of cell de-differentiation. This efficacy of this method was later confirmed in 4000 patients [24]. Consensus on the use of the Gleason grading system was eventually reached amongst urologists [22]. It was found that Gleason grading was useful as a in predicting final pathological stage, and remains a valuable clinical research tool [25, 26].

A later system dedicated to staging was developed as an extension to the universal cancer staging system (TNM) by The United International Cancer Committee (UICC) in 1992 [27].

2.1.4 Transrectal Ultrasound (TRUS)

Acoustic imaging of the prostate traces back to the late 1960's, when Watanabe introduced the use of gray-scale transrectal ultrasound (TRUS) [28]. Early on, it was reported that TRUS could be used for diagnosis of prostate cancer [29]; authorities at the time widely subscribed to a hypoechoic lesion of prostate cancer [30]. However, later studies showed that localized CaP is usually isoechoic in appearance and cannot be reliably distinguished from normal tissue [31, 32]. Furthermore, it was shown that ultrasound was unreliable as the sole method of cancer diagnosis and not superior to DRE for cancer staging [9]. The shift from a hyperechoic to a hypoechoic, then isoechoic appearance, highlights the unreliability of historic ultrasound techniques in identifying cancer. Currently, TRUS is the standard of reference for guidance during

needle biopsy. Originally, a biopsy was performed using digital (finger) guidance.

Doppler ultrasound, which measures frequency and phase shifts in the ultrasound signal, has also been used to visualize blood flow within the prostate [33]. Two forms of doppler ultrasound exist; color doppler gives relative blood velocity, while power dppler correlates with the absolute volume of movement. However, neither of these techniques appears to offer a considerable improvement in sensitivity of cancer detection [34–36], especially with low-grade disease [33, 37]. Contrast-enhanced US has also been explored, but it provides only limited clinical information in practice and results vary widely [36,38,39]. Gray-scale TRUS, now a working tool of every urology clinic, has continued to show poor sensitivity and specificity [32, 40], and is currently used mainly for volume determination and needle guidance during systematic biopsy. Thus, TRUS modalities, while promising, have been limited in their ability to accurately differentiate CaP from benign tissue [41].

2.1.5 Prostate Specific Antigen

In the late '70s, a promising new marker for prostate cancer was discovered, and quantified in the blood [42,43]. Prostate Specific Antigen (PSA) is a blood test where serum levels of the antigen are determined via an immune-enzymatic assay. Elevated serum levels of PSA are considered a possible harbinger of prostate cancer [44], but specific thresholds, e.g. 4 $\frac{\text{ng}}{\text{ml}}$, remain controversial [45, 46].

A landmark in the late '80s conclusively showed that PSA levels correlated with cancer incidence and severity, and was thus a reliable marker for prostate cancer [47]. While further explorations of PSA have continued through the last decade, its reliability has declined due to the rapid increase in early-stage disease [46, 48]. While PSA is specific to prostate disease, PSA levels are not specific for cancer. Furthermore, PSA levels rise normally with age, development of benign prostatic hyperplasia (BPH)

and prostatitis, prostatic manipulation, and even transiently following ejaculation. One CaP marker more specific for cancer than PSA, the PCA3 gene test [49], was recently approved by the U.S. Food and Drug Administration (FDA). While other new markers are under development [50], it is unlikely in the near future that any indirect CaP marker will replace need for biopsy to establish a diagnosis.

2.2 Modern Era and Current Challenges

The advances in the past 40 years have contributed to a significant increase in short-term survival rates, jumping from 69% in the late '70s to nearly 100% today [1]. Approximately 80% of biopsies done today are PSA-driven, i.e., an abnormal PSA serum level prompted the biopsy. However, PSA testing for prostate cancer is now recognized as a fundamentally limited test [46]. In fact, the greatest contributions to serum PSA levels are prostate volume, advancing age with increased leak, and prostatitis. Currently, contributions to serum PSA from localized CaP are greatly confounded by the other factors [46]. Despite the above limitations, many men with an elevated PSA level will elect biopsy. Among them, a perplexing sub-group of men are those with the PSA dilemma, an elevated PSA but normal biopsy. Current diagnostic methods are unable to provide information about the cancer location and extent, except in highly fortuitous cases.

Presently, when a man is suspected of harboring prostate cancer, he can expect a 25% chance of a definitive diagnosis [51]. If high grade cancer is found, then a wide variety of treatment options are available, including surgery, radiation, and focused ultrasound (Table 2.1). All therapeutic options, however, involve ablating or removing the entire gland, and carry serious risks to continence (ability to retain urine) and potency (sexual function). Even with treatment, there is still a risk for cancer recurrence [6].

Alternatively, if low-grade disease is discovered, or if cancer is not found, the management path is less clear. Due the inadequacies of the sampling method, and slow-growing nature of the disease, the patient has to gamble between delaying treatment for potentially lethal cancer and risking a poor quality of life [52].

Technique	**Description**	**Initial Costs**
Open Retropubic Radical Prostatectomy (RRP)	Open surgical removal of the whole prostate	$4437 [53]
Robot-Assisted Laparoscopic Radical Prostatectomy (RALP)	Whole prostate removal using a robot	$6752-15,197 [54, 55]
Brachytherapy	Needle-based insertion of radioactive seeds	$7574 [56]
Cryotherapy	Needle-based insertion of cold gases, which freeze and destroy the prostate	$7588 [56]
3D Conformal Radiation Therapy	Prostate is irradiated with x-rays using a computer-generated model	$9900 [57]
Intensity-Modulated Radiation Therapy (IMRT)	Prostate is irradiated with x-rays of varying intensity from multiple vectors	$25,845-38,000 [57, 58]
Proton Beam Therapy	Protons are focused on areas with CaP, which minimizes damage to neighboring tissues	$58,610 [58]
Chemotherapy	Administration of anti-cancer drugs	$24,000 [57]
Androgen Deprivation Therapy	Hormone suppression used to shrink tumors	$7200-8760 [56,57]
Active Surveillance	Patient routinely followed with PSA testing, imaging, and biopsy.	$743-2586 [54, 56]
Watchful Waiting	No treatment pursued.	<$100

Table 2.1: Cost comparison of different treatment strategies for prostate cancer.

A note on the definition of "significant cancer"

Prostate cancers of low grade (no Gleason 4 component), low stage (generally T1c, see Appendix A), and low volume are increasingly termed 'insignificant,' indicating a putative lack of metastatic potential. Such terminology represents a dramatic change from earlier times, when any tumor tissue found upon prostate biopsy might dictate active treatment. Currently, patients with apparent 'insignificant' or low-risk cancers are often entered into active surveillance, wherein treatment may be deferred indefinitely.

However, prospective differentiation of significant from low-risk CaP has proven difficult. Traditionally, stage, grade, and volume have been assessed via biopsy, performed in a blind manner. Thus, improvements to biopsy methods are critical in advancing the ability to predict tumor potential. A biopsy method that reveals the true biologic potential of a prostate tumor would help resolve two important problems: *over-treatment* of low-risk tumors and delayed diagnosis of serious cancers. Currently, more than half of all radical prostatectomies may not be necessary (overtreatment), but over 34,000 men will die from CaP this year (delayed diagnosis). Both issues could be resolved through improved prostate imaging and targeted biopsy.

2.2.1 Multi-parametric Magnetic Resonance Imaging

Multi-parametric MRI (mpMRI) utilizes different MR imaging modalities for different functions, such as anatomical definition, blood flow, and cellular characteristics. MRI in its various uses has been used to evaluate the prostate and surrounding structures for several decades [59]. Parameters that have been explored include T1- and T2-weighted imaging, dynamic contrast enhancement, diffusion weighted imaging, and spectroscopy.

Initially, T1- and T2-weighted imaging (T2WI) and spectroscopic imaging were used to stage CaP [60–63]. Standard T2WI provided excellent resolution, but could not discriminate cancer from other processes with acceptable accuracy, confining its use to general morphological determinations of suspicious areas [64, 65].

Dynamic contrast enhanced (DCE) MRI, used to visualize blood perfusion, involves a bolus injection of gadolinium contrast during rapidly repeated scanning with high temporal resolution. DCE MRI has been explored for CaP detection over a decade, and has been validated with varying degrees of accuracy [62, 63]. DCE, modeled using pharmacokinetic parameters, is thought to be able to accurately image vascular pathophysiology, such as angiogenesis [66, 67]. Furthermore, prior studies have suggested a correlation of such parameters with the histologic grade of disease [68, 69]. Both simple and complex models of DCE have been shown useful for the detection of prostate cancer [64, 70–73].

Diffusion weighted imaging (DWI) involves the quantification of free water motion, or Brownian motion through the apparent diffusion coefficient (ADC). An average value (aADC) is then computed for general areas inside the prostate, such that a lower aADC corresponds to greater restriction in free water motion (given in $\frac{\text{mm}^2}{\text{s}}$). CaP tissues restrict free water motion, likely on the basis of increased cellularity [74–76]. The addition of DWI to prostate MRI was shown to improve sensitivity and specificity for both peripheral and central gland disease [77–82]. The degree of diffusion restriction also appears to correlate with Gleason score, perhaps reflecting cellular density [81, 83]. Decreased ADC values are reported to correlate with unfavorable histology on repeat biopsy in men on active surveillance [84].

While DWI and DCE alone appear likely to increase the accuracy of localized CaP diagnoses, multiple MR parameters has shown to improve sensitivity over any single parameter [67, 72, 85–87]. Furthermore, the use of mpMRI may also enhance overall

accuracy in cancer diagnosis [73, 88], and improve biopsy yield [89–91]. Spectroscopy has also been evaluated in this context, but has not been shown to improve diagnostic accuracy when added to other imaging parameters [92–98].

2.2.2 MR-Guided Biopsy

Methods of targeting lesions on MRI fall into two categories, biopsy using direct MR guidance, and biopsy using Ultrasound registered (fused) with MRI. In the former, Suspicious regions of the prostate are identified first on a diagnostic MRI, and then biopsied under separate MR guidance. Prospective biopsy of suspicious areas using MRI has shown to improve cancer detection rates and aid in cancer staging [99]. Attempts to conduct MR-guided biopsy have been undertaken for over a decade, since transperineal MR-guided biopsy was used to target a single lesion in a patient with a very high PSA (45.3 $\frac{\text{ng}}{\text{ml}}$), which was found to be cancer [100]. This study was conducted at Brigham and Women's Hospital using an 0.5T open-bore "double-donut" scanner, which contained a gap in the magnet sections, allowing for intervention to take place during imaging [101]. Transperineal biopsy using this platform was validated in phantoms and yielded a needle placement error to 1.2 mm [102].

Another MR-guided biopsy method was developed by Fichtinger *et al* in 2002, which used a robot-assisted device and could be performed with either transrectal or transperineal needle insertion [103, 104]. An improvement to this device, called APT, consisted of a 3 degree-of-freedom (DOF) manipulator for needle insertion, and improved the needle placement accuracy from 2.5 mm to 2.1 mm in phantoms [105, 106]. Further systems development on the APT-II platform added motion tracking, a 6-DOF manipulator, and improved the placement error to 1.5 mm with metal needles, and 0.6 mm with glass needles [107, 108].

Clinical studies from this group in 5 patients found biopsy placement accuracy of

1.8 mm [109]. A follow-up study with the National Institutes of Health in 13 patients with a prior negative biopsy found cancer in only a single area out of 15 targets [110]. However, upon systematic biopsy, cancer was only found in one other patient.

A clinically-approved system emerged in 2005 from Siemens, which included a 3-DOF MR-compatible biopsy guide and planning software [111]. The device was initially tested in 12 patients (mean PSA of 10 $\frac{\text{ng}}{\text{ml}}$) using a 1.5 T scanner, and detected cancer in 12/60 lesions (20%) [111]. A follow up study using 54 patients (mean PSA of 12.1 $\frac{\text{ng}}{\text{ml}}$) used a 3T scanner and an endorectal coil, and found 53/178 targeted areas positive for cancer (30%) [112]. Hambrock *et al* found a much higher tumor detection rate (59%) in 71 patients with prior negative conventional biopsies [98, 113]. Almost all the positive areas (97%) contained clinically significant CaP [98].

Despite the relatively high cancer detection rate for MR-guided biopsy (between 38% and 56%), MR-guided biopsy has not been widely adopted [99, 109]. This procedure suffers from a long execution time (45 mins - several hours), carries a high cost, and can only sample a small number of cores in practice [109]. Furthermore, with the exception of the Brigham and Women's Hospital group, biopsy samples are not actually taken under real-time guidance. The patient has to be pulled out of the MR gantry and then pushed back in following a biopsy sample [111].

2.2.3 Multi-modal Image Fusion

One way to remove the need for using an MR scanner is through multi-modal image fusion. Fusion imaging utilizes the strengths of multiple modalities by merging concordant images or volumes. Multi-modal image fusion in the prostate is already in use for staging and treatment applications. For example, in positron emission tomography - computed tomography (PET-CT) of the prostate, metabolic activity (PET) can be accurately localized within a high-resolution anatomical map (CT) [114, 115].

The combined structural and functional information then aids with identification of lymph node metastases or cancer recurrence after surgery [116].

Another example of fusion in the prostate is MR-CT fusion, used currently for external beam radiation therapy of CaP. In this modality, gold spheres are inserted into the prostate, which are used for prostate localization during radiation therapy. Since gold highly attenuates x-rays, fiducials can be located with high contrast [117].

Computed Tomography (CT) and Positron Emission Tomography (PET), while useful for staging, have not proven useful in the detection of prostate cancer within the gland [38, 118, 119]. MR-US fusion currently offers the most promise in localizing and accurately sampling CaP. Although MR-US fusion is active used in other clinical areas such as neurosurgery, its use in the prostate is relatively new [120, 121]. Early approaches focused on brachytherapy, which paved the wave for its use in CaP diagnosis [122–124].

Description	3D US Acquisition	Biopsy Access	Tracking Mechanism
National Institutes of Health (NIH) / Philips [90, 125–127]	Manual sweep from base to apex	Transrectal	External magnetic field generator
Hitachi Real-time Virtual Sonography [128, 129]	None (real-time biplanar TRUS)	Transrectal	External magnetic field generator
Kaplan et al. [130, 130]	Linear translation (stepper)	Transperineal	Stereotactic positioning
Envisioneering TargetScan [131–133]	Automatic rotation / translation with specialized TRUS probe	Transperineal	None (stationary procedure) with angled needle
Université J. Fourier / Koelis Urostation [134–137]	3D TRUS probe, three different volumes elastically registered	Transrectal	Real-time TRUS-TRUS registration
University Hospital Heidelberg / Biopsee [138]	Linear translation (stepper)	Transperineal	Stereotactic positioning
Robarts Research / Eigen Artemis [139–143]	Manual rotation	Transrectal	Mechanical arm with encoders

Table 2.2: Overview of targeted biopsy technologies utilizing MR-US fusion.

Transrectal Approaches

MR-US image fusion during biopsy, explored for the last decade, requires 3D visualization of ultrasound, real-time tracking of the biopsy needle, and software to register (fuse) MR and ultrasound volumes [130]. These systems allow a clinician to biopsy the prostate in 3D, and perhaps obtain a truer "systematic" distribution of biopsy cores [139].

An early 3D prostate biopsy system, TargetScan, used a stepper motor to acquire sequential 2D image slices, which were then reconstructed into a 3D volume in software. A special needle was used that could be inserted parallel to a TRUS probe while entering the prostate a 45 degree angle. A study in 2007 found that 3D biopsy with evenly spaced samples and an angled point of entry detected more CaP and predicted true Gleason scores better than freehand biopsy [131]. A multi-institution study followed up with 140 men (median PSA of 5.2 $\frac{\text{ng}}{\text{ml}}$) and found a 48% CaP detection on initial biopsy [132]. Moreover, it was found that 3D biopsy cancer detection rates are comparable to extended core biopsy, and is reproducible in men with elevated PSA (4-10 $\frac{\text{ng}}{\text{ml}}$) undergoing initial biopsy [133].

An alternative method of 3D prostate reconstruction using a multi-planer TRUS probe was developed by Baumann *et al* and Koelis SAS (La Tronche, France) [134]. Real-time US images were registered during biopsy with a pre-acquired 3D TRUS dataset, and could be performed in 2.3 seconds, nearing 90% accuracy [134]. Clinical prostate biopsy studies were conducted using 17 patients, which found an 0.83 mm 2D to 3D TRUS registration accuracy [135]. Phantom studies showing the feasibility of MR-US fusion using this system was then demonstrated, followed by a clinical pilot study [137, 144].

The U.S. National Institutes of Health collaborated with Philips to develop and test a transrectal prostate biopsy device which employed MR-US fusion [125]. This

device was swept axially across the prostate to create a 3D volume, while biopsy tracking was performed using an external magnetic field generator. Initial phantom tests from this device found a 2.3 mm error [125]. Retrospective clinical studies were then performed 41 patients, which found an 18.5% detection rate for lesions seen on DWI, DCE, T2WI, and spectroscopy [145, 146]. Follow-up studies found that targeted biopsy MR-US fusion improved CaP detection in patients undergoing initial biopsy, and MR suspicion levels were correlated with D'Amico risk stratification [87, 126, 127, 147]. While MR-US fusion biopsy was found to be comparable to MR-guided biopsy for CaP detection on initial biopsy, the same group noted that "further research is necessary to suggest why patients had disease detected on MRI/US fusion alone or TRUS biopsy alone" [148].

In Japan, a study using a TRUS probe, shaped to mimic an endorectal MR coil, was used for targeted biopsy [128]. This system, Real-time Virtual Sonography, was used for transperineal biopsy on 85 patients with at least one prior negative biopsy (median PSA of 9.9 $\frac{\text{ng}}{\text{ml}}$), and found cancer in 32% of cases [128]. The feasibility of using this system with transrectal biopsy was also demonstrated [129].

Recently, a group out of Robarts Research developed a mechanically-assisted transrectal biopsy device using mechanical encoders to track the needle position in real-time during biopsy [139, 149]. Initial phantom studies found 2.3 mm positioning errors, and the system was then tested in patients [141]. Targeted biopsy with MR-US fusion was then performed in 25 patients, and consistently detected more CaP than systematic biopsy [142] .

Transperineal Approaches

A number of MR-US fusion devices have utilized a transperineal approach rather than a transrectal approach [130, 138, 150, 151]. Although there have been studies

touting the effectiveness of one biopsy method over another [152], cancer detection rates between 12-core transrectal biopsy, and transperineal biopsy have generally been similar [153].

One study using a stereotactic transperineal biopsy device and six-point fidicial registration found that MR-US fusion could be adequately performed [130]. A recent study with 106 patients (median PSA of 8 $\frac{\text{ng}}{\text{ml}}$) found a 60% CaP positivity rate [138]. This device consisted of a transrectal probe with integrated stepper capable of 0.1 mm and 0.1 degree movement resolution. However, biopsy was performed in 30 - 60 minutes with an error of 1.7 mm [138].

There appears to be little difference between outcomes using transrectal and transperineal systems. Existing studies which use either method have primarily explored a patient group undergoing initial biopsy. The role of fusion in low-risk patients, those men in whom curative treatment will be of unknown benefit, has yet to be explored. This thesis explores a system based off of Bax et al, which utilizes mechanical tracking and an articulated arm [139]. Prior to the studies presented in the following section, no clinical testing had occurred using this device. The next section introduces original validation studies and the role of MR-US fusion biopsy in improved CaP diagnosis.

Chapter 3

Targeted Biopsy in Low-Risk Population

The most important function of targeted biopsy is identifying cancers that are missed by conventional biopsy. In high-risk populations, e.g. men with grossly elevated PSA or palpable abnormalities, most cancers are detected by random, systematic biopsy. In such men, MRI has shown to accurately predict a cancer diagnosis [113, 154]. Exclusion of such men from active surveillance and prompt institution of curative treatment are readily accomplished using current diagnostic methods.

However, in 'low-risk' populations, additional imaging studies and targeted biopsy of suspicious findings might prove helpful in arriving at a correct diagnosis. We thus explored the use and impact of MR-US fusion in this population. We utilized different methods for fusion than previous studies. Each of the components of fusion were validated, and are discussed in this chapter. Subsequent chapters examine the impact of this technology in a clinical context.

Low risk has been traditionally identified as men with previously diagnosed minimal amounts of disease or a PSA $< 10\frac{ng}{mL}$. This investigation involved patients that satisfy either of two low-risk criteria:

1. Patients with no prior history of CaP, at least one prior negative biopsy, and persistently elevated PSA.

2. Patients with a prior diagnosis of low-grade (Gleason 3+3) disease.

Men with a prior confirmed diagnosis of low-grade CaP are routinely followed

with a yearly regimen of PSA testing and TRUS biopsy. The goal in this population is to accurately stage cancer, and to ensure that truly low grade disease is present (i.e. no Gleason pattern 4). Typically, these men are enrolled in a program of active surveillance, which aims to track the progression in low-grade tumors. For the purposes of this study, eligibility for active surveillance was defined according to the Epstein criteria[i] [155].

In contrast, the second group of men have no prior history of prostate cancer. In these men, cancer is either truly absent, or is undetectable by conventional biopsy methods. For these men, anxiety exists since treatment might be unnecessarily delayed, potentially leading to a lethal consequence [4,5]. Cancer-related anxiety might drive such men to seek radical treatment when CaP is found upon biopsy, regardless of severity of the lesion. The limited accuracy of conventional biopsy adversely affects the decision making ability of both patients and physicians.

The targeted biopsy procedure subsequently described contains two important steps: identification of a target suspicious of cancer, and *navigation* to the target precisely in real time. MRI was used as the diagnostic method since it currently offers the best sensitivity and specificity in cancer detection. A 3D TRUS imaging device with biopsy tracking features was used to perform navigation and targeting of suspicious areas.

3.1 Multi-parametric Magnetic Resonance Imaging

The ability of MR-Ultrasound to be able to aid in cancer detection hinges on the sensitivity and specificity of the MR image acquisition technique. This thesis describes a multi-parametric (mp) MR imaging technique with each parameter tracking a unique

[i] Bx criteria: $\leq$G3+3; $\leq$2 cores; no individual core harbors >50% cancer; stage $\leq$pT2a.

phenomenon. Although mp-MRI is utilized at a number of academic institutions, the utility of each parameter has been previously unknown when using quantitative metrics for dynamic contrast enhancement (rather than subjective image analysis). Suspicious areas are prospectively graded according to likelihood and significance of cancer. In this thesis, the terms "suspicious area", "suspicious lesion", and "region(s) of interest (ROI)" are used interchangeably.

3.1.1 Acquisition Method

MR imaging was performed on a Siemens TrioTim Somatom 3.0 Tesla magnet with high-performance gradients using a multi-channel external phased-array coil. Although other studies utilize an endorectal coil, which has improved signal-to-noise ratio (SNR) and is used for cancer staging, a trans-abdominal coil has been shown to be adequate for diagnosis and grade stratification [70, 89, 98, 113, 154]. Furthermore, the endorectal coil was not used due to its increase in patient discomfort and scanning time. The protocols used for each modality are given in Table 3.1, and included T2-weighted imaging (T2WI), diffusion weighted Imaging (DWI), and dynamic contrast enhancement (DCE) or perfusion. A contrast agent was used (gadopentetate dimeglumine, administered intravenously at 2 $\frac{\mathbf{mL}}{\mathbf{s}}$ during perfusion (DCE) imaging.

Sequence	**TR/TE (ms)**	**Slice/gap (mm)**	**Matrix/FOV (cm)**
T2:3D TSE	3800-5040/101	1.5/0	$256 \times 205/14 \times 14$
DWI:EPI	1600-2300/75-90	5/1.65	$256 \times 154/35 \times 26$
DCE:TWIST	2.7/1.1 (10° FA)	1.5/0	$320 \times 225/28 \times 30$

Table 3.1: MR parameter information, including pulse sequence and acquisition method. Diffusion weighted imaging (DWI) utilized a full range of b-values (0/400/800/1000), and dynamic contrast enhancement (DCE) protocol involved 42 acquisitions every 4.2 seconds with $0.1\frac{\mathbf{mg}}{\mathbf{kg}}$ gadopentetate dimeglumine (Magnevist, Bayer)

The images were then processed using dedicated prostate imaging software (CAD-vue, iCAD inc., Nashua, NH). The acquisition of multiple b-values for DWI allowed for accurate quantitation of diffusion. Perfusion sequences were processed using the Brix and Tofts model, and using an arterial input function [156]. Three variables were used for quantitative evaluation of DCE, including k_{ep}, k_{trans}, and quick initial area under the curve (Q_{iAUC}).

3.1.2 Interpretation

Each of the MR parameters utilized were interpreted by two radiologists, both of whom have specific expertise in prostate imaging, and were blinded with respect to the patient history and prior imaging studies. Suspicious areas, or regions of interest (ROI), were identified using each MR parameter, and were assigned image grades on a 1 – 5 scale, with '1' being unsuspicious and '5' as very suspicious of CaP. This 'Image Grade' scoring system is described in Table 3.2. The overall level of suspicion was a composite score determined primarily by the average apparent diffusion coefficient (aADC), which is a quantification of the speed of diffusion, and secondarily by the T2 and DCE appearance. The degree of suspicion for T2 is based on the degree of signal darkening as well as the presence of mass effect or surrounding distortion. ADC suspicion is graded based on numerical values -1.4 $\frac{\text{mm}^2}{s}$ and above was 1, 1.2 – 1.4 $\frac{\text{mm}^2}{s}$ is 2, 1.0 – 1.2 $\frac{\text{mm}^2}{s}$ is 3, 0.8 – 1.0 $\frac{\text{mm}^2}{s}$ is 4, and below 0.8 $\frac{\text{mm}^2}{s}$ is 5.

The perfusion grading system was based on 3 components: speed of wash-in (or early enhancement), intensity of enhancement, and speed of washout. Perfusion grades increased when rapid wash-in was also intense. DCE suspicion was given a point for rapid wash-in, intense enhancement, and washout, with 1 more point for intense early enhancement. While quantitative parameters were captured for DCE, the cutoff levels were unclear, so both qualitative evaluation was used for the prospective

score. The quantitative parameters were analyzed retrospectively and only performed for a subset of men enrolled in the studies presented in this thesis. Central gland lesions were also reported separately from peripheral zone lesions, as the specificity for CaP is lower in the central gland [88].

ROIs were then contoured in multiple T2WI slices, as they have the highest spatial resolution. 2D contouring was performed in OsiriX, an open-source imaging program [157]. The surface mesh for each ROI was calculated and converted into a 3D format (Object File Format) using MATLAB. Finally, a CD containing the T2 axial DICOM slices and ROI surface mesh was generated for input into the biopsy tracking device.

Image Grade	**T2-weighted imaging (T2WI)**	**Apparent Diffusion Coefficient (ADC)**	**Dynamic Contrast Enhancement (DCE)**
1	Normal	$> 1.4\times10^{-3}\frac{\text{mm}^2}{s}$	Normal
2	Faint decreased signal	1.2-1.4$\times10^{-3}\frac{\text{mm}^2}{s}$	Early or intense enhancement
3	Moderately dark nodule	1.0-1.2$\times10^{-3}\frac{\text{mm}^2}{s}$	Early and intense enhancement, or early enhancement with washout
4	Intensely dark nodule	0.8-1.0$\times10^{-3}\frac{\text{mm}^2}{s}$	Early and intense enhancement with washout
5	Dark nodule with mass effect	$< 0.8\times10^{-3}\frac{\text{mm}^2}{s}$	Early enhancement is intense with immediate washout

Table 3.2: Classification system for regions of interest (ROI) based on MR characteristics.

3.1.3 MR Validation

The MR technique was validated through correlation with whole mount prostates, recovered after radical prostatectomy. When a prostate gland arrived at surgical pathology, the specimen was weighed and measured and the outer surface inked to help with histologic determination of margin status. The body of the prostate was cut into 5-7 tissue sections depending on size. The tissue slices were then embedded intact as whole mount sections rather than being cut into quadrants, as is done in normal pathology practice. This ensured that when multiple foci of tumors were present, the size and location of each tumor could be accurately determined.

The slices were then imaged and aligned to the corresponding MR image, which allowed for direct comparison between pathological and imaging findings. Pathology features that were examined Gleason sum of each lesion, physical size, sextant and clock-face location, and presence of extracapsular extension or other staging criteria.

Over a period of several years, 116 patients underwent radical prostatectomy, and received a pre-operative multi-parametric MRI including T2, perfusion, diffusion, and spectroscopy. An endorectal coil was used since staging information was required. Linear regression on each of the quantitative MR parameters was performed retrospectively in order to determine their correlation with CaP presence and severity.

The four parameters measured included k_{ep}, k_{trans}, Q_{iAUC}, and aADC. Results from the study, seen in Figure 3.1, show that both k_{ep} and k_{trans} were not found to be highly correlated with cancer positivity. While Q_{iAUC} showed a relationship with cancer presence, in practice it was difficult to generate a reliable interpatient cutoff. aADC, however, was found to be sensitive to cancer presence, validating the mpMRI technique with prior literature findings [77–79]. The clinical studies explored in Chapter 4 explore the validity of the scoring system without the use of an endorectal coil.

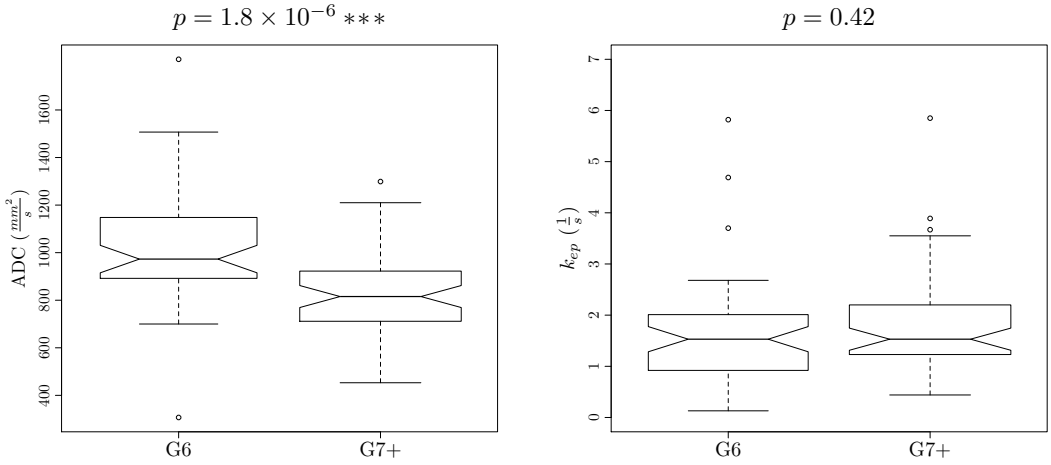

(a) ADC

(b) k_{ep}

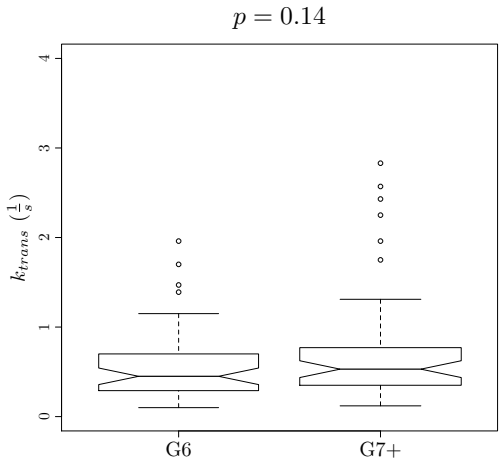

(c) k_{trans}

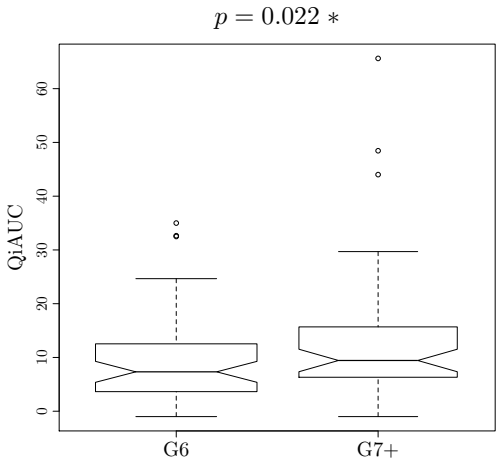

(d) QiAUC

Figure 3.1: Correlation of MR parameters with Gleason sum after prostatectomy, including (a) ADC, (b) kep, (c) ktrans, and (d) QiAUC.

3.2 3D TRUS Biopsy

In order to test the effects of fusion in a low-risk population, we utilized a commercially available 3D biopsy imaging and tracking device (Artemis, Eigen, Grass Valley, CA). Prior to the studies described in this thesis, this device had not undergone extensive

clinical testing, despite initial FDA approval (510(k)) for biopsy tracking functions.

This device has the ability to (1) create a contemporaneous 3D reconstruction of the prostate, (2) plan biopsy sites systematically, (3) digitally record and store the biopsy sites for serial study and sampling, and (4) fuse previously-obtained MRI images of the prostate with concurrent ultrasound images in a real-time manner. This system differed from other fusion imaging systems (Section 2.2.3) by featuring:

1. Mechanical encoders embedded within a tracking arm
2. Use of raw ultrasound feed from external ultrasound machine
3. Ultrasound scanning is performed using an end-fire TRUS probe

(a) (b)

Figure 3.2: Mechanically-assisted 3D imaging and biopsy tracking device (Artemis, Eigen, Grass Valley, CA). (a) Device consists of mechanical encoders embedded into a tracking arm, a graphics processor, and a user interface. (b) Another version of device which replaces counter weight with counter balance, increases device mobility, and embeds foot-pedal controls into end manipulator.

The device arm consists of a passive four degrees-of-freedom tracker with mechanical encoders terminated by a probe cradle. A conventional ultrasound machine

is used to acquire 2D TRUS images, which are captured via a coaxial input, and reconstructed into 3D using a graphics processor.

3.2.1 3D Ultrasound Acquisition

Transrectal ultrasound were acquired using a conventional ultrasound probe and machine (Hitachi Hi-Vision 5500 [Hitachi Medical Systems America, Twinsburg, OH], 7.5 MHz end-fire). Patients were placed in an angled left lateral decubitus position, such that the torso and upper legs form an acute angle, with the knees bent into the chest. This positioning ensured that the patient motion was restricted, reducing potential scanning and tracking errors during the procedure. The TRUS probe was then inserted into patient, using acoustic scanning gel to ensure acoustic matching between the probe and the rectal wall.

A preliminary cleansing enema and prophylactic ceftriaxone and ciprofloxacin were used. During preliminary scanning, the prostate was anesthetized with a periprostatic block, and a geometric volume determination (Length $\times$ Width $\times$ Height $\times$ 0.52) was made on the axial and sagittal imaging planes. Once the prostate was visualized on the ultrasound system, the tracking arm was brought to the probe, attached via a connecting cradle, and scanning commenced.

During 3D scanning, the probe was rotated 200° in order to to digitally record the entire prostate volume and to minimize rotational distortions (Figure 3.3a). These distortions occurred when the TRUS probe was not placed in the center axis of the prostate. This axis could be manually set in software prior to scanning through a calibration procedure, which was carried out monthly.

After scanning, the prostatic boundary was delineated (segmented) in two orthogonal planes. and a semi-automatic segmentation algorithm built into the software was used to reconstruct the prostate surface in 3D. This algorithm allowed for user-based

modification of the segmentation before proceeding to biopsy.

3.2.2 Biopsy Technique

Each patient received both a 12-core systematic biopsy and targeted biopsy, in order to ensure an accurate comparison between both methods. Biopsy was performed using a conventional spring-loaded gun and 18 gauge needles. The systematic 12-core biopsy consisted of samples in the apex, mid-prostate, base, and both lateral and medial sextants on the right and left sides. The planned biopsy locations were set in a template and standardized in software with respect to prostate volume and asymmetric variation.

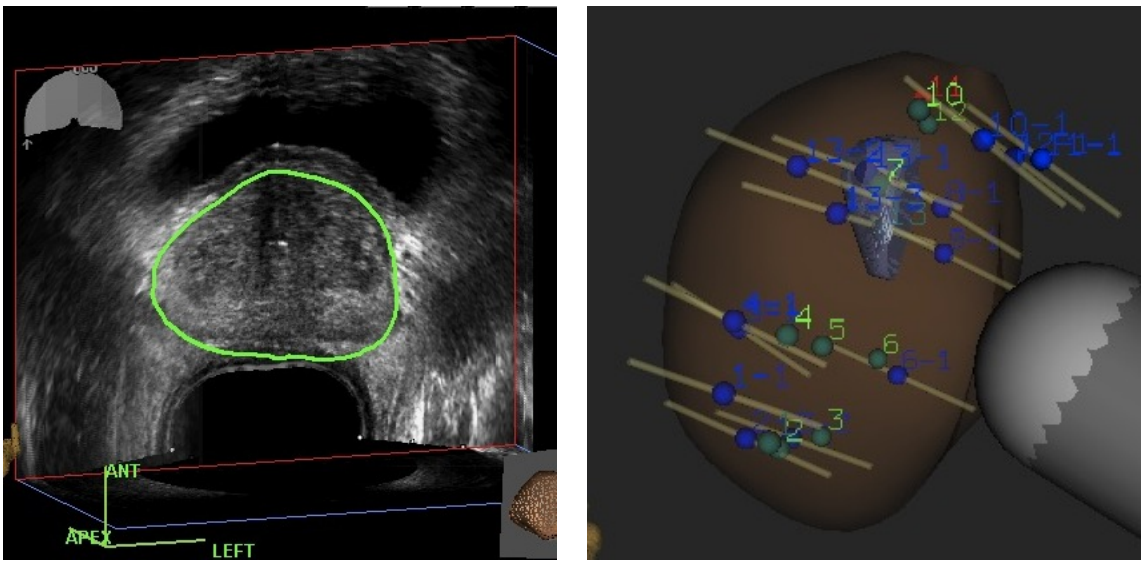

(a) 3D TRUS (b) Post-Biopsy Map

Figure 3.3: (a) 3D reconstruction of rotational TRUS scan and (b) post-biopsy map. Reconstruction is performed by biopsy device software. Green outline in (a) indicates prostate boundary, created through semi-automatic segmentation. Post-biopsy map of the prostate in (b) includes the TRUS probe (gray external probe), biopsy samples (blue dots and tan cylinders), planned points (green dots), and ROI (purple blob).

A post-biopsy map, seen in Figure 3.3b was generated using the 3D prostate model

and biopsy locations. Each biopsy sample consisted of a 1 mm diameter x 18 mm core, that was inked on the distal tip and placed in a separate bottle. This ensured that potential cancers could be retrospectively localized in the prostate. Traditionally, multiple cores from the same hemisphere or quadrant are bottled together, and pathology results are given as X of Y cores positive for cancer. However, biopsy tracking required each cancer sample to be associated with a particular 3D location within the prostate. Furthermore, it was found that core fragmentation regularly occurred, which would have confused findings. Fragmented cores could yield a high percentage of cancer in each piece, but relatively short cancer lengths. When using the Epstein criteria for active surveillance, which includes percent CaP positivity, appropriate clinical context must be known.

3.3 MR-US Registration

Accurate image registration of MR and TRUS is necessary to reliably target areas of suspected cancer. "Mental registration", which does not utilize any software, is inadequate to accurate target CaP [158, 159]. Furthermore, in prostate biopsy, the fusion method must operate in real-time to minimize probe insertion time, and discomfort for patients. Software developed for the biopsy tracking device (Section 3.2.1) was used to preform MR-US registration.

The registration procedure contained the following steps:

1. Semi-automatic segmentation (delineation) of the prostate
    a. MR, performed prior to biopsy by radiologist
    b. TRUS, performed during biopsy by urologist
2. Rigid alignment of MR and TRUS in axial, sagittal, and coronal planes

3. Elastic deformation

4. Interpolation

Following semi-automatic segmentation of prostate, a CD containing the axial MR DICOM images, the prostate surface mesh, and ROI surface mesh was loaded into the biopsy tracking device. The MR was then aligned to the TRUS volume by selecting corresponding anatomic landmarks in 3 planes (axial, sagittal, coronal). Anatomical landmarks included the base and apex of the prostatic urethra, the bladder neck, the prostate capsule, and seminal vesicles. Rotational alignment of the prostate occurred based on the selected points. Next, an automatic registration algorithm and based on an adaptive focus deformable model (AFDM) [160,161] was used. This is a snake-based segmentation technique that relies on capturing both global and local features of an object of interest. In this case, it is used to determine the appropriate registration between MR and TRUS. The final step in registration is elastic warping of the TRUS (or MR's) surface mesh to arrive at the final registered volume.

In AFDM, a training algorithm is used to generate a template or model of the segmentation or registration. Features in this system consist of triangles between three arbitrary points on the snake. Anatomical features are assigned weights, according to their importance [160]. Since triangles can consist of adjacent or distant points, both local and global features are captured, reducing the likelihood of an inaccurate solution. When a new input is given, the energy of the snake (segmentation) is minimized with respect to the training model. However, not all global minima are found due to the greedy nature of the minimization algorithm [160].

The accuracy of the MR-US fusion used in this thesis, hinges on the validity of the automatic (non-rigid) registration step to be accurate. Prior *in vitro* testing of fusion in phantoms found a 3 mm registration error [162]. Using a similar approach, 3D TRUS-TRUS registration found a 2.5 mm registration error [163]. In the studies pre-

sented in this thesis, a different person performed segmentation on MR (radiologist) and TRUS (urologist), which increased variability.

3.3.1 *In vivo* Registration Validation

In order for clinical testing to be successful, the error due to registration needed to be lower than the minimum size of significant tumors. This size was determined to be 0.5 cc, corresponding to a diameter of 4.9 mm [40]. Thus, MR-TRUS registration should be accurate within 4.9 mm. We performed an *in vivo* validation of the MR-TRUS registration accuracy, based on an existing methodology [164]. Five patients with internal gold bead fiducials (3 per patient), previously inserted to guide radiation therapy, were imaged using multi-parametric MRI and 3D transrectal ultrasound. Fiducial marker locations on MRI and TRUS were then identified by three independent users and prostates were delineated again in TRUS using the process described in Section 3.2.1.

While segmentations in TRUS and MRI were kept constant across users, manual alignment and automatic registration was independent. Target registration error (TRE), i.e. the distance between corresponding points on MR and TRUS, was averaged across users and fiducials in a study. The error associated with selecting a fiducial, or fiducial localization error (FLE), was normalized across users, and calculated as the mean norm of the resulting error vectors.

Ten of the fifteen fiducials were found with certainty on both modalities. The study showed an average target registration error (TRE) of 3.23 mm, with an average fiducial localization error (FLE) of 0.53 mm in TRUS and 0.44 mm in MRI. When all observers agreed upon an alignment for registration (i.e. when observers were permitted to influence one another), a TRE of 3.08 mm was found.

The results from this study agree with the 3.0 mm registration accuracy previ-

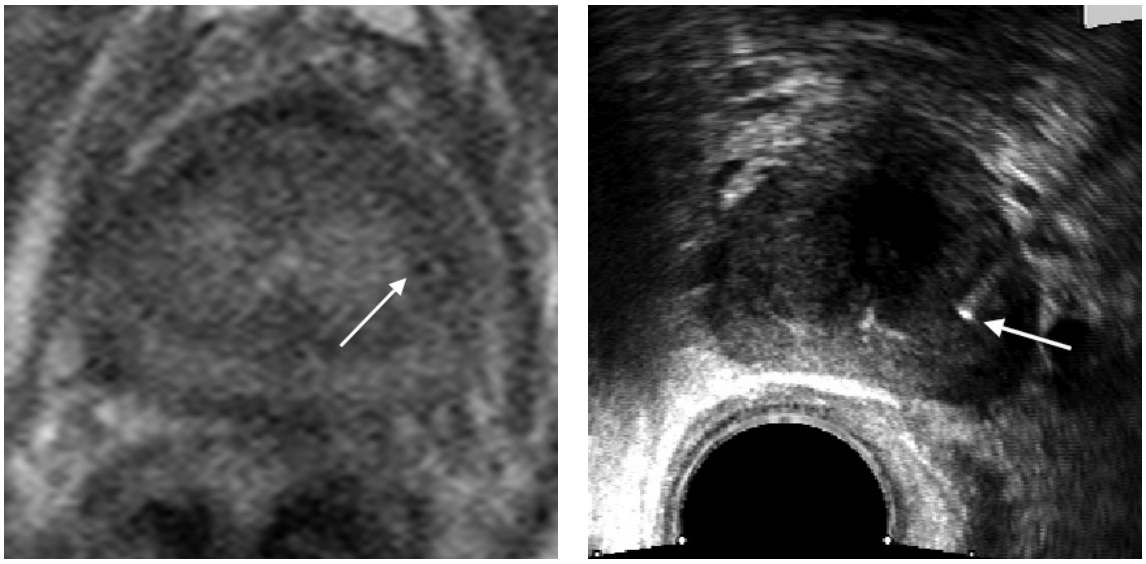

(a) MRI (b) TRUS

Figure 3.4: Fiducial localization on (a) MRI and (b) TRUS. Gold bead fiducial (white arrow) appears as a void in MRI and as a hyper-echoic reflection in TRUS.

ously found in phantoms [162]. Furthermore, it was found that FLE did not contribute greatly to TRE. Increases in both the dataset size and TRUS scan quality are necessary for improved estimation of error. A 3.23 mm registration error indicates that the MR-TRUS fusion method was sufficient for use in clinical targeted prostate biopsy studies, described in the next chapter.

Case	# of Fiducials	TRUS volume (cc)	MR volume (cc)	Max Fiducial Distance (mm)	TRE
1	2	20.25	24.85	27.67	4.91
2	2	25.83	28.00	27.20	4.15
3	2	39.67	41.16	15.65	2.17
4	1	45.98	55.74	–	2.30
5	3	134.70	107.43	45.05	3.01

Table 3.3: MR-US registration accuracy using *in vivo* gold bead fiducial markers in men undergoing radiation therapy. Markers were inserted under ultrasound guidance. Fiducial localization error (FLE) for MR and TRUS was **0.44 mm** and **0.53 mm**. Mean target registration error (TRE) was **3.23 mm**.

Chapter 4

Clinical Implementation of MR-US Fusion

This chapter describes the clinical implementation of targeted biopsy, in a low-risk population. Targeted biopsy findings are correlated with the systematic biopsy, giving a relative measure of accuracy. A true positive for comparison was available in men who received a radical prostatectomy after a cancer diagnosis. The resulting prostate specimen is sliced and preserved using large-form slides, which is used to correlate MR findings with true cancer occurrence.

Current TRUS biopsy is estimated to have a diagnostic rate of close to 25% [51]. We hypothesized that targeted biopsy will improve the detection accuracy of CaP by at least 15-20%, or have a cancer detection rate of over 40%, over the current method of freehand TRUS biopsy. A paired experiment with targeted and 3D systematic biopsy cores had over 90% power to determine an improvement of biopsy-positivity of at least 15% with the sample size of 171 patients.

An additional hypothesis is that targeted biopsy with MR-US fusion will be useful for detecting "clinically significant disease" (See section 2.2). Based on previous studies which estimate a threshold volume of 0.5 cc, targeting errors up to 4.5 mm were considered acceptable. Furthermore, biopsy needle tracking accuracy was estimated in a preliminary study to be 1.5 $\pm$ 1.0 mm [143]. Using these assumptions, the enrollment numbers for this 18-month study ensured sufficient power (>80%) to detect this potential improvement.

4.1 Study Design

This study was conducted over an 18 month period between March 2010 – September 2011 involving 171 patients. Approval by the UCLA Institutional Review Board (IRB) was obtained prior to commencement. Patients prospectively enrolled in the study consisted of men in the UCLA active surveillance program (ASCAP) and men undergoing re-biopsy due to elevated PSA. Patients were excluded from the study due the following factors:

1. No prior biopsy.
2. Prior radical treatment for CaP.
3. Exclusion from MRI (metallic implants, etc.)
4. Intolerance of transrectal prostate biopsy.

Patients enrolled in the study received a multi-parametric 3T MRI with a trans-abdominal coil prior to biopsy, according to the technique described in Section 3.1.1. MR images were interpreted and processed according to Section 3.1.2. Processed data was inserted via CD into the biopsy tracking device, following 3D TRUS acquisition, described in Section 3.2.1. For each suspicious area seen on MR, one biopsy core was taken for every 3mm of the target's maximum diameter. The following workflow was adopted:

1. Patient is imaged using multi-modal MR prior to biopsy visit
2. Prostatic volume in MR is extracted in software (segmentation)
3. Suspicious lesions based on T2 appearance, diffusion, and perfusion parameters are annotated and reconstructed in 3D.

4. During biopsy, prostate is scanned in 3D using conventional TRUS machine connected to biopsy tracking device (Artemis, Eigen)

5. Prostatic volume is delineated in TRUS using software (segmentation)

6. MR and TRUS are aligned in 3D using identifiable fiducials (base and apex of urethra, bladder neck, seminal vesicles, prostatic boundary) in axial, sagittal, and coronal planes

7. Images are fused, and targets are placed in the regions of interest

8. 12-core systematic biopsy plan is overlaid on the 3D prostate model

9. Tissue sample taken from each planned point, inked on distal end, and placed in an individual bottle for pathology processing

Men enrolled in the study received either one or multiple biopsy sessions, as part of the normal diagnostic pathway. Biopsy sessions from the same patient (spaced 6 months–1 year apart for men enrolled in active surveillance) were performed independently, with the radiologist blinded to the clinical history of the patient for scoring purposes. Each biopsy session has an associated MRI, with which suspicious areas are identified. Finally, each tissue sample had individual characteristics that could be analyzed due to the use of a single bottle per biopsy core. Samples were taken as part of a systematic biopsy protocol, or from a target area. Figure 4.1 describes the relationship of different clinical factors in our protocol.

4.1.1 Clinical Variables

In order to detect effects related to fusion imaging and biopsy accuracy, we collected data on patient demographics, general visit information, MR interpretation, and pathology outcome. In particular, we were interested in the Gleason grade for

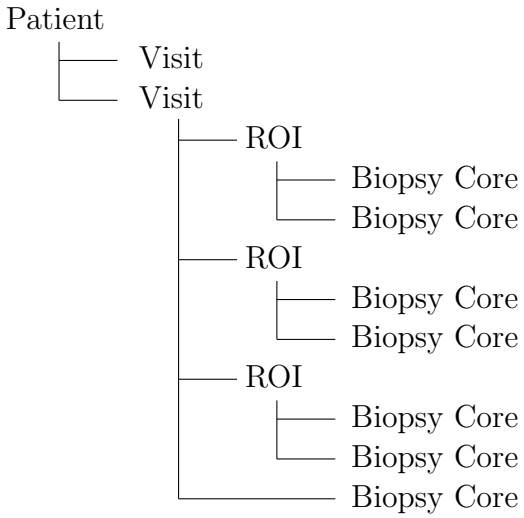

Figure 4.1: Diagram of data relationship in the clinical studies presented in this thesis. Each patient enrolled in a study could have multiple biopsy sessions (visits). During each visit, suspicious areas were prospective noted on the MRI (ROI), which were then sampled during biopsy (Biopsy Core). 12 biopsy cores of each systematic area (apex, mid-portion, and base of lateral and medial aspects of each side of the prostate) were also taken. Due to the complexity between data types (patients, visits, ROIs, and biopsy cores), all data was stored in a relational SQL database.

both systematic and targeted cores, as well as the image grade assigned to targeted cores. We also wanted to measure the performance of MR imaging, so a multitude of MR parameters were recorded, including aADC, perfusion scores, and locality. We tested the clinical utility of these metrics by testing correlation between image grades and pathological outcome. A number of secondary variables were also collected in order to extract the complex nature of both successes and failures of targeted biopsy. Table 4.1 describes all the measured variables.

The "target hit on 3D variable" indicates if a targeted core actually went through the target. This is determined by retrospective verification of ultrasound and computed imagery.

Variable Group (table)	Key variables
Patient	Date of birth, active surveillance status, treatment notes
Visit	Date of biopsy, Date of MRI, most recent PSA, % free PSA, ASCAP enrollment, Date of previous biopsy, number of previous biopsies, previous positive biopsy, TURP, MR protocol used, manual TRUS and MR volumes, software (segmentation) TRUS and MR volumes, depth setting of TRUS device, number of scans performed, number of time motion compensation feature used, hardware and software errors in procedure
Target (ROI)	ROI location, ROI clockface, ROI % apex to base, zonal location (central/transition or peripheral), ROI maximum diameter, ROI volume, presence of a diffuse nodule, T2 image grade (1-5), DCE image grade (1-5), aADC value (using full range of b-values), mean and median kep, ktrans, ejection volume fraction, and area under the curve (AUC)
Biopsy Core	Corresponding ROI (if targeted core), primary and secondary Gleason score, presence of prostatic intraepithelial neoplasia, presence of atypical small acinar proliferations, cancer on inked end (indicating distal location), number of core fragments, number of positive core fragments, total cancer length, total core length, presence of inflammation, freehand core, targeted core, core name on Artemis device, presence of perineural invasion, target hit on 3D, percent of cancer in cores

Table 4.1: Data variables collected for each study component.

4.1.2 Data Analysis

All patient data was stored in a secured, searchable relational database (postgreSQL, PostgreSQL Global Development Group) on a Linux workstation. We developed a custom, cross-platform software application in C++ in order to facilitate entry of patient data, including error validation. Screenshots of the various application functions are shown in Figure 4.2.

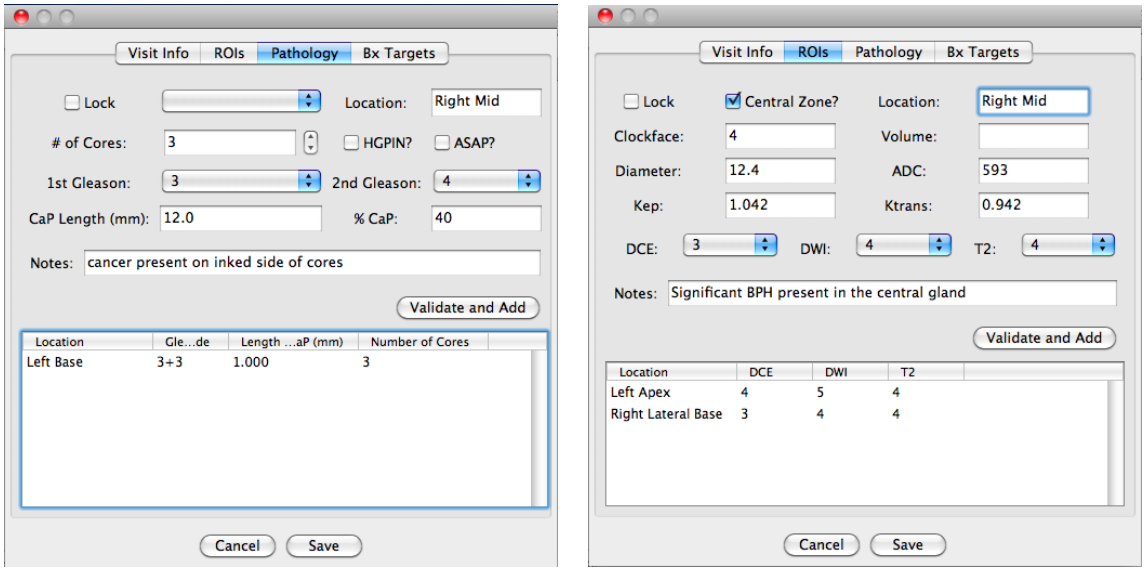

(a) (b)

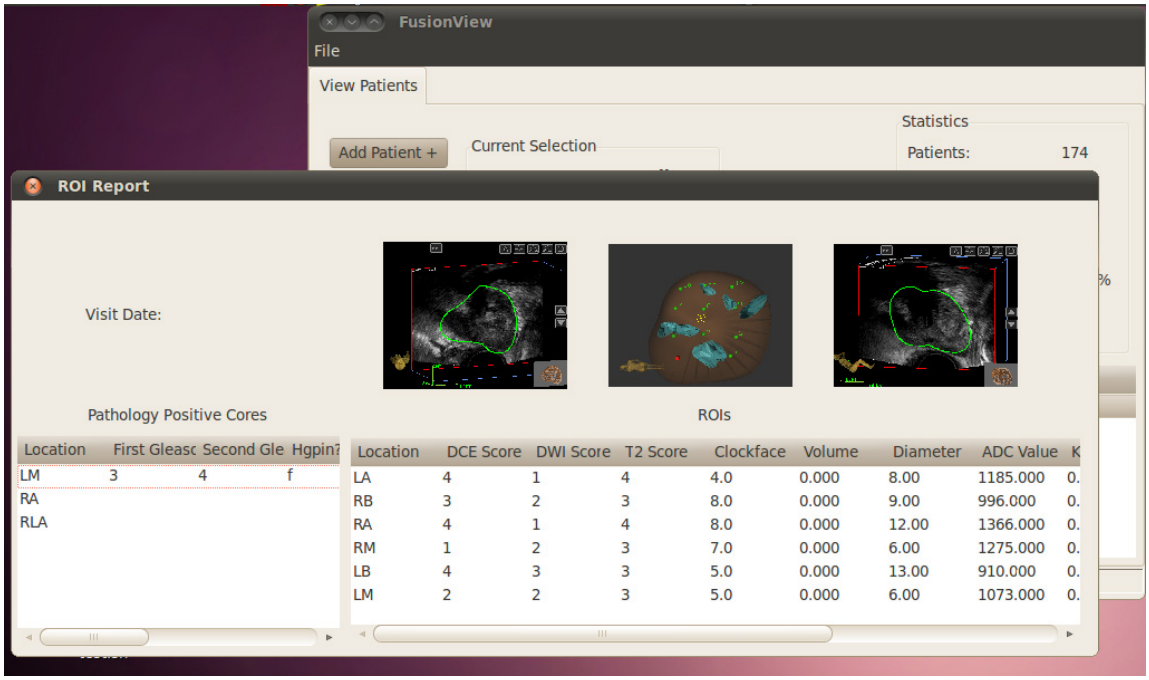

(c)

Figure 4.2: Data collection and analysis software developed at UCLA showing (a,b) entry validation and (c) data visualization.

The software that we developed for this study allowed for data validation during entry, standardization of input, and data exploration. This served two functions: minimization of data entry-related errors, important for accurately correlating imaging with cancer, and real-time visualization of related clinical information for aiding analysis.

All data analysis was performed using R, an open-source statistical analysis software program. Additional functions from the Weighted Gene Co-expression Network Analysis package (WGCNA) were used [165]. For most of the tests performed, there was no assumption of a normal distribution, and therefore non-parametric two-tailed statistical tests were used. Descriptive statistics were used to analyze patient characteristics such as age, PSA, prostate volume and previous biopsy results. For measures that tested a variable's effect on ordered data, such as Image grade or Gleason grade, a Spearman's rank correlation test was used. For analyses comparing pairs of ordered data, such as targeting and systematic biopsy accuracy, a two-pair Wilcoxon Signed-Rank Test (Mann-Whitney U test) was used. For continuous data, and tests examining a variable's effect on a binary outcome (i.e. Gleason $> 3 + 3$), a Kruskal-Wallis test was used. For binary classification, and for data that contained small numbers, a Fisher's Exact test was used. All results were examined and verified by a statistician.

4.2 Results

Patient characteristics and biopsy results are shown in Table 4.2. 171 subjects (median age 65) underwent fusion biopsy a total of 182 times. Multiple visits were excluded in the analysis presented in this thesis, as studies that examine the accuracy from one visit to another require a larger sample size. 106 men underwent biopsy for surveillance, while 65 had prior negative biopsies, but elevated PSA. At the time of

biopsy, median PSA was 4.9$\frac{ng}{mL}$ and median prostate volume was 48 cc.

	All	**Previous Positive Biopsy**	**Previous Negative Biopsy**
# of Patients	171	106	65
Mean # of Prior Biopsies	1.64	1.47	2.16
Mean Age (yrs)	64.5	64	65
Mean time from MR to Bx (days)	27	26	28
Median PSA ($\frac{ng}{mL}$)	4.9	4.35	7.3
Median Volume (cc)	51.4	46.9	58.7

Table 4.2: Statistics for patient groups in the targeted biopsy study. Statistics are broken down into two groups according to whether patients have a prior confirmed cancer diagnosis biopsy or not. Both groups only differ by median PSA, median volume, and mean number of prior biopsies (positive or negative).

The average number of biopsies prior to this study was 1.47 (median of 1) in the surveillance population, and 2.16 (median of 2) in the negative biopsy population. The average time between MRI and biopsy was 27 days. Procedure time, defined as probe insertion to last biopsy, was calculated using meta-data stored in the biopsy device and was approximately 20 minutes. There were no appreciable differences in populations other than PSA, prior cancer diagnosis, and average number of prior biopsies. By definition, the second population consists of men with one or more prior negative biopsies and persistently elevated PSA, which accounted for the differences.

4.2.1 Cancer Detection

All data from the 18-month study were tabulated and analyzed at each level (visit, ROI, core) with regard to cancer detection. Results are given in Table 4.3.

	All	Previous Positive Biopsy	Previous Negative Biopsy
ROIs	352	219	133
ROIs targeted	296	181	115
Avg. # of suspicious areas	1.93	1.92	1.96
# areas positive for CaP	72 (24.3%)	48 (26.5%)	24 (20.9%)
Systematic cores positive	135/1862 (7.3%)		
Targeted cores positive	103/495 (20.8%)		

Table 4.3: Results using MR-US fusion for targeted biopsy. Cancer detection rate in targeted cores improved 3x over detection rates in systematic biopsy cores. Prospective grading of lesions seen on MRI produced a large number of false positives.

There were no cases of hospitalization for fever or sepsis after biopsy. On average, 13.4 biopsy cores were taken per patient. CaP was found using either method in 94 of 171 men (55%). Of these 90 men, 34 (38%) had Gleason ≥ 7. Thirty two cancers were detected only by systematic biopsy, 20 were detected only by MR-US targeted biopsy, and 42 were detected by both. For Gleason ≥ 7 disease, 9 men were diagnosed only with systematic, 14 only with targeted, and 8 for both. Prostate cancer was diagnosed on systematic biopsies in 6 of the 19 (32%) men with no ROI identified on MRI (3 Gleason 3+4, 3 Gleason 3+3).

Targeting accuracy was determined for each method by dividing the number of cores positive for any CaP by the total cores taken. Since both methods were utilized independently and from the same prostate, a paired signed-rank test was used (Mann-Whitney U). The low number of average targeted cores taken (1-4), precluded the use of a paired t-test. Targeted biopsy cores were more likely to harbor any cancer than systematic biopsy cores. 103/495 of targeted cores were positive for cancer

compared to 135/1862 of systematic cores (20.8% vs. 7.3%, $p = 0.001$). The number of cores positive for cancer in each method was the same (103 vs. 135, p=0.47), despite targeted biopsy having $\frac{1}{3}$ as many cores. This means that in our population, targeting suspicious areas increases the likelihood of finding cancer by three times, with using a fewer number of cores. When analyzed for serious cancers, defined here as evidence of Gleason 7+ disease, targeting still presented an improvement over systematic biopsy (7.7% vs. 1.6%, $p = 0.0003$).

Since each biopsy core was separately bottled, cancer lengths could be also independently analyzed. A student's t-test was used to compare the relative means of cancer found with each method. Figure 4.3 shows the means and standard deviations in targeted and systematic biopsy. The mean cancer length from cancer-positive targeted cores exceeded that from systematic cores (4.96 mm vs. 3.26 mm, $p = 0.007$).

Cancer was detected more often and in greater volume by targeted biopsy than by systematic biopsy. This finding serves to confirm the placement accuracy of the targeted biopsy cores. These two findings, number and length of cores involved by cancer, while important, only reveal a part of the relationship between targeted biopsy and cancer detection, as detailed in the following sections.

4.2.2 MR Performance

In order for fusion and targeted biopsy to be effective at detecting cancer, appropriate targets must be chosen on MRI. To this end, we examined the correlation between MR parameters and cancer severity. We analyzed the data by ROI location, aADC value, perfusion (DCE), and T2 score.

A total of 352 targets were identified in the 171 men, of which 296 (84%) were successfully sampled with at least one targeted core traversing the ROI. Nearly half of all targets were located in the central gland. Of these 147 ROIs, 35 showed cancer

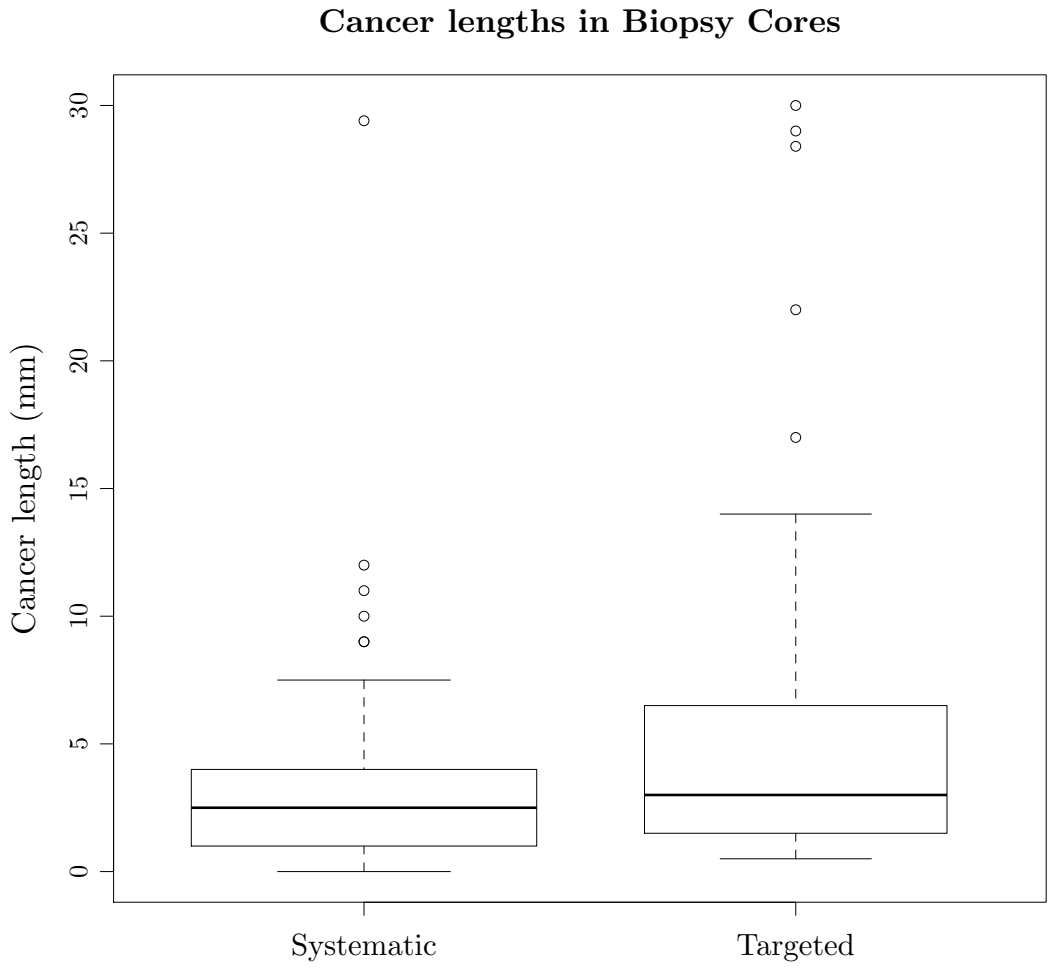

Figure 4.3: Cancer lengths in targeted and systematic cores. Mean cancer lengths from targeted cores exceeded lengths from systematic biopsy cores (4.96 mm vs. 3.26 mm, $p = 0.007$).

upon biopsy (23.8%). All MR parameters had median image grades of 3/5. Each ROI contained an average 2.3 cores, slightly lower than the 3 cores per target that were attempted. The MR scoring system was found to be correlated with the Gleason score on cancer found in targets, shown in Figure 4.4.

ROIs with an image grade of 2, 3, 4, or 5 were found to have a cancer detection rate

Variable	Result
Avg. # of cores per ROI	2.3
Central Gland ROIs	147 (49.7%)
Avg. Maximum Diameter	11.4 mm
Median Image Grade	3 (3.22 mean)
Median ADC	1079 (1063 mean)
Median T2 Score	3 (2.94 mean)
Median DCE Score	3 (3.04 mean)

Table 4.4: Summary of Regions of Interest. Average MR scores of 3/5 indicate that prospective scoring system was appropriately chosen for the patient population in our study. On average 2-3 cores per lesion were taken, with one core taken for every 3 mm of the ROI diameter. A high percentage of central gland lesions are expected as patients with large peripheral gland lesions are frequently screened out by prior conventional biopsy.

of 12%, 20%, 29%, and 58%, respectively. The rate of cancer diagnosis overall and the rate of detection of clinically significant CaP increased with increasing suspicion on MRI.

We then explored the correlation of each parameter to Gleason grade, a test of specificity. The ADC value was found to have a negative correlation with cancer positivity in target (r=-0.13, p=0.038). This was confirmed using a Spearman's rank correlation test. We also looked at the sensitivity of low ADC (< 800) to any cancer presence using a Fisher's Exact test, and found the same correlation with cancer positivity ($p = 0.00398$). The qualitative DCE score was found to be suggestive of correlation with Gleason score ($r = 0.11$, $p = 0.075$), while the T2 score was not ($r = 0.09$, $p = 0.156$). When the ADC values were classified according to the categories prospectively proposed, there was a correlation with Gleason grade ($r = 0.14$, $p = 0.025$).

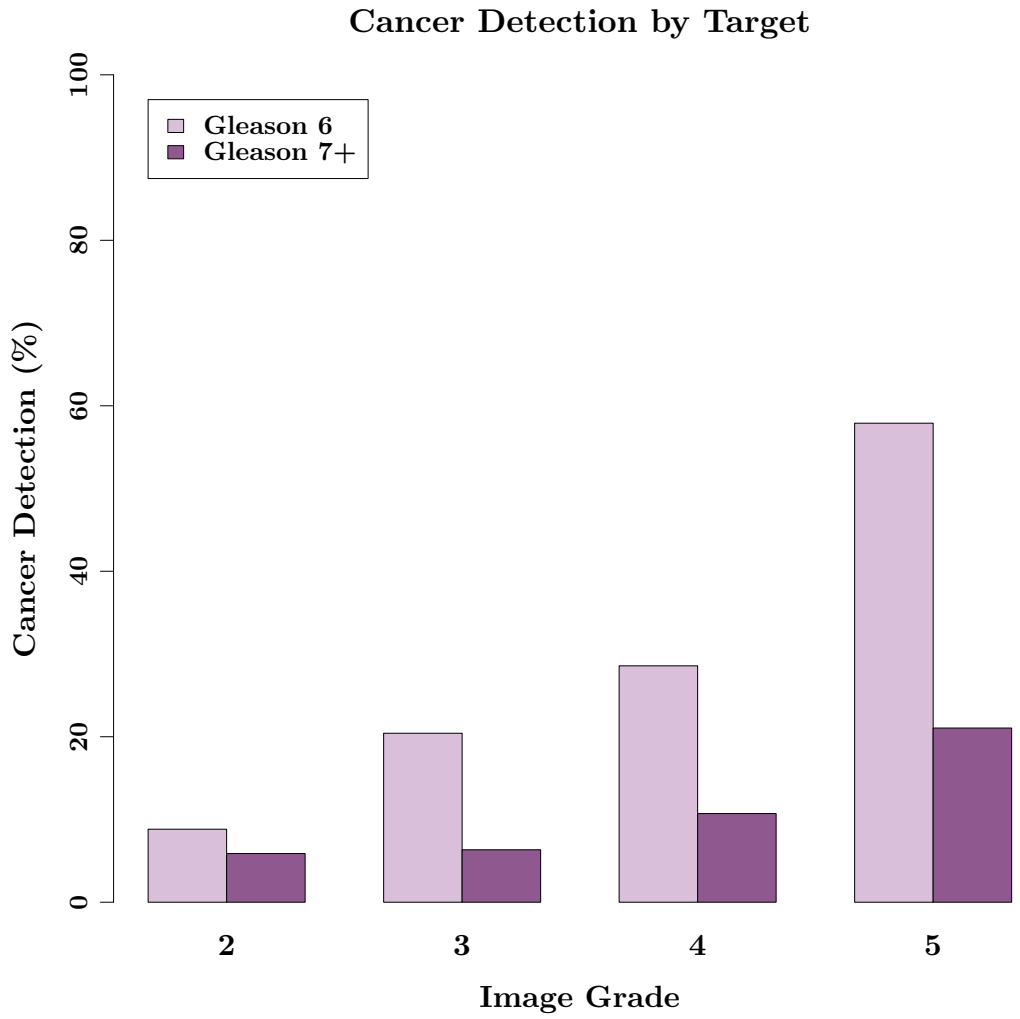

Figure 4.4: Cancer positivity for individual targets, grouped by image grade (MR findings). Total number of grade 2, 3, 4, and 5 targets were 34, 142, 84, and 19, respectively. Cancer positivity increased with image grade.

4.2.3 Volume Concordance

In order to better understand the effect of MR-US registration on diagnostic accuracy, we analyzed our findings with respect to prostate volume. It was hypothesized that discordance between reconstructed surface meshes from MR and TRUS would lead to

targeting errors. To this end, we compared TRUS volumes obtained through the semi-automatic segmentation and freehand method, with MRI. The standard method of prostate volume estimation is performed by measuring each dimension using freehand TRUS. The prostate is assumed to be a prolate ellipse, and volume is calculated with Equation 4.1.

$$\text{Prostate volume} = h \times w \times l \times 0.52, \tag{4.1}$$

where h is height, w is width, and l is the length of the prostate as measured on the sagittal and axial scanning planes on ultrasound. The scanning planes showing the great amount of prostate is used for calculation and is determined by the physician.

The software method (semi-automatic segmentation) involves a planimetric calculation, and is hypothesized to be a more accurate measure. The average deviation between the volumes obtained by planimetric and geometric calculation was found to be 7.8%.

When testing the concordances between MR and TRUS volumes obtained through the software method, there was no difference in volume size (45.64% vs 43.60%, p=0.91). This finding demonstrated that the software method performed identically in both image modalities. This is important in MR-US fusion, as gross volume differences could affect the validity of registration. When comparing the software and human methods of acquiring the volume in TRUS, a significant difference was found, representing a 7.8% underestimation by the geometric calculation ($p < 0.0001$). This error increased with prostate size. Figure 4.5 shows the MR volume compared to TRUS volumes obtained with both methods. The incidence of BPH is high in a population with negative biopsy and elevated PSA, which would complicate volume measure of the prostate. In such cases, a large medial lobe distorts the normal elliptical shape.

Prostate volume also appeared to affect the detection rates of targeted and system-

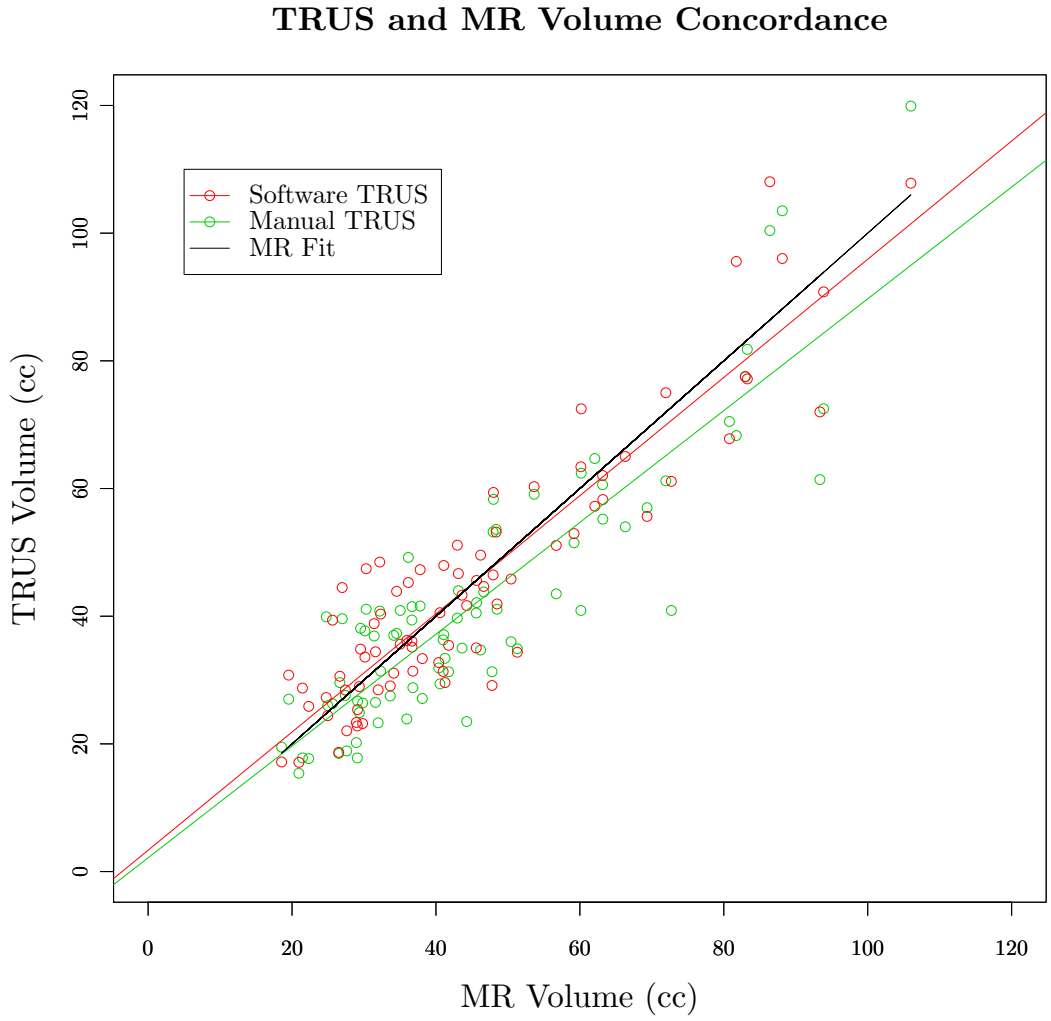

Figure 4.5: Volume differences with relative means. Manual prostate volume calculations (through the geometric method) consistently underreported true volume (defined as prostate volume on MRI). Software volume calculations in TRUS and MRI (planimetric method) were consistent, but both TRUS volumes drifted as prostate volume increased.

atic biopsy. Patients were grouped into three volume categories, less than 40 cc, 40–60 cc, and greater than 60 cc, in order to test normal, moderately enlarged, and greatly enlarged prostate volumes. Comparisons between all three categories were performed

using a two-tailed t-test with no assumption of equal variance (heteroscedastic).

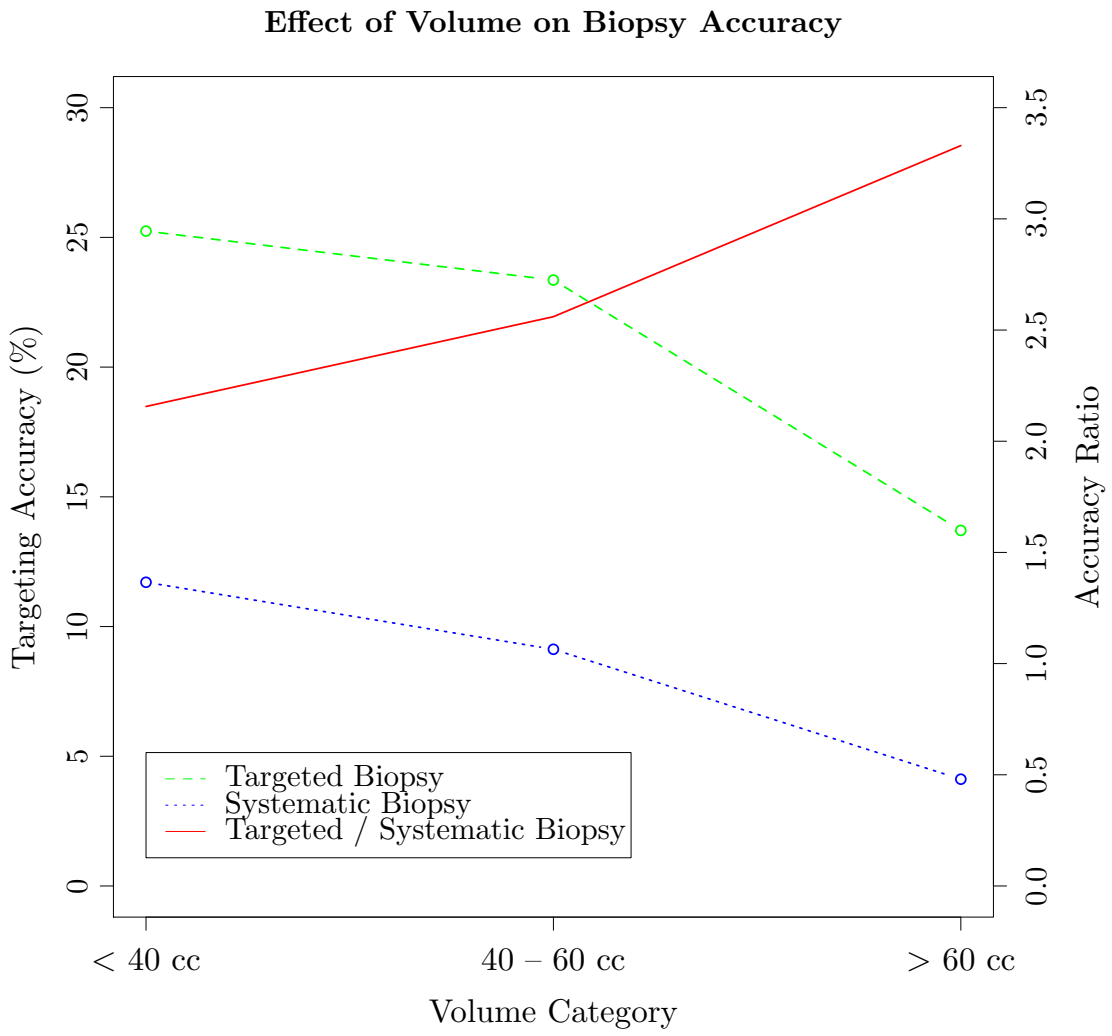

Figure 4.6: Effect of volume on biopsy accuracy. Targeting accuracy (green dashed line) decreased with volume, as did 3D systematic biopsy accuracy (blue dashed line). The relative improvement of targeted biopsy over systematic biopsy increased from 2x to 3.3x as prostate volume increased, indicating that although accuracy decreases with volume, targeted biopsy was still found to be superior to systematic biopsy.

Figure 4.6 plots all three categories, and the effect on cancer detection in both methods. In all three volume categories, targeted biopsy has superior accuracy com-

pared to systematic biopsy (see Figure 4.6, $p < 0.01$, $p < 0.01$, $p = 0.01$). This was primarily due to the significant drop in systematic biopsy accuracy for smaller to larger prostates (11.7% to 4.1%, $p < 0.001$). Also shown is the relative increase in biopsy accuracy of the targeted method as volumes increase, despite the absolute drop in accuracy.

The volume comparison highlighted the relatively poor performance in systematic biopsy with large prostates. Large prostates are sampled the same as small prostates, despite the lesser percentage of volume sampled in the former. Since our study deals with a low-risk patient population, patients with large cancers in areas normally sampled via 6- or 12-core TRUS biopsy are screened out. Cancers which exist in the central gland require needles to be inserted deeply into the prostate, a modification of current biopsy practice. It is also important to note that targeted biopsy performance degraded as well, suggestive of a general drop in accuracy with large volumes (25.2% to 13.7%, p=0.07).

4.2.4 Impact on Patient Care

In order for MR-US fusion to be useful for cancer diagnosis, predictive ability to detect cancer must be evaluated. To this end, cancer detection rate was analyzed according to the maximum image grade for each patient, shown in Figure 4.7. For example, the cancer detected in a man with both an image grade 2 and image grade 4 target, was analyzed according to the higher grade (grade 4) target. This test thus primarily looked at *sensitivity*. The non-parametric Spearman rank correlation was used to assess the relationship between image grade and the presence of cancer. 32% of patients without targets (6 men) were found to have cancer. Cancer positivity gradually increased in patients with maximum image grades of 2, 3, and 4 with 43%, 48%, and 56%, respectively. All but one man with an image grade 5 target (94%)

were found to have cancer.

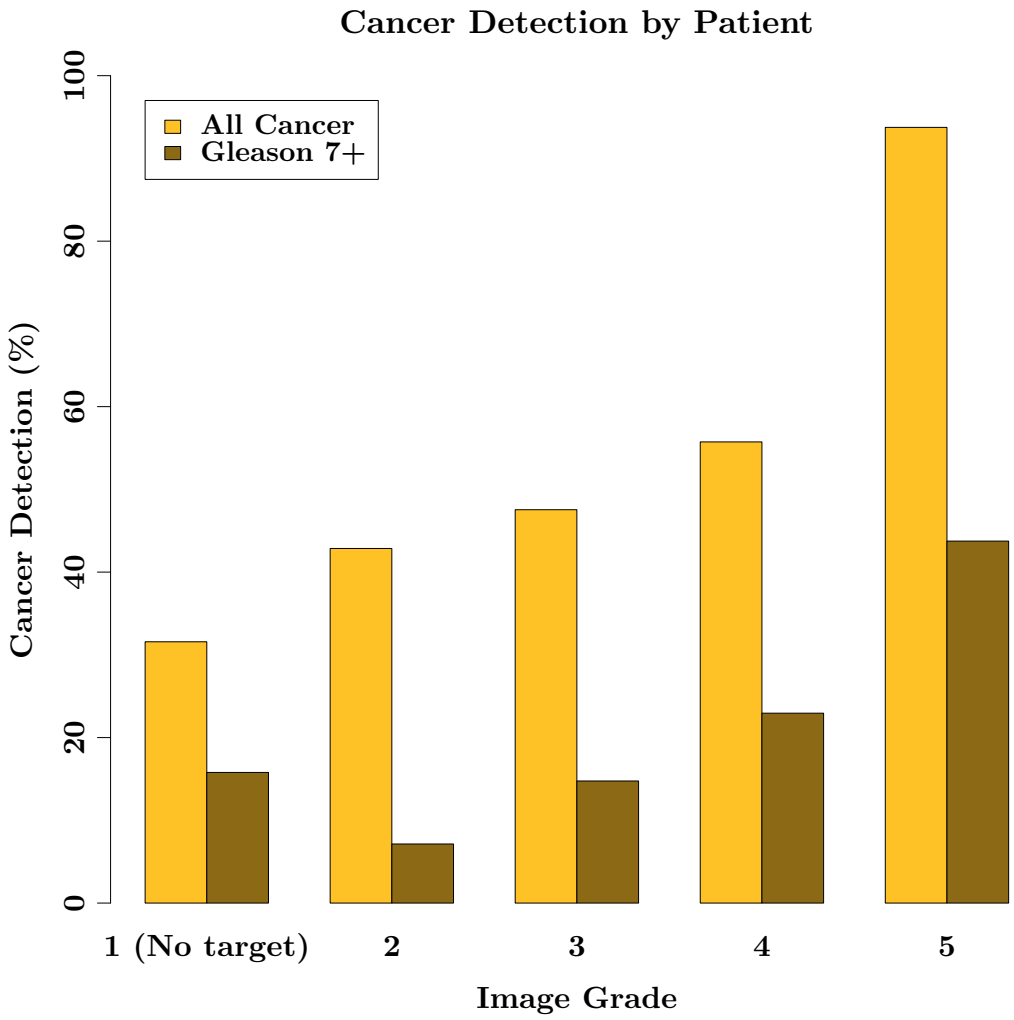

Figure 4.7: Cancer positivity for patient, grouped by highest image grade (MR findings). Total number of patients with a maximum image grade of 2, 3, 4, and 5 are 14, 61, 61, and 16, respectively. 19 patients did not have targets.

The sensitivity of targeted biopsy improved when there was a significant MR finding. Conversely, the similarity in accuracy between image grades 2, 3, and 4 indicated that the MR scoring system required refinement for a moderate level of suspicion. However, it is important to note that two different patient populations

were pooled in this study. In order to better understand the targeting accuracy in each sub-group, we repeated the previous analysis for men with prior positive biopsies, and men with prior negative biopsies.

Figure 4.8 shows the cancer detection rate in patients with prior positive biopsies, grouped by maximum image grade. In this group, the true cancer incidence was ideally 100%. However, many of these men harbored microfocal disease, so it was unclear how many substantial cancers were truly present. Conventional biopsy typically captures up to 25% of cancers on re-biopsy [166]. In the cohort in our study (median PSA 4.1), cancer detection with any method was 63%.

There appeared to be little difference between image grades 2, 3, and 4 in this sub-population. Although there was a moderate increase in the detection rate with Gleason ≥ 7 disease, the grading system did not accurately track the severity. In the active surveillance population, the goal of diagnostic biopsy is to determine if serious cancers are present. An increase in Gleason ≥ 7 diagnoses aids in keeping only those with truly low-grade disease in a surveillance program. As with the overall findings, distinct MR findings reliably predicted cancer detection. Every single man with an image grade 5 ROI was found to have cancer upon biopsy. The amount of Gleason ≤ 7 cancer increased as well.

This analysis was repeated for men with prior negative biopsies, seen in Figure 4.9. In this sub-group, true cancer incidence is unknown prior to biopsy. In literature, cancer detection rates for biopsy #2, #3, and #4 were found to be 10%, 5%, and 4% in patients with mean PSA of 6.7, 7.1, and 7.2 [167]. In this group, any cancer findings are important because it prompts action, either through surveillance for low grade disease, or radical treatment for serious cancers. In these men (median PSA 7.3), the rate of cancer diagnosis was 37%, three times greater than previously published findings [167], and improved over saturation biopsy protocols [168]. This increase in

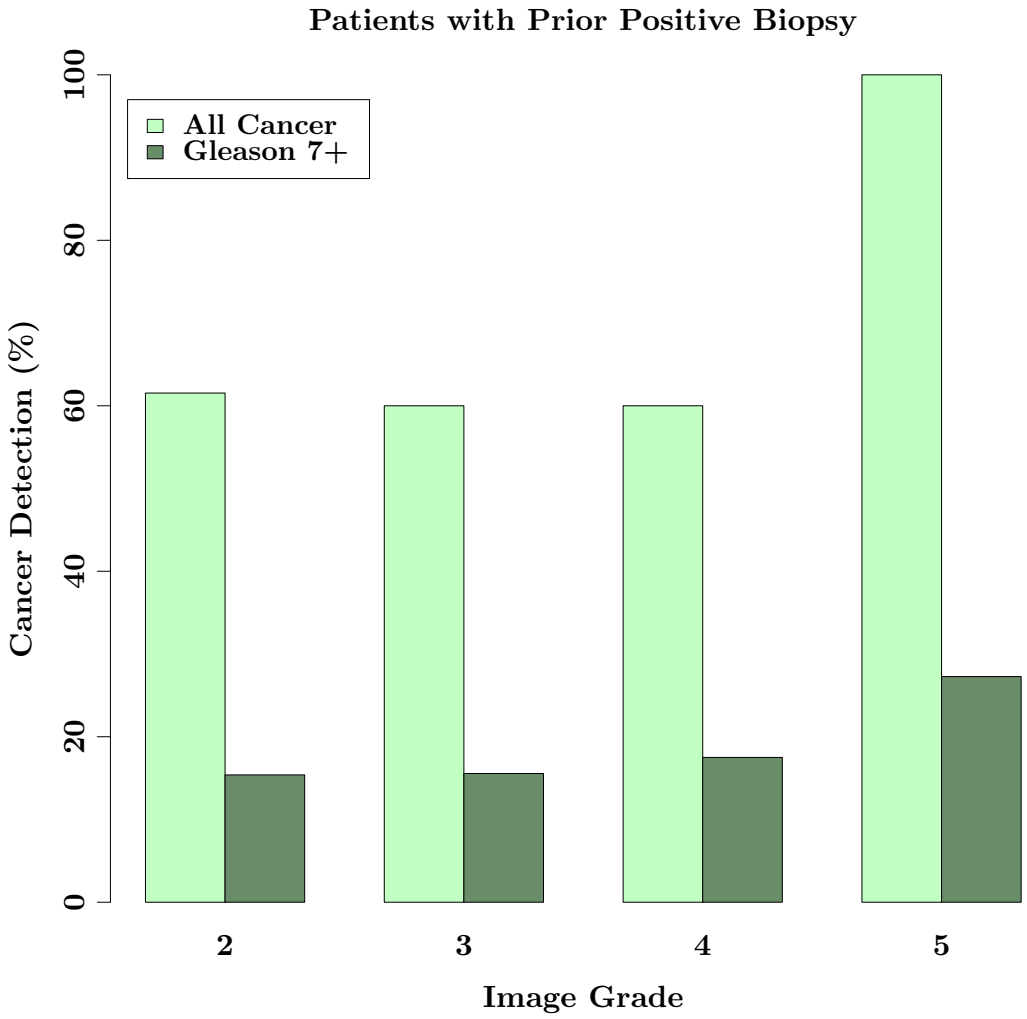

Figure 4.8: Image grade and cancer detection rate in men with prior positive biopsy. While all image grade 5 targets produced cancer, the indifference between image grades 2, 3, and 4 indicates that MR imaging and grading of lesions needs to improve.

diagnosis rate is in line with the 300% accuracy improvement in targeted cores vs. systematic biopsy cores.

In contrast to findings in the active surveillance patients, cancer findings in the repeat biopsy cohort were directly related to image grade. As with the ASCAP cohort, a high percentage of men with image grade 5 lesions were found to have

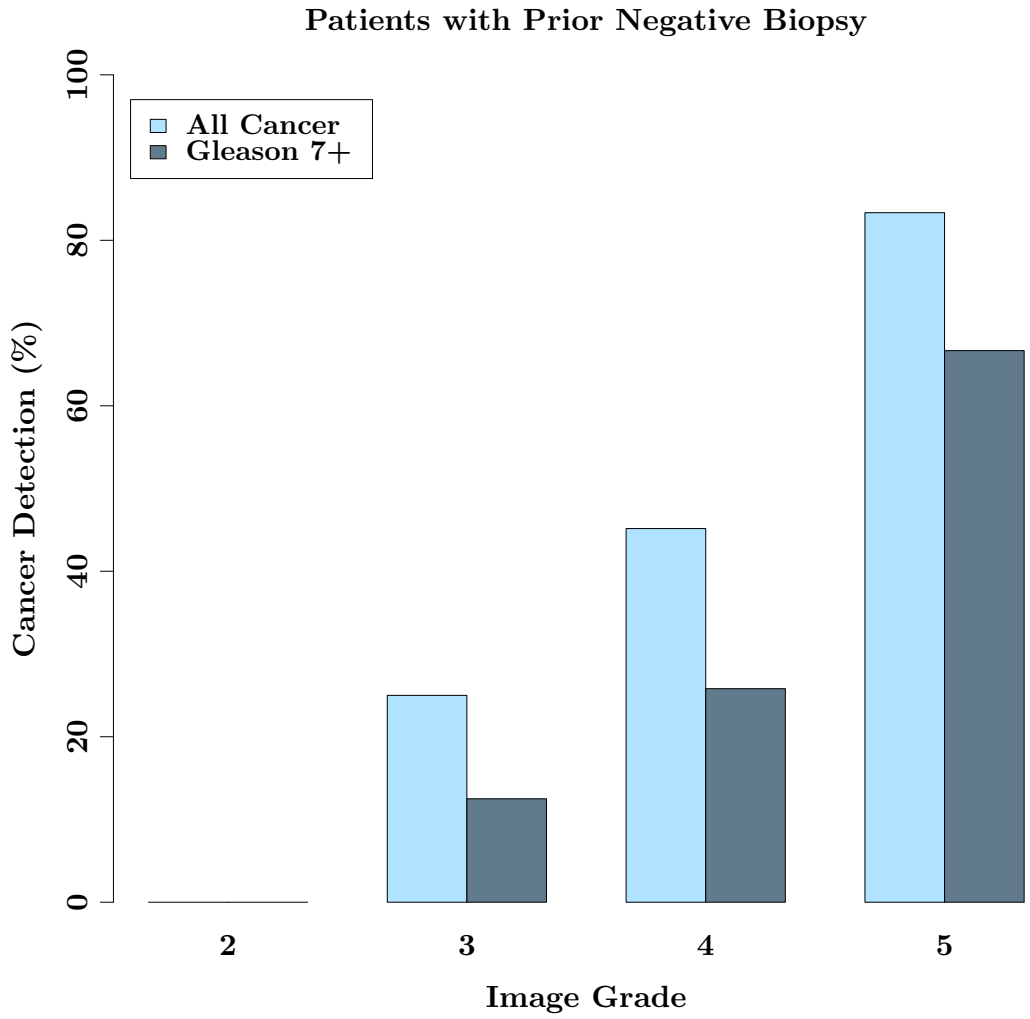

Figure 4.9: Image grade and cancer detection rate in men with prior negative biopsy and persistently elevated PSA. Darker bars represent Gleason 7+ cancers. MR was found to be sensitive and specific for cancer in this patient group. Image grade 2 found no cancer, and image grade 5 found predominantly serious cancer.

cancer. However, most of the cancers found were Gleason ≥ 7. Furthermore, the detection rate of Gleason ≥ 7 increased with each successive image grade. Cancer of any grade was not found in any patient with a maximum image grade of 2. The physical meaning of an image grade 2 ROI was typically a T2 (or morphological)

finding. This could help to explain the high false positive rate of prostate MR.

4.3 Whole Mount Prostatectomy Correlation

In both groups, targeted biopsy represented an improvement over systematic biopsy in detection of numbers and severity of cancer. These findings, however, only provide a comparison of the accuracy between the two methods. True anatomical correlation is required in order to validate MRI and targeted biopsy. In this study, a subset of men elected to receive radical prostatectomy (RP) as part of prostate cancer treatment.

Of the 171 patients who underwent MR-Ultrasound fusion biopsy and were diagnosed with cancer, 25 elected to undergo radical prostatectomy. After surgery, resected prostates were processed using the whole-mount sectioning method described in Section 3.1.3. Table 4.5 describes the pathology outcome and concordance with targeted biopsy.

$N = 25$

	Image Grade 2	**Image Grade 3**	**Image Grade 4**	**Image Grade 5**
Downgraded Gleason Score	0	1	1	0
Same Gleason Score	1	6	6	5
Upgraded Gleason Score	0	1	2	2

Table 4.5: Targeted biopsy correlation with whole mount prostatectomy. Out of 25 prostatectomies, two found serious cancer that was not accurately graded by biopsy. The majority of the cases (18/25) graded cancer accurately.

Of the 25 men who received prostatectomy, 7 (28%) had a a maximum image grade 5 lesion, 9 (36%) had an image grade of 4, 8 (32%) had an image grade of 3, and single patient had an image grade 2, which represented a non-enhancing lesion. Five out of 25 men (20%) had Gleason upgrading, 2 patients were downgraded, and

18 patients (72%) were accurately graded using targeted biopsy. However, of all 5 cases that were upgraded, serious cancer (defined as Gleason 7 and higher) was missed in only 2 patients. Gleason downgrading occurred in two men, and was likely due to differences in pathology interpretation between biopsy and prostatectomy.

More prostatectomies are needed before any strong conclusions can be made about the true accuracy of targeted biopsy. However, if confirmed, use of targeted biopsy to accurately predict final pathology could prove valuable in a low-risk population. For those men without a cancer diagnosis, there is also significant anxiety component since treatment might be unnecessarily delayed, or further biopsy is unnecessary [4]. If targeted biopsy better predicts true cancer incidence than existing method, compliance with active surveillance could be improved.

4.4 Sources of Error

In the results presented thus far, targeted biopsy with MR-US fusion was shown to improve diagnostic sensitivity and specificity over conventional biopsy. However, the discordance between ROI detection accuracy and overall biopsy accuracy in patients, demonstrates that combining both systematic and targeted methods offer the greatest advantage. A considerable number of significant cancers were missed by the targeted technique alone, and represented a failure with either the study methods, MR imaging, MR-TRUS registration, or targeting technique.

4.4.1 Modification of study methods

After the first six months of the study, we evaluated biopsy performance. From this initial analysis, we modified several aspects of the biopsy technique. We discovered that the patient positioning affected the quality of the 3D TRUS scan. To correct

for this, the probe insertion technique was adjusted so that the probe was parallel to the floor, reducing rotational distortion. Additionally, the patient positioning was modified to reduce motion during the procedure. The patient was placed in a left lateral decubitus position with patient's knees to the chest in a fetal position, restricting rotation motion.

Another source of error related to device operation (Artemis, Eigen). These studies represented the first clinical use of MR-TRUS with this device, and consequently, the hardware and software were often unstable, with technical failure of targeted biopsy in up to 20% of cases. This issue was resolved with an improvements in both software and hardware (Figure 3.2b). The updated hardware utilized a counter balance mechanism, instead of a counter-weight, which allowed for easier manipulation of the tracking arm, and increased the mobility of the device.

Qualitatively, we observed that in many cases the expected needle trajectory did not match the actual path. In part, we discovered that the procedure was being erroneously performed, due to the difficulty of 3D targeting. Many targets were not sampled simply due to the needle misplacement. We then amended the targeting procedure to use two orthogonal 2D views (sagittal and axial) instead. When using a 3D view, it was difficult to verify the accuracy of the needle. This mismatch between the expected and actual needle trajectory can be seen in Figure 4.10b.

Targeting accuracy was also also affected by the depth of needle placement. Current urological practice of transrectal biopsies target only the peripheral zone, and thus needles are deployed at approximately equal depth. Targeted biopsy requires the needles to be deployed at a depth unique to the individual target in order to ensure accurate sampling of the suspicious area. In our preliminary work, 41% of the lesions were located in the central gland, necessitating deeper insertion of the biopsy needle than with conventional biopsy.

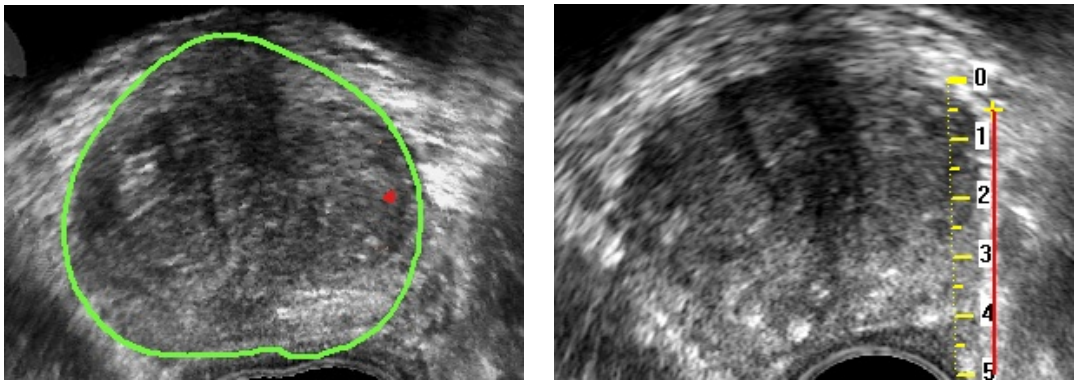

(a) Expected (b) Actual

Figure 4.10: Targeting error due to mismatch between (a) expected and (b) actual needle trajectory. The prostate in the (b) is rotated relative to (a), indicating a motion error, which caused the planned biopsy point to be missed (the actual sampled area was on the prostatic capsule). Expected trajectory is calculated from the 3D model, prostate segmentation, and planned biopsy points. Actual trajectory is from real-time ultrasound image capture during needle insertion. Numbers in (b) are placed along the automatically delineated needle (red line), and indicate relative depth in millimeters.

In order to evaluate the improvement expected from our modifications, we examined the accuracy of the targeted biopsy cores before and after the date of method change. Prior to method modification, the targeting accuracy was only suggestive of an improvement over systematic biopsy accuracy (22.0% vs. 7.3%, p=0.07). However, systematic biopsy produced cores more positive for cancer (28 vs. 9, p=0.004). After improvements were made to the targeting accuracy, 6 months after the study onset, targeted accuracy was found to be significantly improved over systematic biopsy (20.1% vs. 7.5%,$p < 0.0001$), despite having $\frac{1}{3}$ of the number of cores.

4.4.2 Influence of Secondary Variables

In order to better understand the contributions of various factors in cancer detection, a number of secondary variables were analyzed and compared to targeting errors.

Targeting errors were defined as cases where systematic biopsy produced a cancer specimen, but targeted biopsy was negative, or of a lower Gleason score. For example, if targeting an ROI found Gleason 3+3, but Gleason 3+4 was discovered upon systematic biopsy in the same patient, a 'miss' was indicated. Cases where targeted biopsy and systematic produced the same result counted as a 'hit', since targeting accurately indicated the highest Gleason grade in the biopsy session. Univariate analysis was used to measure the following factors: PSA, prostate volume, volume difference between MR and TRUS, age, days between MR and biopsy, ROI size and location, number of previous biopsies, and previous positive biopsy, Additionally, we retrospectively verified the needle position on every biopsy sample, and tabulated the instances where the needle missed the expected target position in 3D. This verification involved visually comparing the TRUS images acquired during each needle deployment with the TRUS image produced by software. If the actual needle position (given by the real-time TRUS image) did not match the expected position (calculated by the software) and was not located inside the ROI, an error was recorded. Results are given in Table 4.6.

Factors that appeared to affect biopsy targeting included PSA, prostate volume, volume difference between MR and TRUS, cancer zonal location, and previous positive biopsies. Several of these factors can be explained by association with the active surveillance cohort. A definition of this patient group is the presence of a previous positive biopsy. Moreover, this group had a lower median PSA than the men with negative biopsies.

Targeting was more accurate in mid-sized prostates (i.e., volumes of 40-60 cc) than in prostates outside that range. Multi-variate analysis is required to better understand this relationship, as men on active surveillance had a lower median prostate volume (40.9 cc) than others (51.6 cc).

	Variable	Significance
Patient Factors	PSA	$p = 0.0018 **$
	Age	$p = 0.52$
	Previous positive biopsy	$p = 0.0125*$
	Number of previous biopsies	$p = 0.192$
	Interval between MR and Biopsy	$p = 0.83$
Volume Factors	Small prostate volume	$p = 0.012*$
	Volume difference between MR and TRUS ($\frac{V_{\text{TRUS}} - V_{\text{MR}}}{V_{\text{TRUS}}}$)	$p = 0.0036 **$
MR Factors	ROI size	$p = 0.11$
	Apical location	$p = 0.73$
	Peripheral gland location	$p = 0.0157*$
	Right side location	$p = 0.81$
	Mistargeting in 3D view	$p = 0.06\bullet$

Table 4.6: Correlation of biopsy and patient factors with targeting errors. Registration was found to be problematic in our study, with errors in targeting associated with prostate volume, volume difference between MR and TRUS, a peripheral gland location, and prostatic or patient motion during the procedure.

Accuracy was also related to volume differences between MR and TRUS measurements. In cases where the TRUS volume was smaller than the MR volume, accuracy decreased. The image registration used between MR and TRUS involves semi-automatic segmentation, and thus mismatch in volume size could affect ROI placement. If a target was located very peripherally, inaccurate segmentation in the target area shifted the ROI to the central gland, where cancer is less likely.

We also discovered that misplacement of needles within target areas was a significant factor in biopsy targeting, and reduced accuracy of cancer diagnosis. This was found through the retrospective visual verification that was previously described. Even with the modified technique, hitting a target precisely in the expected sampling area was difficult, which highlights the importance of motion and needle tracking during targeted biopsy.

Other major factors that can influence biopsy accuracy are MR-US registration

and biopsy tracking. In order to evaluate the cumulative effects of alignment and registration errors, biopsy results were re-tabulated to factor in instances where the MRI showed a target, and the systematic biopsy in the target area was positive. This is different from mistargeting errors, because ROI locations are dependent on MR-US alignment and non-rigid mapping. When recalculated, the number of patients with missed cancers dropped from 31 to 12, and the number of patients with serious cancers missed drops from 10 to 3. On these three patients, the point of failure was the MR imaging, as areas with cancer did not appear suspicious. These results are encouraging, as errors are primarily related to image registration, biopsy tracking, and target selection. The addition of MR imaging was beneficial in almost all cases.

4.5 Discussion

The data in our study clearly supports the value of MR-US fusion in prostate cancer diagnosis. However, the data also show that systematic biopsy remains necessary for complete evaluation, especially in patients undergoing active surveillance.

Clinical Utility

We studied two groups of men, patients on active surveillance and patients with prior negative biopsies. The first group had 63% cancer positive rate compared with 37% in the second group. In a program of active surveillance, it is important to not only diagnose the patient appropriately, but also track the progression of a previously found cancer. Targeted biopsy enables a new approach to active surveillance. First, the previous biopsy site can be revisited, and disease progression can be tracked *in situ*. Second, positive targets can be tracked in MRI, and comparisons between ADC and perfusion values could either delay or hasten follow-up biopsies. While image

grades 2,3, and 4 did not reliably distinguish between serious and non-serious cancer, image grade 5 lesions were almost always positive. This means that a certain number of lesions, which are reliably cancerous, can be detected on MRI.

The cancer diagnosis rate on men with prior negative biopsy and elevated PSA (mean number of previous biopsies = 2.3), exceeded the diagnosis rate from conventional biopsy [168, 169]. This dramatic increase in our positivity rates over published rates demonstrates the advantage of targeted biopsy in finding cancer. In these men, diagnostic accuracy is important as it would hasten treatment for clinically significant disease. Furthermore, anxiety is a major component of this patient group, and a definitive diagnosis would be informative [4, 5]. Several men in our study had more than 4 prior negative biopsies before receiving a cancer diagnosis through targeted biopsy.

MR was shown to accurately predict biopsy outcome at both ends of the image grade scale. Patients with an image grade 5 lesion almost always harbored cancer, usually a clinically significant disease. Use of this information could lead to MR-based screening for serious cancers. Conversely, cancer was not detected in patients with a maximum Grade 2 target. Perhaps in this subset, patients could forego biopsy altogether. While the diagnostic rate for overall and significant cancers increased for image grade 3 and 4, it is less clear how this information could alter clinical workflow, beyond a cancer risk assessment. In these patients, a targeted biopsy is advisable. However, when looking at the correlation between targeted biopsy performance with whole mount prostates there was not significant Gleason upgrading.

These results show the advantage of MR-US fusion in prostate cancer diagnosis. The associated errors with image transformations (i.e. segmentation, registration, and tracking) were demonstrated to be less than 4.9 mm, the minimum diameter of a clinically significant lesion, under the original 5 mm (0.5 cc) cutoff proposed

by Stamey in 1993. Newer criteria define a significant lesion as large as 1.3 cc, corresponding to a diameter of 7 mm [170]. Using either of these criteria, targeted biopsy was able exceed the minimum requirements. However, others have proposed a greater required accuracy (3 mm), by applying computational methods [171], although this may change with different patient groups [172] and biopsy strategies [173]. In individual patients, errors related to the initial 3D scan of the prostate significantly affected the final outcome. Furthermore, targeted biopsy appeared to be difficult on patients with asymmetric prostates, or those with defects from a prior transurethral resection of the prostate (TURP).

Perhaps the most important finding from these tests is that Gleason scores alone do not tell the whole story of disease progression. When biopsy findings were analyzed with cancer length as a co-variate, targeted biopsy was superior to 3D systematic biopsy. The performance of 3D systematic biopsy might also be influencing the overall results since it may offer a more accurate sampling of the prostate [131, 132, 172, 174, 175]. One study found an 8.86 mm needle placement error associated with freehand sextant biopsy [176]. A randomized prospective trial directly comparing 3D systematic biopsy to freehand TRUS biopsy, would aid in determining the relative improvement of 3D biopsy.

Comparison with Other Studies

While this study demonstrates the efficacy of MR-US fusion biopsy in a low risk population, it only represents one of many explorations needed to confirm the use of targeting for all patients with suspected or confirmed CaP. There have been numerous other studies utilizing MR-guided biopsy, transrectal MR-US fusion biopsy, and transperineal MR-US fusion biopsy (see Tables 4.7 and 4.8).

Our work focused on a men with a low risk of harboring serious CaP, and results

matched those in other studies. We found that targeted biopsy cores were more likely to harbor CaP than systematic cores, at an average detection rate of $\tilde{2}1\%$, confirming prior work in similar patient groups [126, 138, 148]. Low ADC values were also found to correlate with significant CaP [112, 177, 178]. Our MR scoring system was also similar to those by other groups, and yielded similar results irrespective of patient population characteristics [111, 138, 142, 148, 154].

The results from the work presented in this thesis were also comparable to those from previous studies using MR-guided prostate biopsy. Previous work using a Siemens Invivo biopsy device and an endorectal coil (EC) found a 20-30% cancer positivity rate for all targets, compared to our rate of 24.3% [111, 112]. Furthermore, the authors found that cancer positivity increased as suspicion level (low, moderate, and high CaP suspicion) increased [111]. A followup study at Neijmegen found a CaP detection rate of 59% in patients with prior negative biopsies, with most lesions harboring clinically significant disease [98, 113]. CaP detection in very suspicious lesions (image grade 5) was similar to our rate (58%).

MR-Guided Biopsy Devices

Group	MR Protocol	# of Patients	PSA	CaP Detection
Brigham and Women's Hospital [179, 180]	1.5T EC, DWI, DCE, T2WI, Spec	46 (all $\geq$ 2 PNBx)	13.8 $\frac{ng}{ml}$ (mean)	19/46 (38%) Targeted,
Johns Hopkins University [110]	3T EC, DCE, T2WI	13 (all PNBx)	4.9 $\frac{ng}{ml}$	1/13 Targeted, 1/47 ROIs
Humboldt-Universität zu Berlin / Daum [111]	3T EC, T2WI	12 (9 PNBx, 2 PPBx, 1 IBx)	10 $\frac{ng}{ml}$	5/12 (41.7%) Targeted, 12/60 (20%) ROIs
Siemens Invivo [112]	1.5T EC, DWI, DCE, T2WI, Spec	54 (all PNBx)	12.1 $\frac{ng}{ml}$	21/54 (39%) Targeted, 53/178 (29.8%) ROIs
Neijmegen [98, 113]	3T EC, DWI, DCE, T2WI, Spec	68 (all $\geq$ 2 PNBx)	13.0 $\frac{ng}{ml}$	40/68 (58.8%) Targeted, 46/114 (40.4%) ROIs

Table 4.7: Overview of clinical studies using MR-guided biopsy for CaP diagnosis. Patient groups are those with prior negative biopsy (PBx), prior positive biopsy (PPx), and those undergoing initial biopsy (IBx).

Despite the similar detection rates with MR-US and MR-guided biopsy, the former can be performed in 15-20 minutes for 15-18 cores versus a 30-90 minute procedure time for the latter [109]. Furthermore, current commercially available MR-guided biopsy devices require patients to be slid out of the MR gantry every time a core is taken, potentially introducing errors [111].

Clinical work with MR-TRUS fusion was notably performed at the NIH using a 3D biopsy device with an external magnetic field generator to track and target ROIs [90, 125]. Initial studies with this device, PercuNav (Philips), found a 37% CaP detection rate in a heterogenous patient group using systematic biopsy only (PSA of 8.8 $\frac{\text{ng}}{\text{ml}}$), and that T2WI + DWI alone was retrospectively indicative of cancer [146]. A follow-up study prospectively targeted ROIs seen on T2WI alone, and discovered a 9.3% CaP detection rate in targeted cores [87]. The low CaP detection rate, compared to our study, was likely a result of the MR protocol used, as T2WI alone has been repeatedly shown to be a poor predictor of CaP [144, 154, 181].

Recent studies adopted an mpMRI protocol and examined a larger patient group (N=101), which helped show a relationship between prospective risk and MR scoring [127,148]. They noted a 6.5% cancer positivity rate in low-grade ROIs, and an increase by a factor of 6.5 in patients with highly suspicious lesions [126]. Despite the lower median PSA in our patient group (5.4 vs. 4.9 $\frac{\text{ng}}{\text{ml}}$), our study found more CaP in both low-suspicion (image grade 2) and high-suspicion (image grade 5) ROIs (8.8% and 57.9% respectively).

MR-US Fusion Biopsy Devices

Group	MR Protocol	# of Patients	Median PSA	CaP Detection
Kaplan et al. [130]	1.5T EC, T2WI	2 (post-radiotherapy)	Unspecified	2/2 (100%) Targeted
Miyagawa et al. [128]	1.5T DWI, DCE, T2WI	85 patients (all $\geq$ 1 PNBx and/or PPBx)	9.9 $\frac{ng}{ml}$	61% Targeted + Systematic vs. 53% Targeted
Pinto et al. [126, 127, 148]	3T EC, DWI, DCE, T2WI, Spec	101 (29 PNBx, 36 IBx, 36 PPBx)	5.4 $\frac{ng}{ml}$	54% Targeted + Systematic vs. 45% Targeted
Hadaschik et al. [138]	3T DWI, DCE, T2WI	106 (49 PNBx, 46 IBx, 11 PPBx)	8.0 $\frac{ng}{ml}$	59.4% Targeted + Systematic vs. 47/106 (44%) Targeted
Fenster et al. [142]	3T EC, DWI, DCE, T2WI	25 (14 PNBx, 11 IBx)	8.3 $\frac{ng}{ml}$ (mean)	32% Targeted + Systematic vs. 24% Targeted
This thesis [177]	3T DWI, DCE, T2WI	171 (65 PNBx, 106 PPBx)	4.9 $\frac{ng}{ml}$	55% Targeted + Systematic vs. 34% Targeted

Table 4.8: Overview of clinical studies using MR-US targeted biopsy for CaP diagnosis. Patient groups are those with prior negative biopsy (PBx), prior positive biopsy (PPx), and those undergoing initial biopsy (IBx)

One explanation for this difference might be that slightly more biopsy cores per target were taken. In the NIH study, 2 cores per ROI were taken, while we sampled every 3 mm of an ROI (with an average of 2.3 cores per ROI). Differences associated with the mpMRI protocol might have also caused this discrepancy. Moreover, our methods utilized a system with a physical tracking mechanism [139,141], and were less influenced by environmental factors, but were technically challenging to operate [177].

None of the fusion-based targeted biopsy studies undertaken in the literature attempted to quantify the errors associated with image registration in a clinical context. In fact, it was previously noted that CaP missed by targeted biopsy is not well understood [148]. Our work explored the various factors that influenced fusion, and caused an ROI to be mistargeted.

Limitations

This work had several limitations related to study design, MR performance, image registration, and biopsy tracking. First, the true incidence of cancer is unknown amongst this patient group. Due to the short time of study and selection of a low-risk population, relatively few men underwent radical prostatectomy subsequent to biopsy. Furthermore, the short study duration yielded little follow-up data, which would be helpful to record the long-term impact of MR-US fusion imaging and targeted biopsy. While we can estimate the number of significant cancers found, the long-term prognosis of patients with negative targeted biopsies is unknown.

MRI was shown to be correlated with cancer positivity and severity. Significant cancer (Gleason $\geq$ 7) was missed by MRI on only three patients. However, the scoring system that was developed lacked distinction between image grade 3 and image grade 4. Moreover, there were a small number of serious cancers that were assigned an image grade of 2. These limitations could be due to lack of resolution of

MRI, or physiological characteristics of the disease since there are cancers that are not enhanced on perfusion or diffusion-weighted imaging, especially in the transition zone [182, 183]. Further development of MR imaging protocols specific to prostate cancer will create a standardized and optimal scoring system [98, 181]. At time of writing, there is an active multi-center effort which aims to answer this very question [154, 181].

The MR-US registration analysis was limited, due to poor quality of fiducial visualization on TRUS. If fiducial locations could be confidently identified, registration accuracy might be different than what was measured. Furthermore, the 3 mm registration error estimate was based only on six patients. Further studies which look at more patients, with a larger variance in prostate volume would give a better estimate of *in vivo* target registration error.

In the current fusion imaging regimen, systematic biopsy cores in addition to targeted cores are needed in order to make a definitive diagnosis. The need for both biopsy methods represents a major limitation. While fusion imaging dramatically increased both sensitivity and specificity of cancer detection, there were a number of serious cancers that were missed due to limitations with MRI, image registration, and targeting.

TRUS visualization of the prostate was found to be important in targeting peripheral lesions. In order to get a quality 3D scan of the prostate, it was necessary to repeat the scanning procedure up to 3 times in some cases, which added 3-5 minutes to the biopsy procedure for each additional scan. The quality of the scan was important in order to get an accurate segmentation. Furthermore, alignment with the MR was difficult to perform when the scan quality was poor.

In our study, we observed a 58% positivity rate when targeting grade 5 lesions, but a near 100% rate when combining systematic and targeted biopsies in patients with a

grade 5 target. This discordance is likely due to mistargeting of the suspicious areas. In the current procedure, the prostate MR and Ultrasound are manually aligned by identifying corresponding anatomic landmarks. However, axial images do not have any readily identifiable landmarks, and thus a rough guess of the prostatic boundary was used. A method which does not require manual alignment would improve the accuracy of fusion biopsies.

Another limitation of targeting accuracy was the ability to scale with prostate volume. Even though targeted biopsy improved cancer detection over systematic in all prostate volume categories, the overall diagnosis rate decreased as volume increased. This might be explained by the presence of a large central gland due to extensive BPH, characteristic of this patient population. Volume differences for large prostates have been observed elsewhere [98, 184]. Morphological differences between the MR and TRUS segmentations, despite having the same overall volume, would hamper the ability to accurately perform fusion imaging. Moreover, biopsy needles must be inserted deep into the prostate for anterior targets, which would compound the error. If the 3D deformation of the prostate could be known in real-time, then errors due to visualization and needle deformation might be avoided [185, 186]. Follow-up studies with this technology are needed to accurately characterize this effect.

Smaller prostate volumes were also correlated with failures in targeting. In such prostates, misalignment errors between MR and TRUS are exacerbated, leading to larger registration errors. Volume mismatch between MR and TRUS also led to targeting errors, indicating the importance of the quality of TRUS imaging and segmentation method.

Motion during biopsy was also another factor that was measured in a subset of cases. A software function in the biopsy tracking device allowed for dynamic compensation of prostate motion. However, this function only tracked in-plane motion

(i.e. body movement by the patient), and thus could not be used to fix gross motion errors. Prostatic motion within the body is also unaccounted for. Again, a real-time 3D imaging method could provide dynamic information about prostate motion and would potentially improve biopsy tracking.

In spite of these limitations, targeted prostate biopsy using MR-US fusion was shown to improve CaP detection rate of serious cancers. The similar results with other studies using alternative fusion technologies shows the benefit of MR-US fusion in prostate cancer diagnosis. Furthermore, by demonstrating the utility of fusion and targeted biopsy in a low-risk population, *over treatment* of prostate cancer could be reduced. Ultimately, in order for targeted biopsy to be effective as a stand-alone diagnostic, improvements are needed in ultrasound and MR imaging, and targeting method.

Chapter 5

Transurethral Ultrasound Imaging

The previous chapter showed the promise of MR-US fusion for prostate cancer diagnosis, despite limitations in the imaging technique. A method that reduces errors related to motion and image registration would enable MR-US fusion to be used in lieu of a systematic biopsy. This section explores how these limitations might be overcome using an alternative method for ultrasound acquisition, transurethral ultrasound (TUUS).

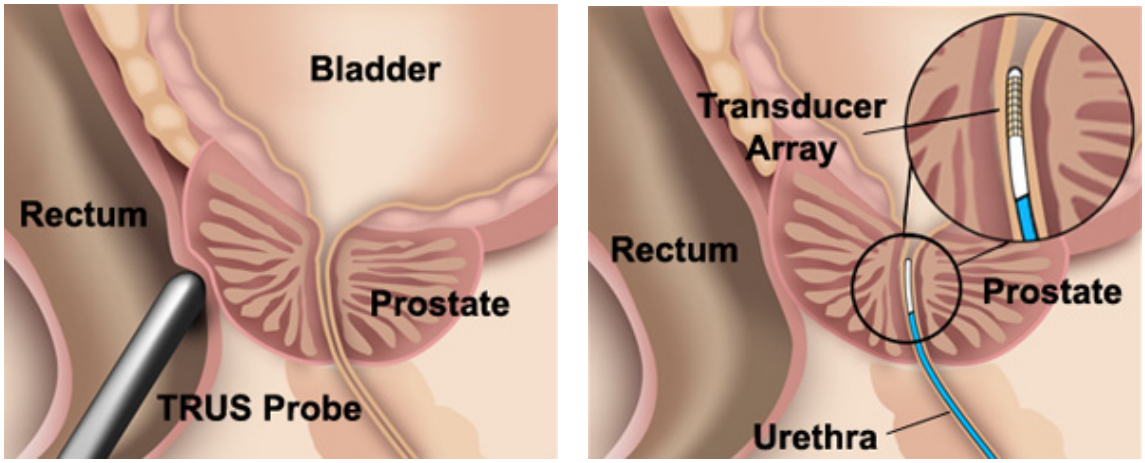

(a) TRUS (b) TUUS

Figure 5.1: Comparison of (a) transrectal ultrasound (TRUS) with (b) transurethral ultrasound (TUUS). In TRUS, the transducer is placed external to the prostate, and must be stabilized during scanning. In order to acquire a quality image, the probe must be pressed against the rectal wall which in turn deforms the prostate. TUUS allows the transducer array to be left alone during scanning, which reduces motion artifacts and potentially improves image registration with MRI.

TUUS imaging was first described for prostate and bladder imaging in 1974, and

used a rigid 4.5 MHz probe [187, 188]. Early work involved comparing clinical images taken with TUUS and TRUS [189], originally implemented using a chair-type scanner [29, 190]. Later studies used TUUS to explore bladder tumors [191–194] and their co-localization in MR, CT, and TUUS using the same rigid probe [195]. A 12.5 MHz rotating probe was subsequently investigated for imaging of the urethral rhabdosphincter [196]. Later work used a catheter-based transducer array, similar to intravascular ultrasound (IVUS) [197, 198].

The central location of the TUUS probe would enable higher frequencies, and consequently higher resolution imaging. Additionally, the probe location within the prostatic urethra is hypothesized to reduce or eliminate the need for motion compensation. Furthermore, prostate morphology might be less influential on image quality as large prostates were found to be detrimental to targeting accuracy. An imaging system which combines transrectal needle insertions with TUUS imaging, could improve the accuracy and reliability of prostate biopsy. Moreover, the miniaturization or elimination of the TRUS probe would potentially reduce patient discomfort.

We investigated the development of a transducer array that contains elements both wrapped circumferentially around a catheter, and linearly along the length of the catheter. With such a device, real-time 3D imaging would be enabled through multiple scanning planes. Figure 5.1 illustrates the difference between TRUS and TUUS imaging for the prostate.

In order to determine the feasibility of MR fusion with transurethral ultrasound, we attempted fusion using a commercial intravascular ultrasound (IVUS) transducer (Visions, Volcano Therapeutics). This transducer contained elements operating at 9 MHz, radially spaced along the circumference of an 8.2 F (2.8 mm) catheter.

5.1 Explorations of Catheter-Based Ultrasound

Although clinical studies utilizing large rigid TUUS probes (23F) have been reported recently [199], flexible catheter-based TUUS would allow for improved resolution and smaller diameters (5-18F) [198, 200, 201]. Much of the current interest in catheter-based imaging is found in intravascular applications.

A number of catheter-based intravascular ultrasound imaging (IVUS) systems currently exist, and fall into two categories: (1) linear, phased-array transducers and (2) single-element transducers which mechanically rotate [202]. Linear phased-array transducers, or longitudinal transducers, are mounted on the side of a catheter and use electronic beam steering [203]. Although these catheters are capable of high quality imaging in the longitudinal direction (perpendicular to the catheter shaft), the catheter must be manually rotated in order to obtain a cross-sectional (axial) image. Examples of current commercial systems in this category include the family of Siemens Acuson systems, and Volcano Therapeutic Vision systems.

In contrast, single-element rotational transducers use a mechanical drive shaft to spin 360° [204]. These arrays capture axial images with high quality, but must be manually pulled, or translated, in order to obtain longitudinal image information. This operation is known as mechanical pullback, as the catheter is inserted to the end of the target region, and then pulled back towards the point of insertion. Examples of current commercial systems that use this approach include the Boston Scientific Ultra ICE and Atlantis systems, and the Volcano Therapeutic Revolution systems.

IVUS catheters that feature automated rotation have yielded higher quality axial images than phased array IVUS transducers, but are susceptible to both rotational and linear distortion and have complex construction [205, 206]. A study evaluating non-uniformities in rotational velocity observed a 700% rotational velocity variation

with one mechanical system, leading to random errors in measurements [207]. Phased array transducers are immune to such inconsistencies in the longitudinal direction and are easier to set up and operate [208]. However, they do not provide axial information and have limited acoustic power and resolution [209, 210]. Efforts to improve rotational imaging have focused on gating image slices [211, 212], yet fail to address the challenge of registration between cross sectional images.

Figure 5.2: Intravascular ultrasound (IVUS) transducer used in studies in this chapter (Visions, Volcano Therapeutics, Rancho Cordova, CA). IVUS transducers are typically single- or multi- element linear arrays that mechanically rotate to create a 360° image, whereas the transducer used in our studies was radially phased (gold section in figure), with 64 elements placed around the circumference of the catheter.

Transurethral imaging studies using IVUS catheters have been explored by many groups [197,213–215], but have predominantly focused on imaging of the bladder. One study by the Mayo clinic used commercially available IVUS catheter-based transducers, to image the prostate in 3D [216]. Investigations by this group involved 10.0 MHz, 10F IVUS systems that featured linear phasing (AcuNav, Acuson) and mechanical rotation (ICUS, Boston Scientific) [198, 216, 217].

As in previous linear phased array IVUS studies, the AcuNav device required manual rotation to produce 3D imagery. In the TUUS experiments, manual rotation resulted in frequent non-uniform rotational distortion (NURD) and catheter twist during image capture [198].The authors concluded that the Acunav transducer was not optimal for transurethral applications, and that a redesign was required to improve 3D imaging [216].

The single-element Boston Scientific ICUS device was found to have an axial resolution of approximately 0.3 mm at a field of view of 6 x 6 cm^2 [198, 217]. However, as with prior work in IVUS, a constant pullback velocity was required to obtain 3D TUUS volumes. A constant pullback rate was difficult to achieve and limited lateral resolution of the images when they were reconstructed in 3D [218]. An additional practical drawback was patient discomfort associated with frequent rotation or translation of the transducer within the urethra during imaging. The same group also published work on image processing and reconstruction techniques for TUUS [198, 218, 219]. Due to noisy, specular reflections, common intensity-based registration schemes were ineffective and thus images were manually registered to create a 3D prostate volume [218].

Even when limited by manual translation or rotation, TUUS was found to improve resolution and localization of prostate features over both CT and TRUS [218]. Transducers that do not require any rotation could further improve the quality of intravascular imaging [208]. To this end, one early group developed a 16-element circular IVUS transducer [202, 220, 221], in which radial, rather than linear, phasing was used. A radially phased TUUS array may exploit curvature of the catheter to reduce imaging artifacts [208, 222, 223], such as those caused by calcifications near the urethra [213]. The study described in this chapter explored 3D TUUS imaging using a 64-element radially-phased IVUS transducer.

5.2 System Description

In order to evaluate the feasibility of 3D TUUS imaging and MR-TUUS registration using a radially-phased array, we performed an *in vitro* phantom study. Multi-modal prostate phantoms were constructed and imaged in MR, TRUS, and TUUS using a radially-phased IVUS catheter transducer.

5.2.1 Tissue-mimicking Phantom

Multi-modal phantoms were constructed according to a modified recipe from the literature [224]. This agar-based phantom mimicked the appearance and tissue properties of a human prostate in Ultrasound, CT, MR, and PET, and remained stable over a 1-month period. The recipe was modified to exclude $BaSO_4$, [^{18}F] Fluorine, and $^{68}GeCl_4$ since CT and PET properties were not used for the experiments described in this thesis. Barium sulfate increases radiographic attenuation, while $^{68}GeCl_4$ and [^{18}F] Fluorine both exhibit positron (β^+) decay, necessary for PET imaging.

Component	100 cc Prostate	400 cc Pelvis
DI Water	87.65 mL	338.92 mL
Agar	3.64 g	4.68 g
Gelatin	5.7 g	21.92 g
$CuCl_2 \cdot 2\,H_2O$	0.12 g	0.44 g
EDTA	0.34 g	6.6 g
NaCl	0.8 g	3.08 g
37% Formaldehyde	0.25 mL	0.96 mL
Germall-Plus	1.5 g	5.8 g
$25\mu m$ Glass spheres	0 g	17.6 g

Table 5.1: Amounts of raw materials for a 500 cc multi-modal phantom consisting of a 100 cc prostate and 400 cc of pelvic material. The recipe for the prostate aspect of the phantom was modified according to the desired phantom size [224].

A total of three phantoms were created, with different sizes representing the mean and $+1\sigma$ and -1σ prostate volumes of the previously discussed population (Section 4.1). The phantom specifications are outlined in Table 5.1. The variety in phantom sizes allowed for the robustness of TUUS imaging to be tested. Each phantom was created as a result of a 3-step process. The prostate phantom was created using a

50-75 ml beaker, to roughly mimic the prostate shape. A piece of sterile pneumatic tubing with 3 mm outer diameter was inserted into the prostate to simulate the urethra. Finally, the phantom was placed in a 5" × 5" × 2.8" glass container and filled with pelvic phantom material and was cured for 12 hours at room temperature.

5.2.2 Image Acquisition

Transurethral imaging was accomplished using a radially phased catheter transducer (Visions, Volcano Therapeutics) designed for intravascular imaging. Transducer elements operated at $f_c = 9$ MHz with a 2 MHz bandwidth. A companion IVUS imaging system (i5, Volcano Therapeutics) was used to generate acoustic signals. The size of the transducer (8.2 F) minimized the trauma to the phantom during catheter insertion. During imaging, the catheter was slowly withdrawn at a uniform rate to ensure that consecutive slices had roughly uniform slice separation. A DICOM image sequence was then exported using the IVUS system software.

For TRUS imaging, a Hitachi Hi-Vision 5500 Ultrasound system with 7.5 MHz endorectal probe was utilized. This system and transducer is identical to the one used in clinical studies described in Section 3.2.1.

MR imaging of the prostate phantoms was conducted using a similar protocol to the previously discussed clinical study (Section 3.1.1). A 3T Siemens TrioTim scanner was used with two pulse sequences: an axial and coronal T2 turbo spin echo pulse sequence, and a T1 sagittal acquisition. Diffusion and perfusion were not taken due to the use of a static prostate model. Table 5.2 outlines the imaging parameters for all modalities.

Compared to TRUS, the effective resolution given by the TUUS scan is doubled ($120\mu m$ vs. $240\mu m$). The system used exceeded the previous resolution of the rotational system ($300\mu m$).

	Frequency	Voxel size
Magnetic Resonance	–	$0.47 \times 0.47 \times 2.0$ mm
Transrectal Ultrasound	7.5 MHz	$0.24 \times 0.24 \times 0.3$ mm
Transurethral Ultrasound	9 MHz	$0.12 \times 0.12 \times 0.12$ mm

Table 5.2: Parameters of prostate phantom imaging study.

T2 imaging of the phantom produced sub-optimal image quality, likely a result of the modifications to the phantom recipe. However, image quality using the T1 sequence was sufficient for phantom visualization. Figure 5.3 shows the constructed phantom, as well as imaging using all three modalities: MR, TRUS, and TUUS.

5.2.3 3D Reconstruction

There were several challenges in reconstructing the 2D image slices obtained using TUUS into a 3D volume. First, the catheter transducer could rotate during insertion. This was minimized, but could not be avoided due to manual insertion. Second, the "urethra" present in the phantoms were curved, in order to accurate reflect the prostate geometry. Multiple overlapping imaging planes were created as the catheter was withdrawn, complicating the reconstruction. Finally, the 3D volume had to be imported into the the segmentation software described in Section 3.2.1, which required volumes to be imported in an image orientation and format for end-fire TRUS probes. This was necessary to compare TUUS with the current 3D TRUS method. 3D transformation and import into segmentation and registration software was performed using MATLAB 2010b (Mathworks, Natick, MA).

Image sequences from the IVUS system were stored in DICOM format, and were imported into MATLAB (Figure 5.4a). The catheter tract through the phantom 'urethra' was extracted from the MRI, and then interpolated to generate a number of slices (Figure 5.4b). All points along the urethral tract were converted to millimeters

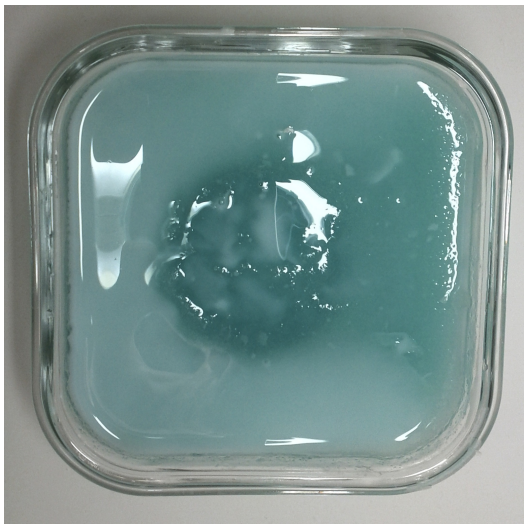

(a) Visual

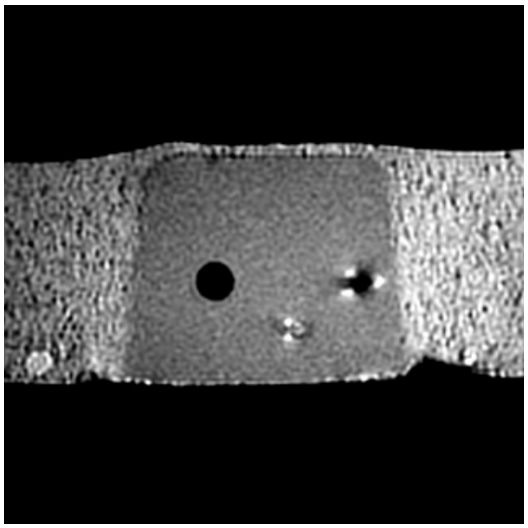

(b) MR

(c) TRUS

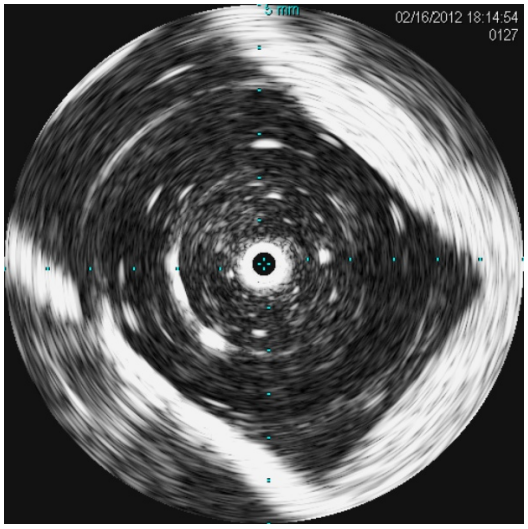

(d) TUUS

Figure 5.3: Multi-modal prostate phantom imaged with (a) camera, (b) MR, (c) TRUS, and (d) TUUS. The phantom, consisting of the prostate (dark aqua) and pelvis (light aqua) is captured in a coronal orientation in (a), while other images are in an axial view. The MR image in (b) shows fiducial markers (large black circles) placed within the prostate (dark grey), which is surrounded by the pelvis (light grainy gray). In (c) TRUS, the imaging probe is located at black semi-circle at the top of the image, while in (d) TUUS, the probe is located at the black circle in the center of the image. The white area around the urethra in TUUS was due to near field effects.

and then to pixels according to the inherent resolution of the TUUS images (0.12 mm). Next, the TUUS frames were automatically rotated to minimize differences between adjacent slices. The number of frames was increased using linear interpolation (Figure 5.4c). This accounted for rotational movement as the catheter was withdrawn.

Next, an affine transformation matrix was constructed for each slice, which consisted of a rotation around the axis defined by the urethra phantom. The axis of rotation was calculated from the cross product between the vector towards the next point on the urethral tract, and the normal vector of the frame. The image was placed on the XZ dimension of a 3D volume, with the normal vector being the +Y axis. The image was replicated twice, so that it was 3 pixels thick, in order to facilitate interpolation.

$$\mathbf{u} = \underbrace{\hat{\mathbf{n}}}_{\text{image normal}} \times \underbrace{\hat{\mathbf{v}}}_{\text{current trajectory}} \tag{5.1}$$

$$\theta = \cos^{-1}\left(\frac{\mathbf{n} \cdot \mathbf{v}}{\|\mathbf{n}\|\|\mathbf{v}\|}\right) \tag{5.2}$$

The affine matrix, constructed according to Equations 5.1–5.3 was used to rotate each image about a vector, resulting from the cross product of the image normal vector and current trajectory.

$$\begin{bmatrix} u_x^2(1-\cos\theta)+\cos\theta & u_x u_y(1-\cos\theta)-u_z\sin\theta & u_x u_z(1-\cos\theta)+u_y\sin\theta \\ u_x u_y(1-\cos\theta)+u_x\sin\theta & u_y^2(1-\cos\theta)+\cos\theta & u_y u_z(1-\cos\theta)+u_x\sin\theta \\ u_x u_z(1-\cos\theta)-\sin\theta & u_y u_z(1-\cos\theta)+u_x\sin\theta & u_z^2(1-\cos\theta)+\cos\theta \end{bmatrix} \tag{5.3}$$

The affine transformation (Figure 5.4d) was applied to the 3D volume containing the frames, and new values were calculated using trilinear interpolation. Both a

nearest neighbor and bilinear interpolation were initially used, but did not provide acceptable quality.

The rotated image slice was placed in the final volume, translated so that the center of the volume was the center of the corresponding point on the urethral tract. At each voxel, a test was applied to check if empty voxels existed at the original or destination. These voxels were then replaced with ones containing data. If both source and destination voxels contained data, then the values were blended through averaging (Figure 5.5a). The shape of the urethra was roughly a simple curve shape, reducing tortuosity, and thus blending of large numbers of co-located slices.

The segmentation and registration software used was the same system utilized in the previous chapter (Section 3.2.1). This ensured a consistent *in vitro* evaluation of MR, TRUS, and TUUS imaging. Data had to be imported as a rotational volume, similar to the 3D TRUS acquisition using end-fire probes. 180 rotational slices were extracted from the original orthogonal volume, one per degree (Figure 5.5b). The center of rotation was selected as the center of the prostate phantom.

The mean computation time for the automated 3D reconstruction algorithm was 514 seconds, using a quad-core PC with 8GB of RAM. This time was measured using 200 TUUS images, each sized at 500x500 pixels, and placed in a final volume of 500x500x500 voxels. The run-time for each image was 2.3 seconds. In order to speed up the computation, interpolation steps were implemented in C++. Calculations for each frame could be performed in parallel and used to further reduce the reconstruction time. Furthermore, merge operations between the source and destination matrix were optimized to take advantage of the (initially) sparse dataset.

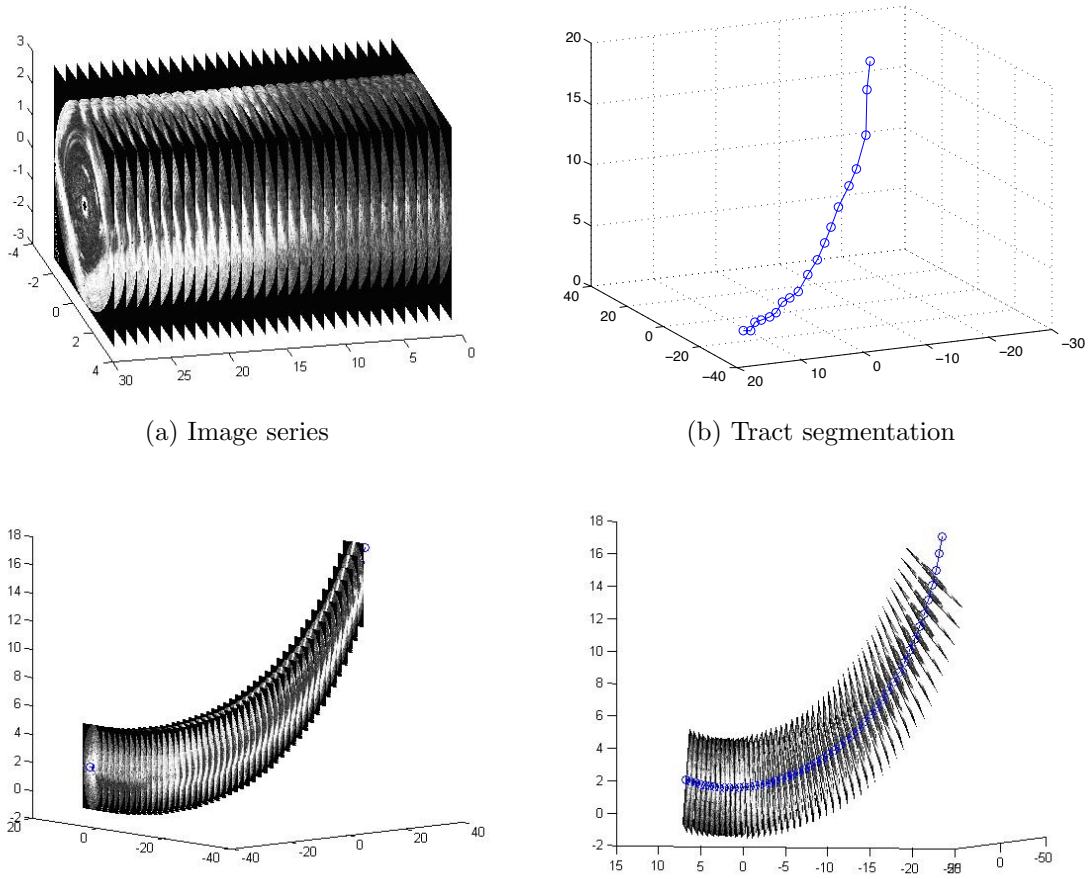

(a) Image series

(b) Tract segmentation

(c) Interpolation

(d) Affine transformation

Figure 5.4: 3D reconstruction of prostate phantom using (a) TUUS 2D slices. Workflow includes (b) segmentation of catheter trajectory on MR slices, (c) interpolation of image slices and segmented tract, and (d) translation and rotation to correct slice orientation along trajectory.

5.3 Comparison with TRUS

Both TRUS and TUUS volumes were imported into the biopsy tracking software. A semi-automatic segmentation, identical to the one performed in Section 3.2.1 was performed on both modalities. We previously noted that prostate volume concordance strongly influences the accuracy of prostate cancer diagnosis using fusion. The fusion process requires a reliable volume estimation. It was previously shown that

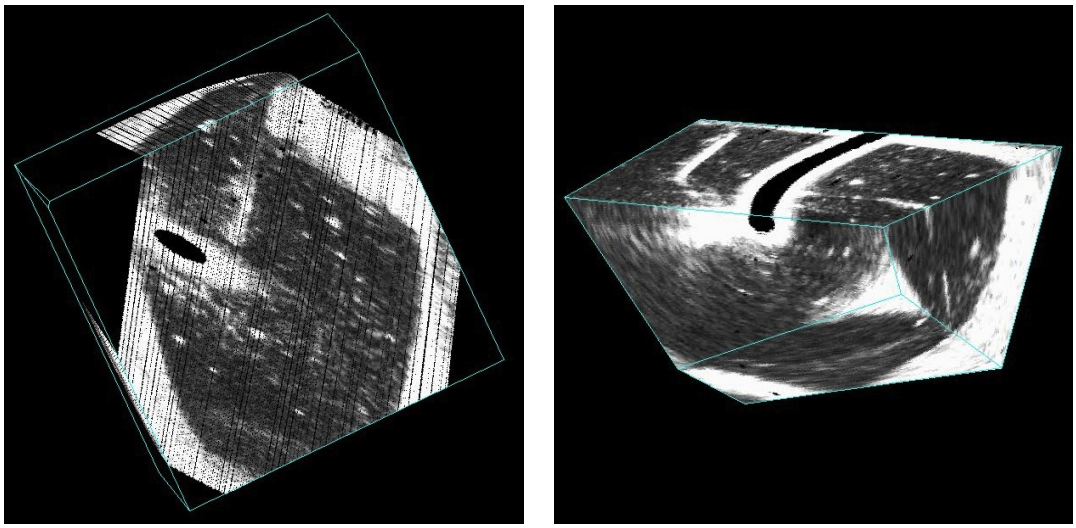

(a) Final linear volume (b) Final rotational volume

Figure 5.5: 3D reconstruction of prostate phantom is finally processed using (e) blending and trilinear interpolation to achieve final volume. TUUS volume is further transformed (f) into 180 rotational slices (1 per degree) for import into segmentation software and comparison with 3D TRUS.

TRUS measurements are generally similar to MR volumes *in vitro*. We performed segmentation on the TUUS volume to qualitative compare the volume accuracy.

The prostate phantom was delineated in an axial and sagittal view on TRUS and TUUS. The phantom shape was similar to a prostate, but contained sharp angles, which affected the segmentation. Actual phantom volume was measured to be 75 cc during fabrication, but was reduced in size approximately 5-10% after solidifying. In TRUS, the phantom was found to have a volume of 77.17 cc, while TUUS found a volume of 65.12 cc. We compared this volume to the MR segmented volume, which was 61.50 cc.

The semi-automatic algorithm utilizes a template of normal prostate shapes to construct the surface mesh. The sharp edges in the phantom appeared to cause the final mesh to be slightly distorted, which could explain the discordance between all three volumes. Furthermore, TRUS images required contact, and slight compression

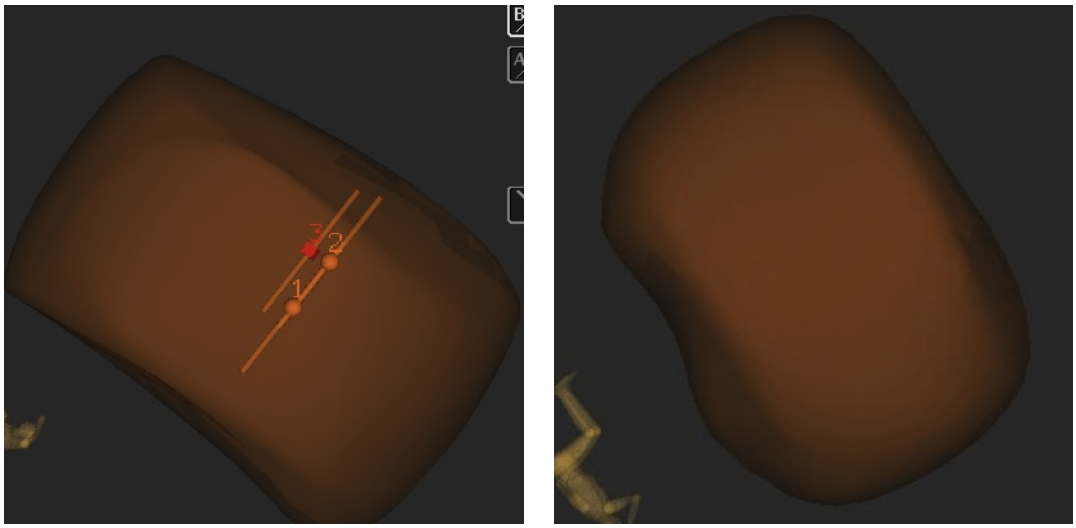

(a) TRUS (b) TUUS

Figure 5.6: 3D reconstruction of phantom volume in (a) TRUS and (b) TUUS. Orange lines in (a) indicate positions of hyperechoic fiducial markers (glass beads), inserted under TRUS guidance. Both prostate volumes in TRUS and TUUS were similar after segmentation and 3D reconstruction. Prostate volumes in TUUS were closer to the MRI in three phantoms.

of the phantom, which affected the shape. However, the rough prostate shape on TRUS and TUUS appear to be similar, which validates the feasibility of the 3D reconstruction method for TUUS visualization.

In order to test registration with MR and the two ultrasound modalities, fiducial markers were placed inside the phantom. Six markers were placed in the prostate phantom, consisting of 3 plastic beads and 3 glass beads. This ensured both hypo- and hyper- echoic fiducial markers could be compared. Figures 5.7, and 5.8 show this comparison.

Fiducial markers appeared as "streaks" in the TRUS images, and were qualitatively better visualized using TUUS imaging. Both imaging modalities appear to suffer from shadowing effects, but TUUS less so. In the sagittal view, the urethral tract is easily identified as a void. On TRUS, the urethral tract was visualized as a

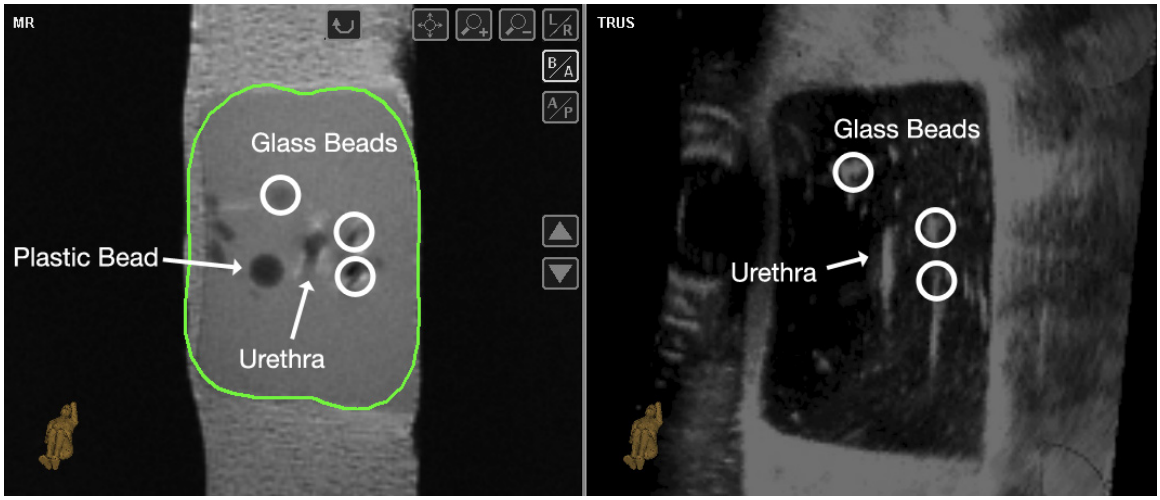

(a) TRUS

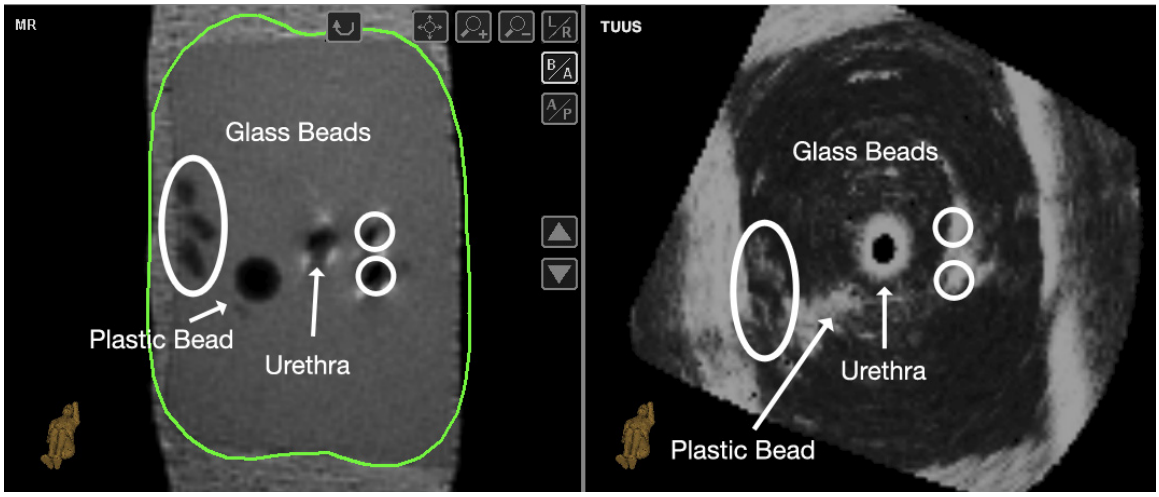

(b) TUUS

Figure 5.7: MR-TUUS fusion comparison in axial view with MR-TRUS fusion. Urethra, hyperechoic fiducials, and phantom defects visualized on both TRUS and TUUS. Fiducials and the urethra in TRUS appear as hyperechoic streaks, while markers in TUUS appear closer to the actual spherical geometry of the fiducial.

hyperechoic distortion. The difficulty in acquiring a 3D image is also highlighted in the sagittal view, as the axis of rotation appears to be off center in Figure 5.9a. The plastic bead fiducials (hypoechoic), one of which can be seen in Figure 5.8, did not appear on either ultrasound modality.

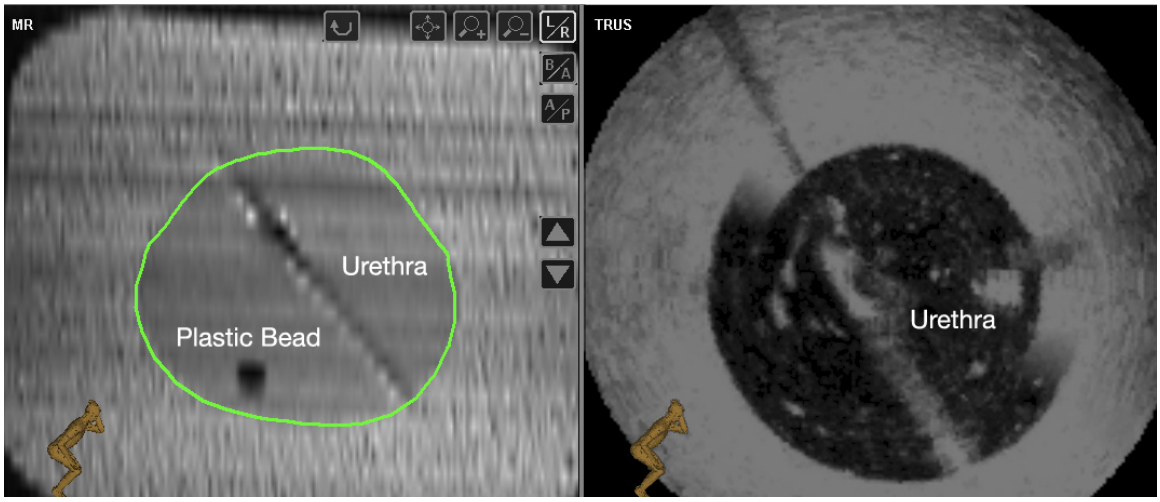

(a) TRUS

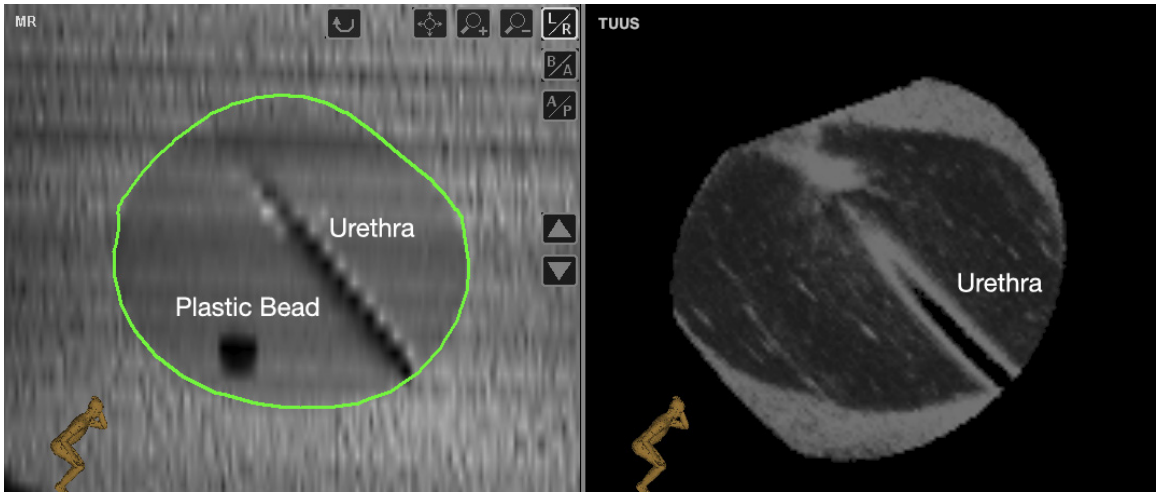

(b) TUUS

Figure 5.8: MR-TUUS fusion comparison in coronal view with MR-TRUS fusion. Urethra is better visualized on TUUS compared to TRUS. Hypoechoic fiducial markers (plastic bead, black circle on MRI) are not visualized on either ultrasound modality.

5.4 Discussion

Previous studies looked at a rotational transducer array which suffered from non-linear distortion (NURD). Rotating drive shafts were also found to be impractical due to the number of electrical connections that must be fed down the shaft of the catheter and

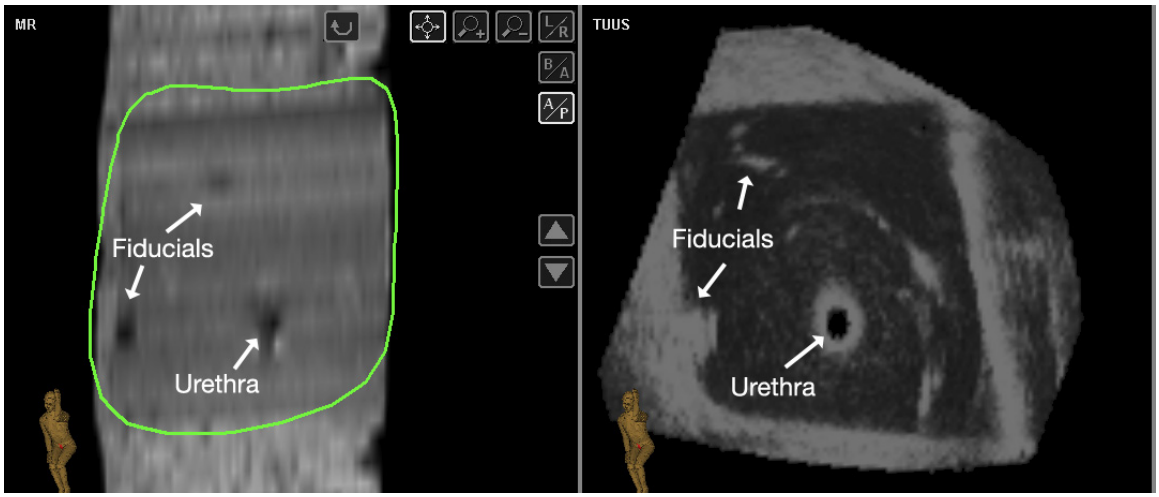

(a) Sagittal

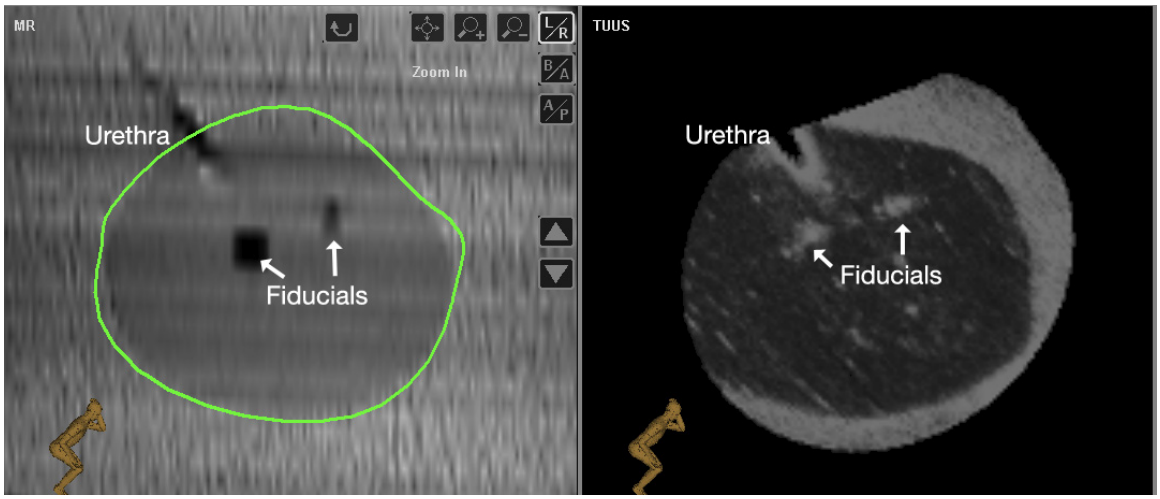

(b) Coronal

Figure 5.9: Additional images of MR-TUUS fusion in sagittal and coronal views. Fiducial visualized clearly and in same locations on both MR and TUUS. Registration was accomplished using TRUS software, indicating feasibility of MR-TUUS fusion.

rotated [207]. Registration studies using TUUS and CT previously used three separate pullback scans (base, middle, and apex) of the prostate, and were independently reconstructed. In this study, a radially-phased 64-element IVUS transducer array and a single pullback scan was used. The prior limitation of this transducer, 3D image reconstruction, was overcome and demonstrated to be comparable to TRUS.

Furthermore, with TUUS we could achieve a higher imaging resolution over TRUS. Moreover, shadowing artifacts appeared reduced. However, the qualitative nature of this data makes the advantage in target registration error unclear. The specific configuration of the phantom could have also influenced imaging results, notably with the presence of large specular reflectors adjacent to the urethra.

In prior studies, specular reflections in US images caused common intensity-based registration schemes to fail. Manual segmentation and registration had to be used to accurate reconstruct the 3D volume. We have successfully demonstrated an automated algorithm to reconstruct the 3D TUUS volume, given an MRI of the urethral tract. MR-TUUS fusion was demonstrated using current registration algorithms optimized for TRUS. Furthermore, volume reconstruction could be performed in seconds if parallel rendering were utilized.

One limitation of this study is that the pullback rate must be kept constant, as was found in prior studies. Mechanical pullback devices exist, but add cost and complexity to the procedure. Another limitation of these studies is the quantitative validation of the 2D to 3D TUUS registration method. It is unknown how the selection of MR fusion method influences image quality, as errors may be introduced with the current method. However, these studies demonstrated that registration was possible, even when using a semi-automatic registration method designed for TRUS imaging. Improved algorithms will only serve to improve TUUS for prostate imaging.

Smaller prostates would benefit from a TUUS based approach, since a high resolution can be achieved, and alignment could be simplified by using the urethral tract. Larger prostates would conversely become more problematic with the current system, since the TUUS array barely captured the entirety of the 75 cc prostate phantom at 9 MHz. As the study in the previous chapter demonstrated, large prostates are a source of difficulty even for TRUS imaging. Modification to the pulse repetition frequency,

and center frequency would be necessary in larger models. A system which allows for dynamic frequency adjustment, assuming the transducer has the necessary bandwidth, would allow for more robust imaging of the prostate. Other limitations may be overcome through the use of a natively 3D imaging method, as 3D construction would be performed in situ. These improvements together would potenially enable real-time 3D fusion imaging of the prostate, and thus may increase the diagnostic accuracy of targeted biopsy over existing 2D methods.

Chapter 6

An Improved Prostate Imaging System

This chapter describes a prostate imaging system that aims to address the limitations of the 2D IVUS arrays used in the previous section. An ideal prostate imaging system was described to be capable of real-time 3D imaging, necessary for accurate intra-procedure registration and lesion targeting. The depth of penetration and field of view was found to be insufficient for very large prostates, necessitating dynamic adjustment of acoustic signaling parameters.

There are several other considerations in developing such a system; namely, the ability to utilize newer imaging techniques while being compatible with current pulse-echo based imaging. To this end, a versatile imaging system was developed, capable of driving a multitude of transducers, and able to utilize frequency-based signaling techniques in addition to pulse-echo transmission.

This system, the Reconfigurable Diagnostic Imaging Platform (RDIP), included a cylindrical transducer array, suitable for mounting at the end of a transurethral catheter, and electronics to handle signal generation and processing. Eight independent transmission and reception pathways, or channels, were implemented, each consisting of an arbitrary waveform generator, a power amplifier, an analog receiver, and embedded control logic. A field programmable gate array (FPGA was used to control each channel and communicate with a PC.

6.1 Catheter-based Transducer Array

A transurethral catheter-based transducer array was designed with piezoelectric elements spaced circumferentially around an 18F (6 mm) catheter. Initial design specifications based on the previous studies required a center frequency of 9-12 MHz to improve the resolution over TRUS. An impedance of 50Ω was necessary to minimize losses between imaging electronics and transducer array. Each element was required to be balanced with respect to frequency and impedance, in order to be able to perform multi-static imaging. A 6dB Bandwidth of 2 MHz was needed in order to use frequency-based signal processing techniques and to vary the depth of penetration. Figure 6.1 shows an initial array after fabrication.

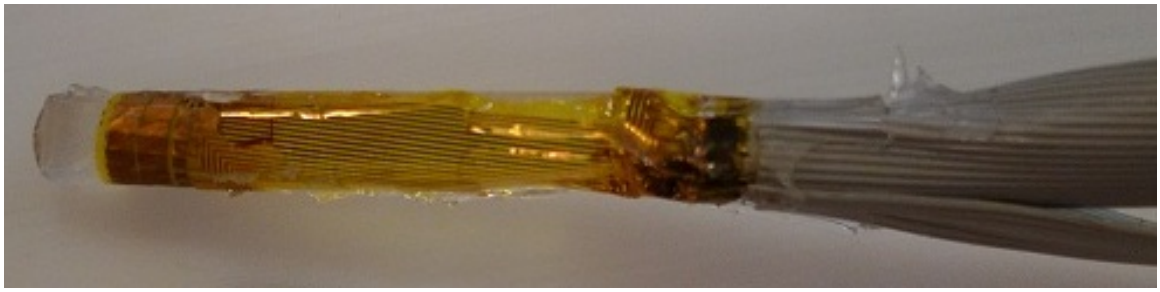

Figure 6.1: Transurethral ultrasound transducer array developed at UCLA using microelectronics fabrication methods. Transducer consists of 32 elements, arranged in a 2 x 16 format. The 2D array configuration enabled multi-planar (3D) image capture.

6.1.1 Fabrication Process

Fabrication of the transurethral ultrasound array was performed by collaborators at the Institute of Micro and Sensor Systems (IMOS), University of Magdeburg (Magdeburg, Germany). The cylindrical 2D transducer array was constructed similarly to a previously described micro fabrication process [225].

A flexible polyimide substrate was used to allow for bending and wrapping in a

cylindrical shape. For this initial prototype a backing layer was not used. Copper leads were patterned on the polyimide substrate. Lead zirconate titanate (PZT) plates with gold electrodes were soldered to the copper layer, which were then diced in single elements forming the array. The entire array was then wire-bonded, wrapped, and filled with polydimethylsiloxane (PDMS). The array elements were patterned in a row-column arrangement, to simplify interconnections and to allow for scalability with multiplexers. Row elements were connected via ground traces on the outer layer of the transducer, and columnar elements were connected via wire bonding. Each row and column trace were integrated into a row of solder pads (pitch of 1.1mm). [226] Solder pads were patterned for each row and column, and were wrapped independent of the array elements.

The initial transducer array contained 2 rows of 16 elements with a frequency of operation at 18 MHz. This high initial frequency was chosen to test the range of the system electronics. An optimal design for the prostate requires a 9-12 MHz array. After cylindrical wrapping, a 6 mm diameter was achieved, representing an 18 F catheter.

6.1.2 Interconnect and Packaging

A standard ribbon cable (40-pin, 0.625mm pitch, 30 AWG) was used to connect the transducer to the imaging system. The cable contained conductors that were soldered onto each of the 18 leads patterned on the transducer array. The pitch of the solder pads were designed to match the pitch of the ribbon cable. Every other conductor was soldered to the transducer, with the remainder of the wires soldered to ground, such that every signal wire had adjacent ground wires to ensure minimal cross-talk. The cable terminated with a standard 64-pin molex connector for compatibility with the system electronics.

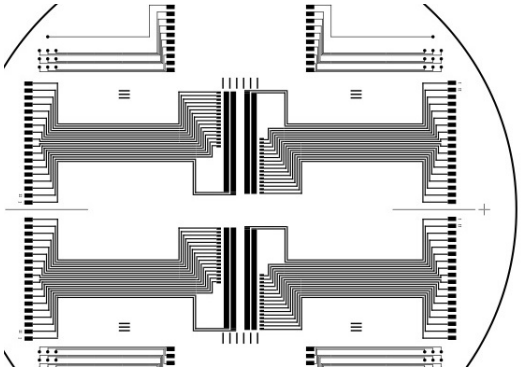

(a) Mask

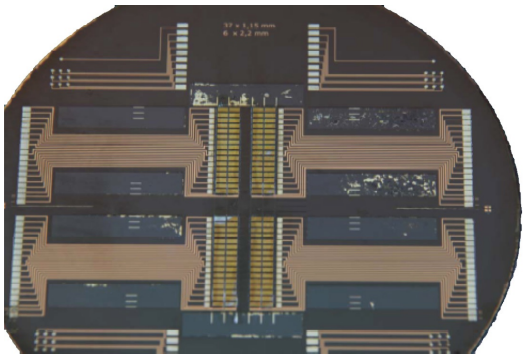

(b) Wafer

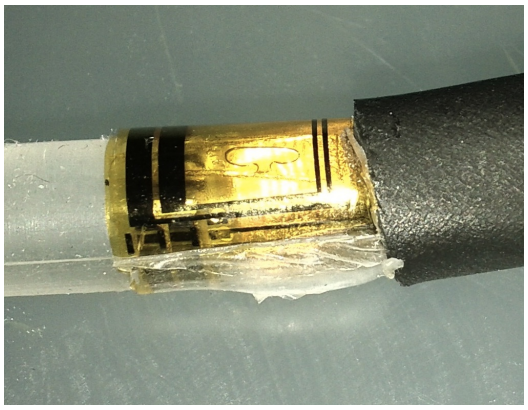

(c) Wire bonds

(d) Wrapped array

Figure 6.2: Fabrication process for catheter-based prostate imaging array. Transducer was designed using microelectronics (MEMS) fabrication methods, and involved creating a mask for (a) photolithography, placing piezoelectric elements and dicing them into an array on the (b) wafer, which ensured that elements in the same row were electrically connected. Elements in the same column were connected using (c) wire bonds, and the array was (d) cylindrically wrapped and filled using PDMS.

The interconnects were encased in PDMS to protect the assembly from tearing and shearing forces. The entire cabling system was then wrapped circumferentially and encased with a flexible polymer (RTV-30) using an 18F catheter mold. Table 6.3 describes the fabrication parameters and characterization results for the TUUS transducer array.

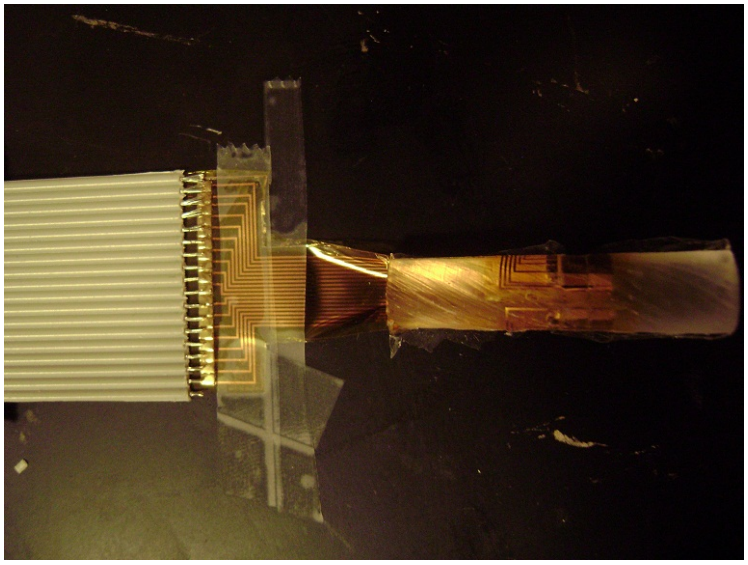

Figure 6.3: Interconnect between transducer elements and system electronics, consisting of a standard 1.27 mm pitch ribbon cable. Every other element was grounded to minimize noise and ensure signal integrity over the cable length (3 ft).

6.2 Image Reconstruction

Synthetic transmit aperture (STA) is a tomographic image reconstruction algorithm based on transmit-receive transducer element pairs. This technique was previously explored for use with an inward-looking flexible transducer array [227–229].

In STA, range profiles from pairs of transducer elements are analyzed for echoes. Locations corresponding to points on the range profiles are ambiguous, as they could be located anywhere on an ellipse defined by the transducer pair (see Figure 6.4). Thus, the entire ellipse is illuminated on the reconstructed image. The final image is produced by iterating through all points on the range profile and all array combinations. Areas on the image that contain many intersections, or hot spots, have a high statistical likelihood of being acoustic reflectors. Additional post-processing can be utilized to further enhance the image quality.

STA is potentially advantageous in 3D ultrasound imaging because it requires sim-

pler processing. This would also improve imaging over beamforming techniques since transducer elements in an outward-looking circumferentially array, such as TUUS, cannot be phased with more than a few elements.

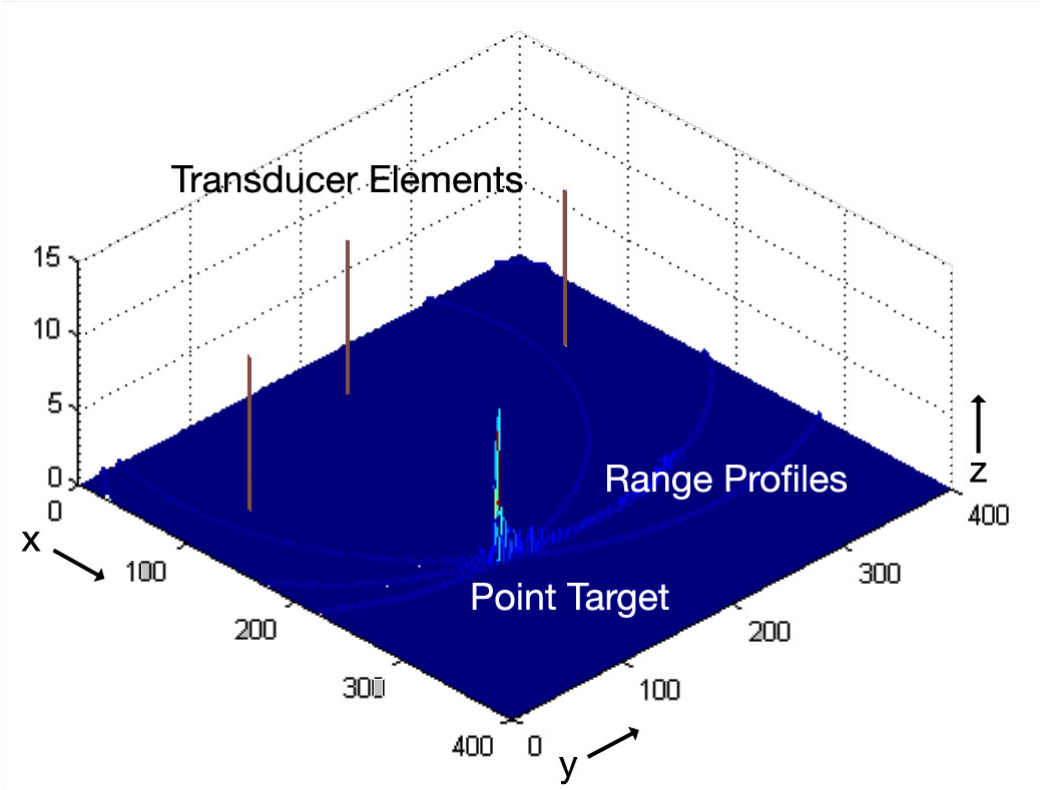

Figure 6.4: Image reconstruction using synthetic transmit aperture (STA). Three transducer elements are represented by vertical red lines, and the point target is represented by the intersection of the three arcs. STA uses pairs of transducer elements as points in an ellipse defined by the roundtrip acoustic transmission time between both elements. The ellipses indicate all probable points where a reflection occurred, and the intersection of ellipses indicate the location of a reflector, with high probability.

6.3 System Electronics

Theory of Operation

The transmitter is comprised of a high-speed digital-to-analog (D/A) converter connected via universal serial bus (USB) to a laptop. This laptop connection allows for arbitrary signal generation by first designing the waveform on the laptop and then downloading it to the transmitter where it is converted to an analog waveform.

The analog signal is then routed to the desired firing element through a 16-channel multiplexer (MUX) and Transmit/Receive (T/R) switch controlled by the laptop. To transmit and receive through a pair of transducer elements, first the T/R switch is put into the transmit position and the MUX is configured to connect to the desired transmitting element. After the transmit waveform is applied to the element, the T/R switch is then put into the receive position and the MUX is configured to connect to the receive element. These steps help protect the sensitive receive electronics.

The received waveform is then down-converted from the carrier frequency (same as the center frequency of operation) to baseband through a super-heterodyne down-converter. The receiver is comprised of two mixers and low pass filters (i.e. classical I-Q demodulator architecture) so as to extract the in-phase and quadrature phase baseband signals. These signals are then digitized and uploaded to a laptop via USB.

A detailed block diagram of this system, the Reconfigurable Diagnostic Imaging Platform (RDIP), can be seen in Figure 6.5.

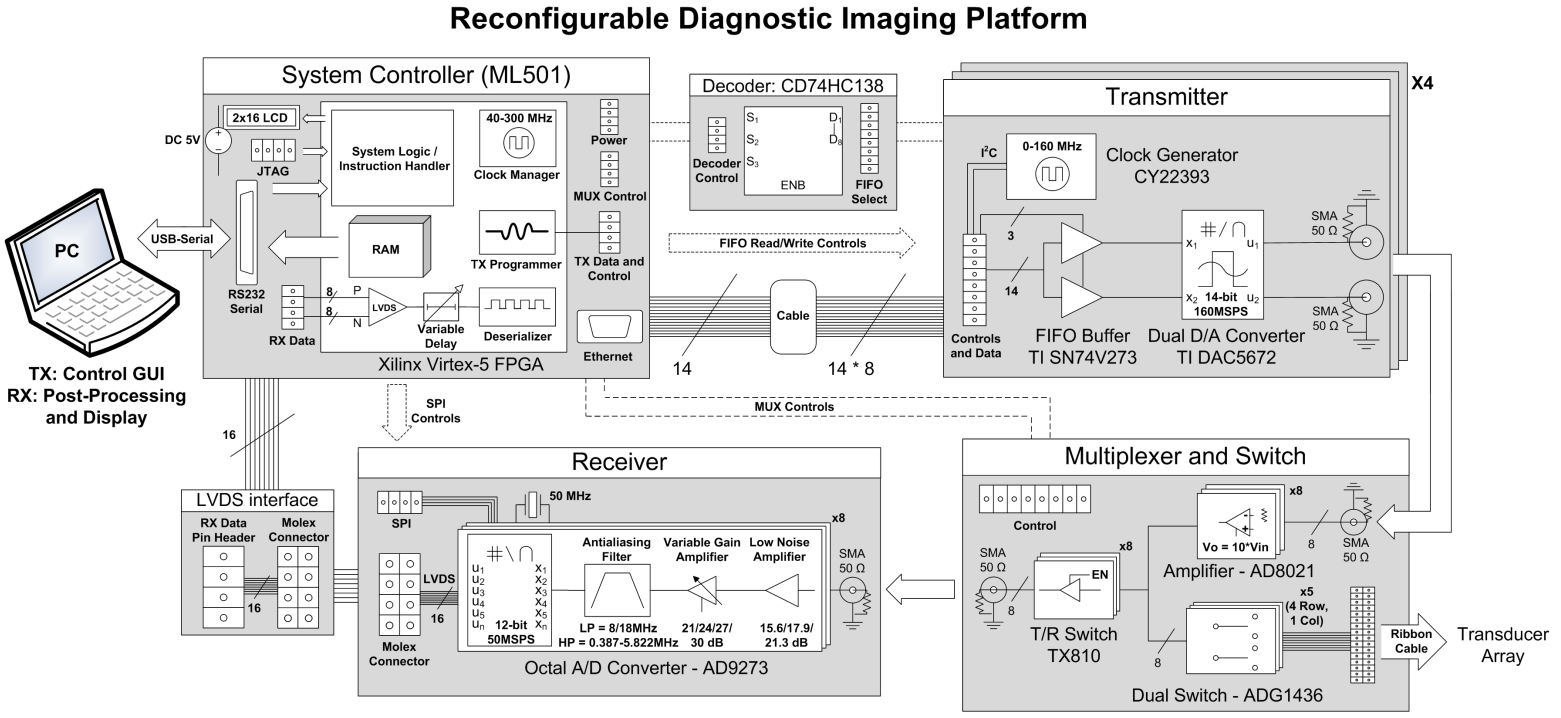

Figure 6.5: Block diagram for Reconfigurable Diagnostic Imaging Platform (RDIP), which consists of an eight-channel ultrasound transmitter, eight-channel receiver and FPGA controller.

6.3.1 Hardware Description

The system was designed using Eagle EE software, and components were subsequently fabricated using an online vendor (Sunstone Circuits). All system components were integrated into a mini-ATX computer case, allowing the system to be portable and low-power.

Transmitter

The arbitrary waveform generator enabled precisely designed signaling methods to be easily implemented in system hardware. The transmit pattern is programmed on the FPGA using a laptop over a serial connection. The resulting samples are then downloaded into the onboard volatile memory buffer.

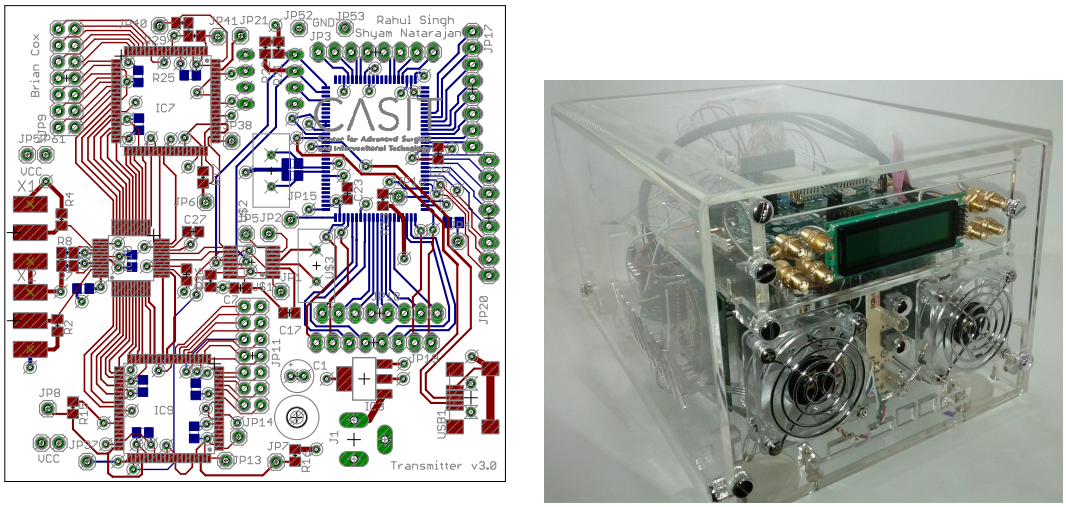

(a) PCB (b) Use in System

Figure 6.6: (a) Printed circuit board (PCB) of two-channel arbitrary waveform generator, 4 of which were used in the (b) ultrasound system. Imaging system contains 4 identical boards, resulting in eight channels of independently programmable waveforms operating in either synchronous or asynchronous mode.

Once the transmitter is activated, the waveform is sent from the microcontroller to

first-in-first-out (FIFO) memory buffers. The data in the FIFO buffers (TI sn74v273) could then be clocked out at a very high rate to the D/A converters, where the analog signal is then transmitted into the transducers. The use of FIFO buffers allows the waveform to be constantly retransmitted at full speed (166 MHz) without any communication with the PC, ensuring the stable operation of the system. Data output from the TI DAC5672A dual channel 14-bit D/A converters is converted from differential to single-ended mode, allowing the use of common 50Ω RF cables in the rest of the electronics.

A Cypress CY22393 programmable clock generator handled digital timing on each board, which was managed by the FPGA using an I^2C serial connection. Each clock chip was driven by a 10 MHz crystal oscillator, and an FPGA external clock. The clock source could be dynamically selected, allowing each transmitter to receive a coherent waveform or operate in an asynchronous fashion. This design, while more complicated, offered greater flexibility in frequency selection. The former setting is necessary for phased array operation, and in the latter case each channel could transmit a completely independent waveform pattern, center frequency, and pulse repetition frequency (PRF).

$3.3V$ power from each dual-channel transmitter was supplied by stable voltage regulators on the FPGA evaluation board. Each transmitter drew up to 200 mA in power during active use. The use of off-the-shelf components and open-source software allowed the system to be cheaply built and modified, which was important for initial prototyping and allowed for the determination of initial parameters. The specifications of the current iteration of the system are listed Table 6.1.

Conditions: $f = 20$ MHz

Power Supply		$V_{dd} = 3.3$V (FPGA-powered)
Output Voltage		367 mV
SNR	Actual	70 dB
	Nominal	86 dB
Power Spectral Density		80.1 dB $\frac{\text{uV}}{\text{Hz}}$
Effective Number of Bits	@75 dB	12
	@70 dB	11.67
Line Width		100 Hz

Table 6.1: Technical specifications of the arbitrary waveform generator. Actual signal-to-noise ratio (SNR) achieved by the system was close to the theoretical maximum based on system components, indicating a low contribution to overall system noise. A 100 Hz line width, or frequency resolution, was achieved at 20 MHz, and measured using a spectrum analyzer.

Multiplexer

Between the transceiver and transducer, a multiplexer and signal conditioning board was used to address and isolate each channel from the array. The board contains an eight channel single pole double throw (SPDT) switch, which isolates the receiver from high power transmissions. Each transmitter channel contains a buffered amplifier with 10x gain, a reconstruction filter (low-pass filter) with a 3 dB cutoff frequency of 20 MHz, and a 1:4 multiplexer. The multiplexer enables addressing for up to 32 transducer elements.

In order to facilitate the architecture of the TUUS array, row-column addressing was used. In order to activate a particular element (in the m^{th} column and the n^{th} row) a differential signal was applied to the m^{th} column interconnect and the n^{th} row interconnect. Using this method of addressing, each element in the array was uniquely addressable and able to be independently fired in turn. This technique maximized the number of array elements that could be excited with a minimum number of electrical

interconnects. The fewer cables required between the array and system reduced the catheter diameter.

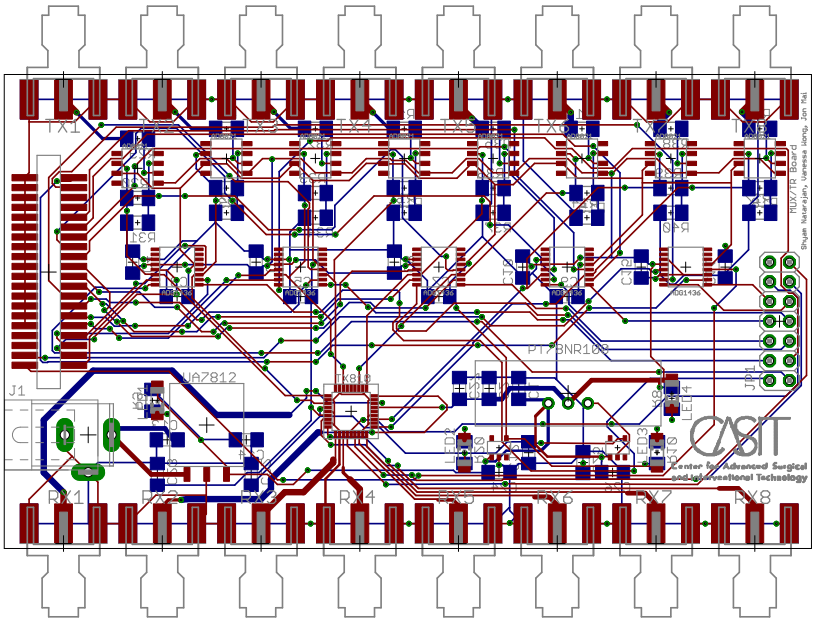

Figure 6.7: PCB layout of multiplexer and signal conditioning board. Board contains 8 independent transmit and receive channels, with capability to address up to 32 transducer elements. Each channel consists of a T/R switch, amplifier, and low-pass reconstruction filter to remove discontinuities in Tx waveforms.

The column is grounded (normally an open circuit), and the acoustic signal is transmitted across the row causing the transducer element at the row, column pair to be selected and transmit the desired waveform. Leakage current caused by transmission of adjacent elements is minimized due to -55dB isolation between each conductor. The leads of the micromachined array were physically connected to the multiplexer with a standard ribbon cable cable, containing 40 conductors. Every other conductor was grounded to reduce noise in transmitted signals.

Receiver

Receiver electronics were necessary to properly decode the information sensed at the transducer. A previous iteration of the system utilized an analog superheterodyne receiver, a low-noise amplifier (LNA), a band-pass filter (BPF), a 90° splitter, dual channel mixers, dual channel low pass filters (LPF), and dual analog-to-digital converters (ADC). The improved system described in this thesis was designed for acoustics in the $1 - 12$ MHz range. This frequency enabled filtering to occur in the digital domain. Thus, an integrated ultrasound receiver was used, containing an octal LNA, variable gain amplifier (VGA), anti-aliasing filter (AAF), ADC, and crosspoint switch (AD9273, Analog Devices). All channel inputs had identical path lengths in order to balance phase. FPGA Interfacing was performed using low-voltage differential signaling (LVDS), operating from 400–600 Mb/s in 8- and 12-bit mode, respectively. A serial interface with the SPI protocol was used to modify the timing and gain settings.

6.3.2 Software Description

Software was implemented on the Virtex-5 FPGA (ML501, Xilinx) in Verilog. The modular nature of hardware descriptor languages (HDL) and FPGA, allowed for a great amount of versatility in the system. The software structure of the FPGA code is outlined in Figure 6.8. PC control was implemented in C++ using a serial standard (RS-232), which was sufficient for eight-channel testing. Future work to expand this to a faster interface, such as Ethernet, is necessary in order for system performance to scale with the number of transducer elements.

The main software blocks included data processing, signal transmission, clock management, system control, and serial PC interfacing. An instruction set was implemented in the FPGA, such that all high- and low-level functions could be called from a connected laptop. Pulse parameters, receiver processing, and control logic

could be modified, allowing for dynamic variation of the transmitted waveforms. This enabled the rapid implementation of signaling techniques, as well as receiver configuration and processing. A custom software program, written in C++, allowed for user control of RDIP. When data was captured and transferred to the laptop, image reconstruction was performed using MATLAB. This software was chosen for its simplicity and modularity, a recurring theme in the system.

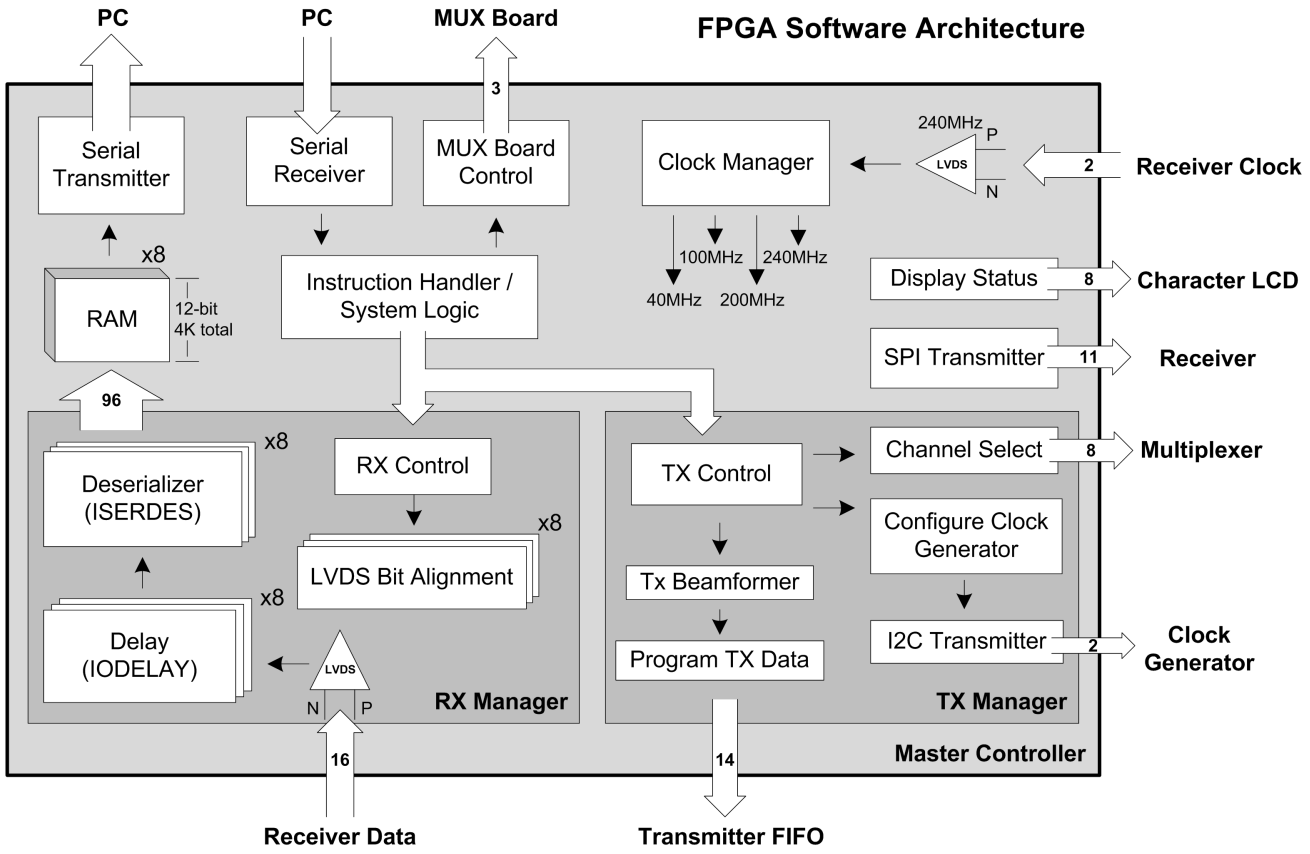

Figure 6.8: Block diagram for FPGA main module, part of the Reconfigurable Diagnostic Imaging Platform (RDIP) system. Each box contains a unique logic module, which allows this software to be scalable up to 16 independent channels. A greater number of channels would require multiple FPGAs.

6.4 System Validation

In order to validate the operation of the RDIP system for use in transurethral ultrasound, each component of the imaging pathway was characterized in isolation. Once correct operation of the entire system together was verified, we performed imaging experiments on a standardized phantom. Following validation, we describe the use of the system with a multi-column catheter-based transducer array.

6.4.1 Measurement Setup

A commercially available Acoustic Measurement System (AMS, Sonora Medical Systems, Glendale AZ), was used to measure the acoustic intensity values originating from the transducer under test. This system allowed for consistent measurements to be acquired across different transducers, as well as precise mechanical rotation and translation of the transmitting element or array. The receiver employed a wide-band PVDF hydrophone (Sonora Model 804) which had a flat acoustic response up to 20 MHz.

Measurements related to frequency response and power were taken using a HP 3577B vector network analyzer, which measured S-parameters on two ports. The system is capable of sweeping from 5 kHz to 200 MHz, and allowed for reflectance and transmission measurements to be taken with 0.1 dB resolution and 0.001 Hz frequency resolution. The output of this system was captured by a laptop running MATLAB, in which raw S-parameter and frequency-power data were processed. FPGA outputs and other digital signals were validated using an HP1664A Logic Analyzer. This machine allowed up to 32 discrete digital signals to be sampled at 250 MHz.

6.4.2 Transceiver characterization

First, the transmitter output was verified via oscilloscope, to ensure a concordance between configured parameters and the transmitted waveforms. Next, the transducer was connected directly into the receiver to test the entire signal path. Attenuators were inserted into the signal pathway to prevent damage to the receiver. Receiver data was captured via PC connection and the resulting waveform, a 10-cycle tone burst at 8 MHz, is shown in Figure 6.9.

Once single channel operation was verified, each channel was compared to one another. Balancing of the receiver was necessary to ensure that data from each channel was valid when the system was used for imaging. Each input was fed a sinusoid pulse and the resulting data was balanced with respect to input phase, and frequency, and noise level.

Once the correct operation of both receiver and transmitter channels were ensured, we conducted *in vitro* experimentation to verify the range accuracy and imaging capability.

6.4.3 In-vitro testing

The imaging ability of the system electronics was first tested using a commercial Acuson L7 8MHz transducer. The isolated system component was attached to eight elements in the center of the array.

The transducer elements were first characterized using a Vector Network Analyzer. Plots of the normalized reflectance can be seen in Figure 6.10. A single element was excited by the system, and the acoustic response was measured using the Sonora test system. The resulting response was compared with the transmission using a commercial ultrasound system (Acuson 128 X/P, Acuson). Table 6.2 describes the

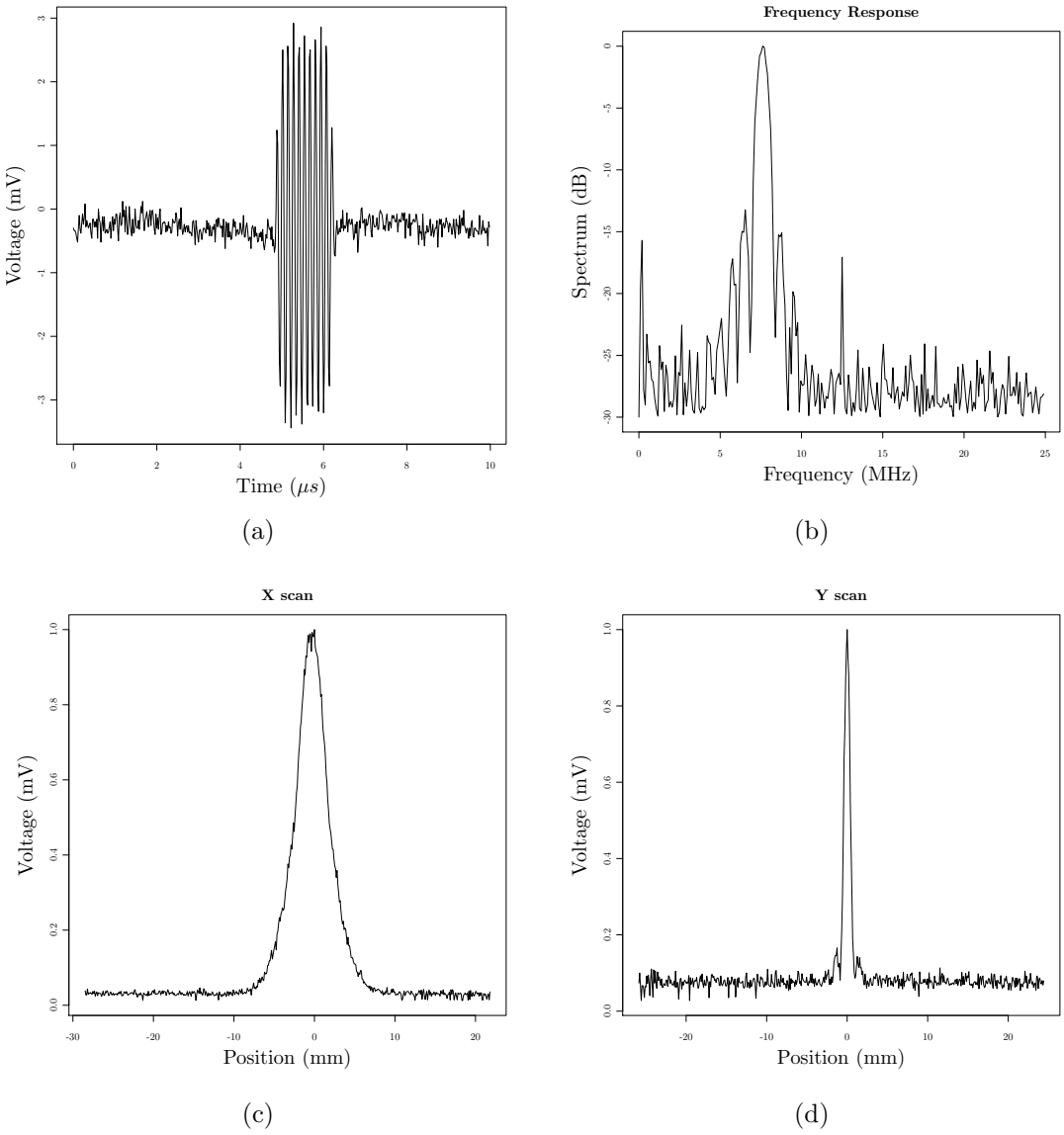

Figure 6.9: Transceiver characterization, including (a) time- and (b) frequency domain representation of acoustic pulse, and (c,d) cross axis scan of single element. The element beam pattern, seen by the cross axis scan, had minimal side lobes, which ensured a high degree of certainty in beam location in subsequent experiments utilizing this transducer.

measured parameters.

The acoustic intensity from the RDIP system was measured to be 0.08 $\frac{W}{cm^2}$ for a

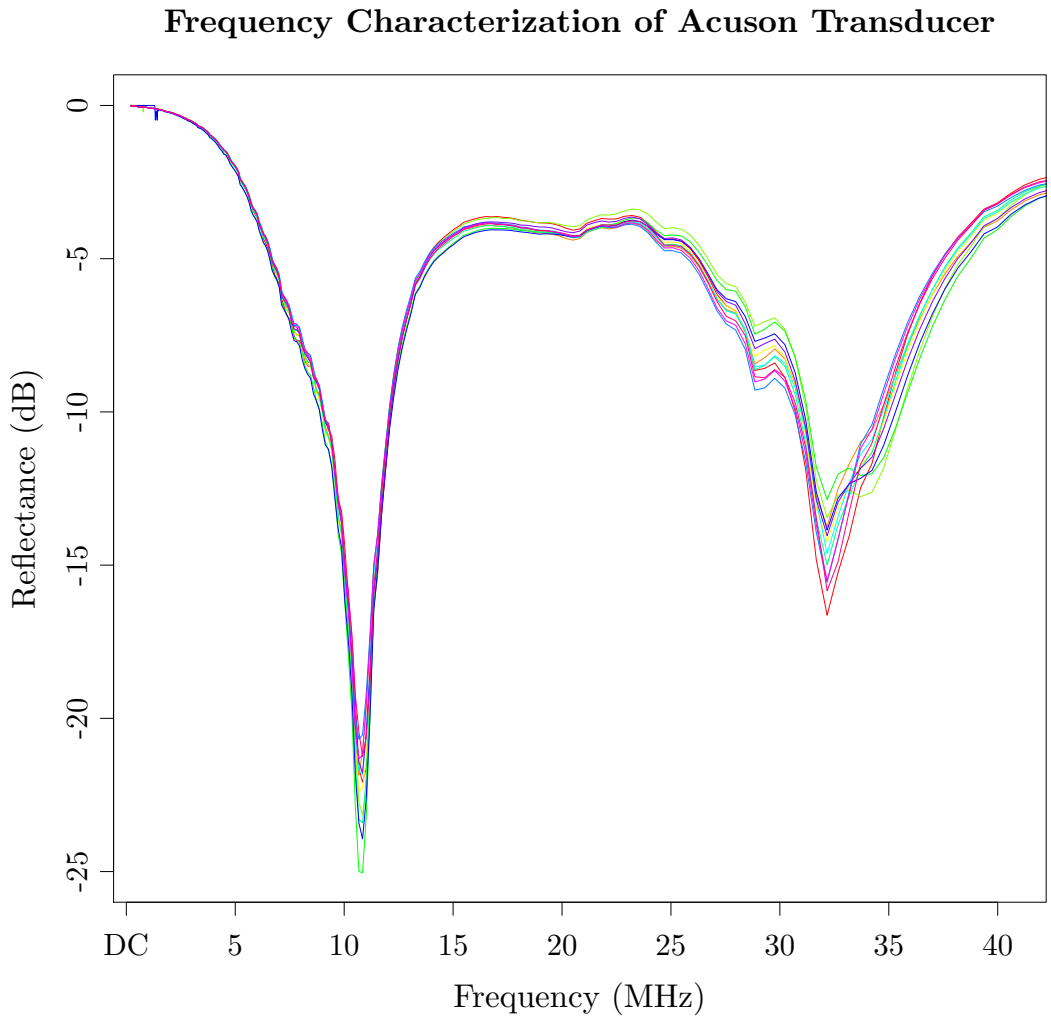

Figure 6.10: Characterization of transducer array used in setup. An L7 8MHz Acuson transducer was used for subsequent testing. Each element was plotted by frequency and reflectance back to the transmitter. Elements are well matched near 10 MHz (low reflectance indicating acoustic transmission), despite the use and compatibility with a 7-8 MHz Acuson system.

single element. In subsequent ranging and imaging tests, comparison of intensities with the Acuson system gave us insight into the theoretical performance of the RDIP system in imaging with dense transducer arrays.

	Acuson	**RDIP**
Center Freq (MHz)	6.914	7.614
Pulse Length (μs)	6.914	7.614
-3dB Bandwidth (MHz)	4.199	0.653
$I_{\text{spta}}(\frac{W}{cm^2})$	66.88	0.08

Table 6.2: Comparison of imaging system with commercial ultrasound scanner (Acuson 128X/P, Acuson). Pulse parameters in Acuson and RDIP for ranging and imaging studies are used to demonstrate low-power operation of RDIP.

Ranging

After confirming the correct power levels and waveform shape, ranging experiments off a calibration phantom were performed. This metal phantom was machined to have 10 targets every 5 mm from 0-100 mm. A single element was driven by a 9 MHz, 1μs pulse and an adjacent receiving transducer element was used as the receiver. The range accuracy off the phantom as a function of depth was recorded (Figure 6.11) in this bistatic configuration. For this test, a range accuracy of 0.92% was found on average for depths 10-45 mm. One explanation for the relatively poor range accuracy is that the test setup was not calibrated properly. This system was also testing using a frequency-based signaling method, which reduced the peak acoustic power [228].

Imaging

In order to test the imaging capability of the RDIP system, a staircase phantom with a 5×5 mm step size was used. The Acuson transducer array was linearly scanned across the surface with a horizontal step size of 250μm, mimicking the pitch from the fabricated TUUS transducer array. The resulting image of the phantom can be seen in Figure 6.12. The signal-to-ratio was in the image was measured to be 18.01 dB at maximum and 15.39 dB on average.

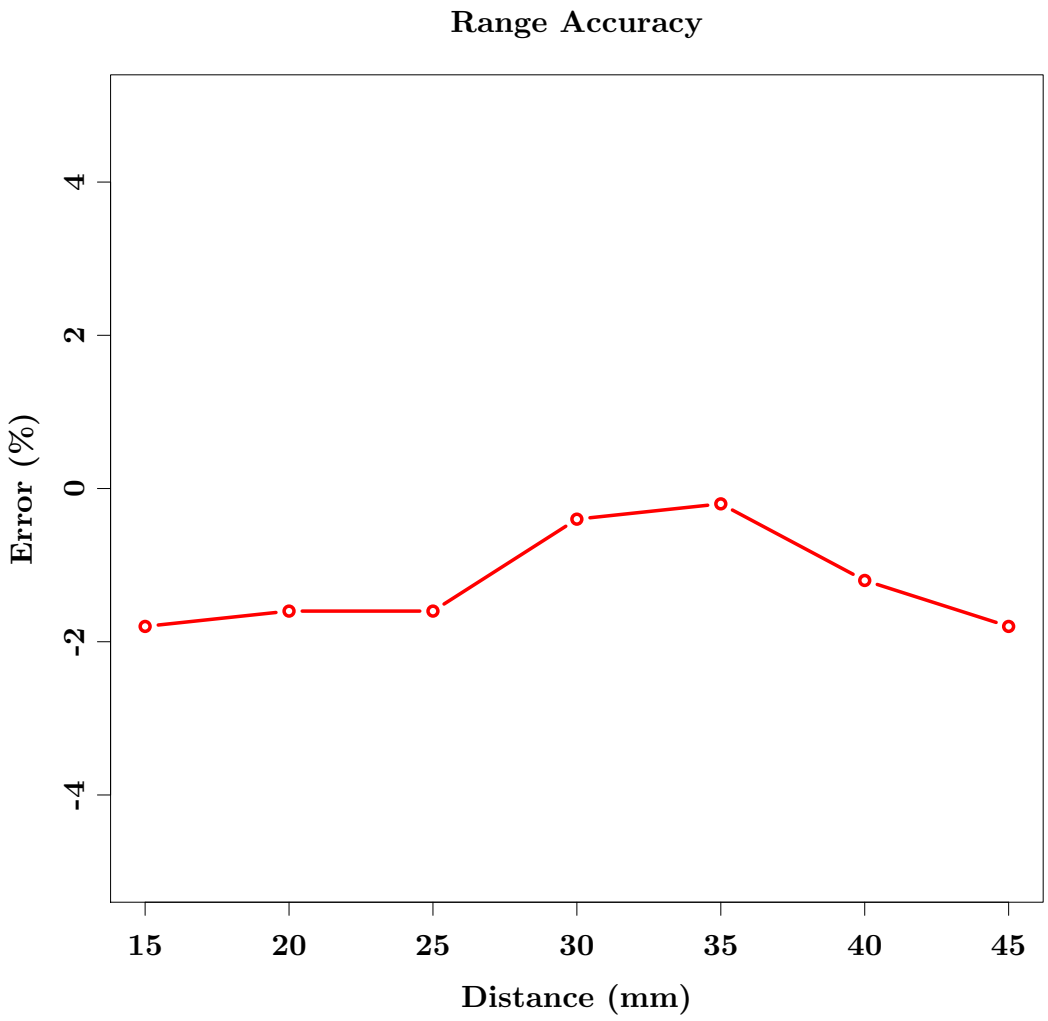

Figure 6.11: Range accuracy of imaging system. Data was taken at 9 MHz, to match the frequency used in the TUUS imaging study in Section 5.2. Accuracy was 0.92% on average.

This test demonstrated feasibility and accuracy of imaging using this system. Once the system electronics were fully tested and characterized, we integrated the catheter-based transducer array.

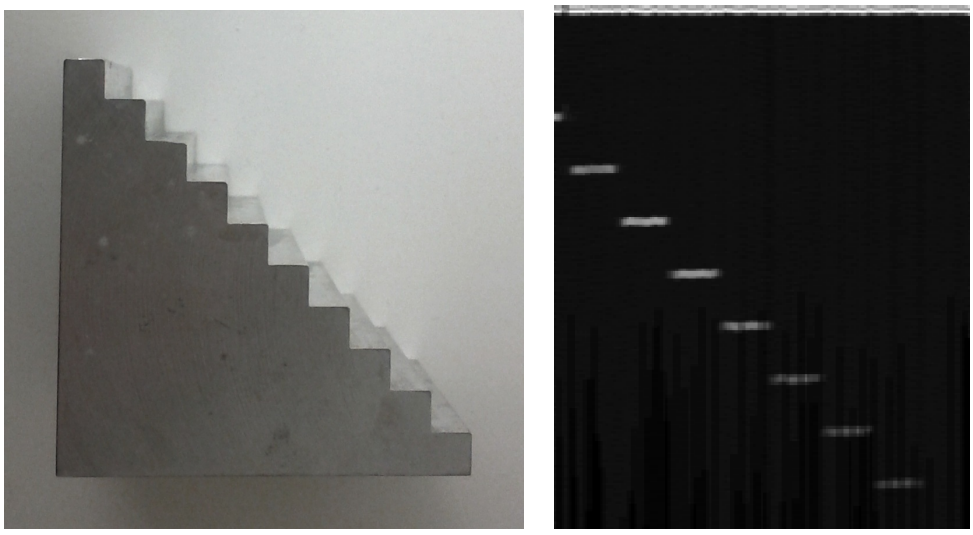

(a) (b)

Figure 6.12: (a) Staircase phantom and (b) resulting image taken with imaging system (RDIP) in a water medium. The Acuson L7 transducer was positioned above the phantom, facing down such that the white lines in (b) represented specular reflections from 'stairs,' and the bright white line at the top of the image represented the initial reflection from the transducer face.

6.4.4 TUUS Array Verification

An initial prototype of the catheter-based transducer array was completed, using the MEMS-based process as described earlier (Figure 6.2), consisting of 32 elements in a 2×16 row-column configuration In order to show feasibility of prostate imaging using this system, the catheter-based transducer array had to be validated. Characterization tests on the transducer array were performed. During the fabrication process, there was a risk of de-poling the piezo electric elements following placement on the flexible substrate. In order to verify the fabrication process and the correct operation of the transducer device, we measured the resonances of each element using a VNA. Table 6.3 shows the characterization information for the TUUS transducer array.

Initial system characterization showed a majority of the elements working after

Elements	22
Center Frequency	18.71 MHz
Impedance	65Ω
Peak Magnitude	-1.6 dB
Full Width Half Max	13.76 MHz

Table 6.3: Characterization of polyimide-based TUUS transducer array. Metric of interest is listed in left column, with value in the right column. Initial array had double the frequency than needed, and a slightly higher impedance, which reduced the efficiency of signal transmission. Array characteristics did not match initial specifications which possibly meant that the transducer elements were de-poled during fabrication.

wirebonding and cabling. Piezoelectric elements had a resonant center frequency of approximately 18 MHz, balanced across 22/32 channels. Impedance was measured to be 65Ω on average, higher than specifications. This frequency was much higher than the ideal TUUS imaging frequency, but served to validate the basic feasibility of the array fabrication process. Furthermore, the broad bandwidth, and low peak magnitude indicated that the PZT needed to be re-poled. Ten elements were not functioning, presumingly due to de-poling of the PZT element during processing. A second array containing larger elements was fabricated and again characterized with the Vector Network Analyzer. Resonant frequency, impedance, and 6dB bandwidth were again measured, shown in Figure 6.13.

This array had only three functioning elements out of 32, but all three met design specifications with a resonant frequency from 10-11 MHz, no imaginary component in impedance measurements, and 6 dB bandwidth of nearly 2 MHz. Pulse-echo ranging data was successfully obtained using this transducer and the system previously described. Transmitted waveforms were at 18 MHz, and then processed. The resulting captured waveforms are shown in Figure 6.14.

With this experiment, valid operation of the the entire system was shown. The

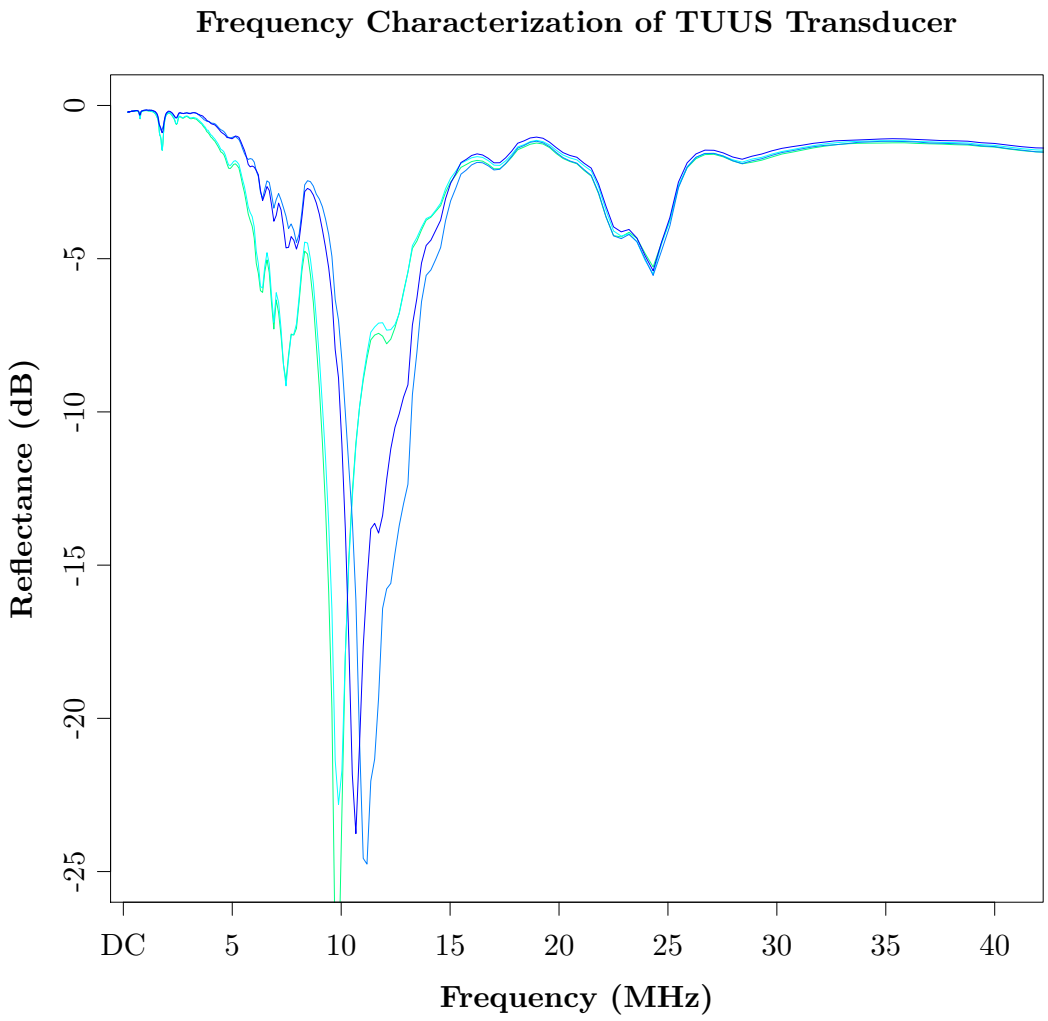

Figure 6.13: Frequency characterization of polyimide-based TUUS array. Array elements are matched at 10 MHz, and 25Ω impedance.

TUUS transducer array was driven at 10 MHz by the system electronics, and acoustic data was successfully captured and processed. Despite the different resonant frequencies of each transducer element, the versatility of the imaging system allowed rapid modification of testing parameters, and enabled successful capture of ranging data.

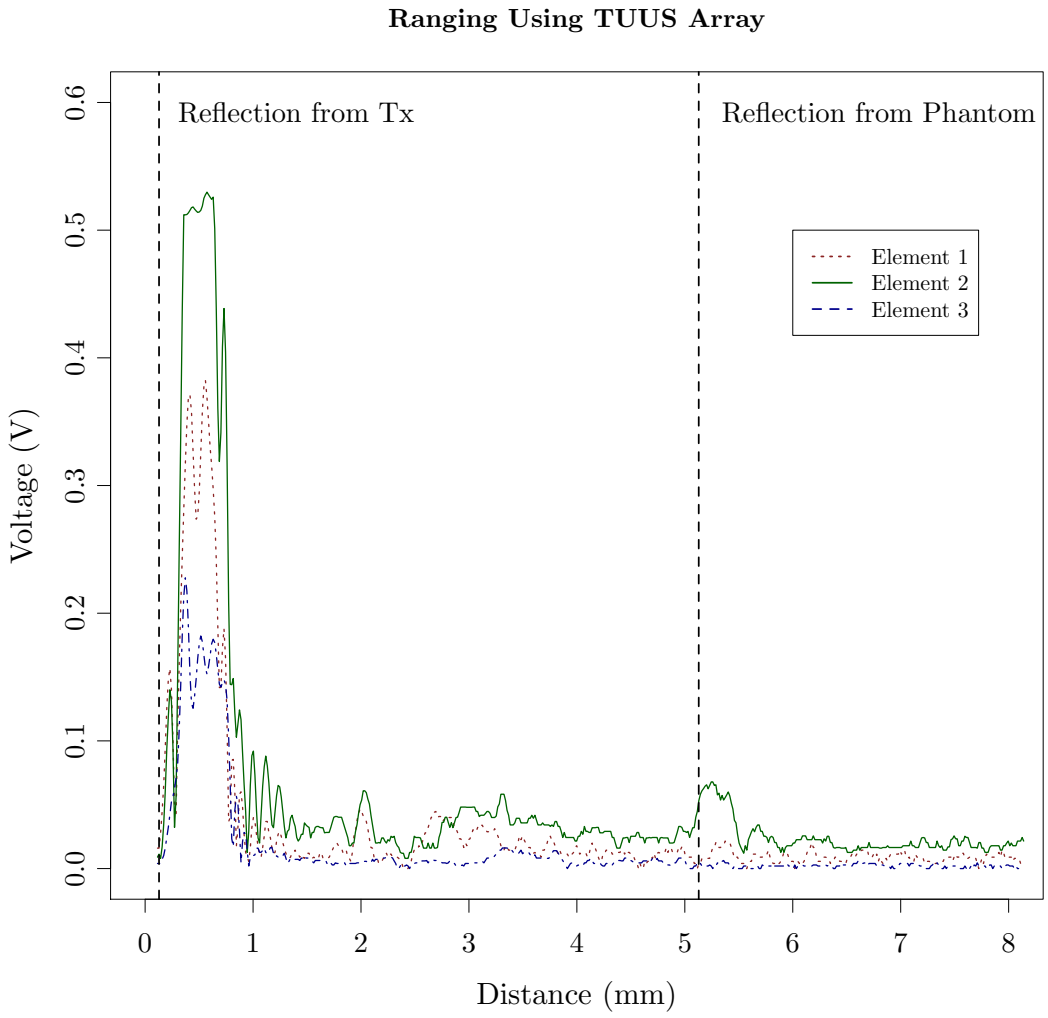

Figure 6.14: Acoustic data taken using polyimide-based TUUS array. Three elements were tested using multiple 10 MHz pulses. Figure represents the range profile of a metal target placed in water 5 mm from the TUUS array.

6.5 Discussion

A portable and robust prostate imaging system was developed and validated. The testing described in this chapter represents a proof of concept for an improved transurethral ultrasound imaging system that will facilitate future studies. Image pro-

cessing, system electronics, and transducer fabrication, were demonstrated, as well as integration of all three components. The system electronics were verified for range and frequency accuracy, and imaging studies were conducted utilizing a conventional Acuson linear array transducer. Synthetic transmit aperture was also demonstrated in this system using a flexible transducer array.

A multi-dimensional array design and robust signal processing capability was developed, overcoming the fundamental limitations of the TUUS system in the previous chapter. The previous TUUS studies utilized an IVUS imaging catheter transducer, which required linear pullback to capture multiple imaging planes. Furthermore, the fixed depth of penetration afforded by the system made visualization of the largest phantoms difficult. Interface with this transducer and the system described here (RDIP) was attempted. However, the array design included an embedded chip that prevented arbitrary signal processing techniques to be used.

There were a number of limitations discovered during the development of this imaging system. First, the original design requirements of a 9-12 MHz transducer array were met, but the low number of working PZT elements and poor durability prevented imaging. The transducer design, interconnect, and packaging require refinement in order to protect against mechanical stresses, such as shearing and bending of the polyimide layer. This was exacerbated by the outer placement of the column (ground) leads, as any discontinuity in these wires rendered the entire transducer inoperative. A potential improvement would be to deposit a thicker layer of polyimide, and to pattern a redundant grounding wire. Additionally, the interconnect should isolate the tension in the catheter wire from the transducer array. A high-density transducer array, necessary for real-time 3D imaging of the entire prostate, requires improved reliability in the fabrication and assembly process. Further development of the transducer array is necessary for *in vivo* studies to be conducted.

Chapter 7

Conclusions and Future Directions

We have thus described and tested the use of MR-Ultrasound fusion for prostate cancer diagnosis. Suspicious findings on MRI are correlated with both cancer presence and severity. Targeted biopsy using MR-US fusion appears to have a dramatic impact in men with prior negative biopsies and elevated PSA. In men on active surveillance, refinement of the MR scoring system is needed as there was no difference between image grade 2, 3, and 4. In both cases systematic biopsy is still required until the registration and targeting accuracy can be improved. Failure in targeting occurred in both very small and very large prostates, and was influenced by patient motion and biopsy technique.

Qualitative improvements to prostate visualization and MR-US fusion were achieved using a novel imaging method, transurethral ultrasound. Results from the clinical testing informed the development this prostate imaging system to be developed. 3D TUUS volumes were initially captured with a commercial intravascular ultrasound catheter transducer, and reconstructed into 3D. We discovered that this method was limited in the ability to vary imaging parameters, such as depth of penetration and signaling technique, necessary for visualization of larger prostates. We developed and tested a prostate imaging system that allowed for signal transmission and reception parameters to be dynamically reconfigured. A multi-row, multi-column catheter-based transducer was developed that utilized flexible polyimide joints. The entire system was validated through *in vitro* experimentation. Further development of a higher density transducer array is necessary before real-time 3D imaging of the entire

prostate can be implemented.

A potential expansion of fusion imaging is with focal therapy [122, 123]. If cancer can truly be localized and diagnosed, then perhaps it can be targeted with any number of ablative technologies. An interesting point is that the accuracy requirements for MR-Ultrasound fusion in therapy are relaxed compared to diagnosis. In the current version of focal therapy, an entire hemisphere of the prostate is irradiated or treated. The meaning of focal in this context is related to laterality. There are groups investigating the ablation of specific cancers, but these studies are still preliminary [230–232].

If cancer can be accurately staged and found upon diagnosis, truly focal ablation is enabled. Improving fusion technology, particularly the targeting and image registration, is thus key to raising its clinical utility. Transurethral ultrasound offers a potentially superior alternative. This thesis described the preliminary exploration and *in vitro* implementation of TUUS. Qualitatively, MR-TUUS fusion using current catheter technology is not only possible, but can be implemented using existing registration algorithms. Proving its efficacy *in vivo* will be key in future studies.

Chapter A

TNM Staging System

Primary Tumor (T)	
TX	Primary tumor cannot be evaluated
T0	No evidence of primary tumor
T1	Tumor is confined inside gland, but not clinically detectable, or with imaging
T2a	Tumor is organ-confined, and palpable
T3	Tumor extends through the prostatic capsule and/or to the seminal vesicles
T4	Tumor has spread to the neck of the bladder, the external sphincter, the rectum and/or wall of the pelvis.
Regional Lymph Nodes (N)	
NX	Regional lymph nodes cannot be evaluated
N0	No regional lymph node involvement
N1	Cancer has spread to a single lymph node
N2	Cancer has spread to multiple lymph nodes
Distant Metastasis (M)	
MX	Distant metastasis cannot be evaluated
M0	No distant metastasis
M1	Distant metastasis is present

Chapter B

Creative Commons License

ment of music or other alterations of a literary or artistic work, or phonogram or performance and includes cinematographic adaptations or any other form in which the Work may be recast, transformed, or adapted including in any form recognizably derived from the original, except that a work that constitutes a Collection will not be considered an Adaptation for the purpose of this License. For the avoidance of doubt, where the Work is a musical work, performance or phonogram, the synchronization of the Work in timed-relation with a moving image ("synching") will be considered an Adaptation for the purpose of this License.

"Collection" means a collection of literary or artistic works, such as encyclopedias and anthologies, or performances, phonograms or broadcasts, or other works or subject matter other than works listed in Section 1(f) below, which, by reason of the selection and arrangement of their contents, constitute intellectual creations, in which the Work is included in its entirety in unmodified form along with one or more other contributions, each constituting separate and independent works in themselves, which together are assembled into a collective whole. A work that constitutes a Collection will not be considered an Adaptation (as defined above) for the purposes of this License.

"Distribute" means to make available to the public the original and copies of the Work through sale or other transfer of ownership.

"Licensor" means the individual, individuals, entity or entities that offer(s) the Work under the terms of this License.

"Original Author" means, in the case of a literary or artistic work, the individual, individuals, entity or entities who created the Work or if no individual or entity can be identified, the publisher; and in addition (i) in the case of a performance the actors, singers, musicians, dancers, and other persons who act, sing, deliver, declaim, play in, interpret or otherwise perform literary or artistic works or expressions of

folklore; (ii) in the case of a phonogram the producer being the person or legal entity who first fixes the sounds of a performance or other sounds; and, (iii) in the case of broadcasts, the organization that transmits the broadcast.

"Work" means the literary and/or artistic work offered under the terms of this License including without limitation any production in the literary, scientific and artistic domain, whatever may be the mode or form of its expression including digital form, such as a book, pamphlet and other writing; a lecture, address, sermon or other work of the same nature; a dramatic or dramatico-musical work; a choreographic work or entertainment in dumb show; a musical composition with or without words; a cinematographic work to which are assimilated works expressed by a process analogous to cinematography; a work of drawing, painting, architecture, sculpture, engraving or lithography; a photographic work to which are assimilated works expressed by a process analogous to photography; a work of applied art; an illustration, map, plan, sketch or three-dimensional work relative to geography, topography, architecture or science; a performance; a broadcast; a phonogram; a compilation of data to the extent it is protected as a copyrightable work; or a work performed by a variety or circus performer to the extent it is not otherwise considered a literary or artistic work.

"You" means an individual or entity exercising rights under this License who has not previously violated the terms of this License with respect to the Work, or who has received express permission from the Licensor to exercise rights under this License despite a previous violation.

"Publicly Perform" means to perform public recitations of the Work and to communicate to the public those public recitations, by any means or process, including by wire or wireless means or public digital performances; to make available to the public Works in such a way that members of the public may access these Works from a place and at a place individually chosen by them; to perform the Work to the public

by any means or process and the communication to the public of the performances of the Work, including by public digital performance; to broadcast and rebroadcast the Work by any means including signs, sounds or images.

"Reproduce" means to make copies of the Work by any means including without limitation by sound or visual recordings and the right of fixation and reproducing fixations of the Work, including storage of a protected performance or phonogram in digital form or other electronic medium.

2. Fair Dealing Rights. Nothing in this License is intended to reduce, limit, or restrict any uses free from copyright or rights arising from limitations or exceptions that are provided for in connection with the copyright protection under copyright law or other applicable laws.

3. License Grant. Subject to the terms and conditions of this License, Licensor hereby grants You a worldwide, royalty-free, non-exclusive, perpetual (for the duration of the applicable copyright) license to exercise the rights in the Work as stated below:

a. to Reproduce the Work, to incorporate the Work into one or more Collections, and to Reproduce the Work as incorporated in the Collections; and,

b. to Distribute and Publicly Perform the Work including as incorporated in Collections. The above rights may be exercised in all media and formats whether now known or hereafter devised. The above rights include the right to make such modifications as are technically necessary to exercise the rights in other media and formats, but otherwise you have no rights to make Adaptations. Subject to 8(f), all rights not expressly granted by Licensor are hereby reserved, including but not limited to the rights set forth in Section 4(d).

4. Restrictions. The license granted in Section 3 above is expressly made subject to and limited by the following restrictions:

a. You may Distribute or Publicly Perform the Work only under the terms of this License. You must include a copy of, or the Uniform Resource Identifier (URI) for, this License with every copy of the Work You Distribute or Publicly Perform. You may not offer or impose any terms on the Work that restrict the terms of this License or the ability of the recipient of the Work to exercise the rights granted to that recipient under the terms of the License. You may not sublicense the Work. You must keep intact all notices that refer to this License and to the disclaimer of warranties with every copy of the Work You Distribute or Publicly Perform. When You Distribute or Publicly Perform the Work, You may not impose any effective technological measures on the Work that restrict the ability of a recipient of the Work from You to exercise the rights granted to that recipient under the terms of the License. This Section 4(a) applies to the Work as incorporated in a Collection, but this does not require the Collection apart from the Work itself to be made subject to the terms of this License. If You create a Collection, upon notice from any Licensor You must, to the extent practicable, remove from the Collection any credit as required by Section 4(c), as requested.

b. You may not exercise any of the rights granted to You in Section 3 above in any manner that is primarily intended for or directed toward commercial advantage or private monetary compensation. The exchange of the Work for other copyrighted works by means of digital file-sharing or otherwise shall not be considered to be intended for or directed toward commercial advantage or private monetary compensation, provided there is no payment of any monetary compensation in connection with the exchange of copyrighted works.

c. If You Distribute, or Publicly Perform the Work or Collections, You must, unless a request has been made pursuant to Section 4(a), keep intact all copyright notices for the Work and provide, reasonable to the medium or means You are uti-

lizing: (i) the name of the Original Author (or pseudonym, if applicable) if supplied, and/or if the Original Author and/or Licensor designate another party or parties (e.g., a sponsor institute, publishing entity, journal) for attribution ("Attribution Parties") in Licensor's copyright notice, terms of service or by other reasonable means, the name of such party or parties; (ii) the title of the Work if supplied; (iii) to the extent reasonably practicable, the URI, if any, that Licensor specifies to be associated with the Work, unless such URI does not refer to the copyright notice or licensing information for the Work. The credit required by this Section 4(c) may be implemented in any reasonable manner; provided, however, that in the case of a Collection, at a minimum such credit will appear, if a credit for all contributing authors of Collection appears, then as part of these credits and in a manner at least as prominent as the credits for the other contributing authors. For the avoidance of doubt, You may only use the credit required by this Section for the purpose of attribution in the manner set out above and, by exercising Your rights under this License, You may not implicitly or explicitly assert or imply any connection with, sponsorship or endorsement by the Original Author, Licensor and/or Attribution Parties, as appropriate, of You or Your use of the Work, without the separate, express prior written permission of the Original Author, Licensor and/or Attribution Parties.

d. For the avoidance of doubt:

i. **Non-waivable Compulsory License Schemes.** In those jurisdictions in which the right to collect royalties through any statutory or compulsory licensing scheme cannot be waived, the Licensor reserves the exclusive right to collect such royalties for any exercise by You of the rights granted under this License;

ii. **Waivable Compulsory License Schemes.** In those jurisdictions in which the right to collect royalties through any statutory or compulsory licensing scheme can be waived, the Licensor reserves the exclusive right to collect such royalties for

any exercise by You of the rights granted under this License if Your exercise of such rights is for a purpose or use which is otherwise than noncommercial as permitted under Section 4(b) and otherwise waives the right to collect royalties through any statutory or compulsory licensing scheme; and,

iii. **Voluntary License Schemes.** The Licensor reserves the right to collect royalties, whether individually or, in the event that the Licensor is a member of a collecting society that administers voluntary licensing schemes, via that society, from any exercise by You of the rights granted under this License that is for a purpose or use which is otherwise than noncommercial as permitted under Section 4(b).

e. Except as otherwise agreed in writing by the Licensor or as may be otherwise permitted by applicable law, if You Reproduce, Distribute or Publicly Perform the Work either by itself or as part of any Collections, You must not distort, mutilate, modify or take other derogatory action in relation to the Work which would be prejudicial to the Original Author's honor or reputation.

5. Representations, Warranties and Disclaimer

UNLESS OTHERWISE MUTUALLY AGREED BY THE PARTIES IN WRITING, LICENSOR OFFERS THE WORK AS-IS AND MAKES NO REPRESENTATIONS OR WARRANTIES OF ANY KIND CONCERNING THE WORK, EXPRESS, IMPLIED, STATUTORY OR OTHERWISE, INCLUDING, WITHOUT LIMITATION, WARRANTIES OF TITLE, MERCHANTIBILITY, FITNESS FOR A PARTICULAR PURPOSE, NONINFRINGEMENT, OR THE ABSENCE OF LATENT OR OTHER DEFECTS, ACCURACY, OR THE PRESENCE OF ABSENCE OF ERRORS, WHETHER OR NOT DISCOVERABLE. SOME JURISDICTIONS DO NOT ALLOW THE EXCLUSION OF IMPLIED WARRANTIES, SO SUCH EXCLUSION MAY NOT APPLY TO YOU.

6. Limitation on Liability. EXCEPT TO THE EXTENT REQUIRED BY APPLICABLE LAW, IN NO EVENT WILL LICENSOR BE LIABLE TO YOU ON ANY LEGAL THEORY FOR ANY SPECIAL, INCIDENTAL, CONSEQUENTIAL, PUNITIVE OR EXEMPLARY DAMAGES ARISING OUT OF THIS LICENSE OR THE USE OF THE WORK, EVEN IF LICENSOR HAS BEEN ADVISED OF THE POSSIBILITY OF SUCH DAMAGES.

7. Termination

a. This License and the rights granted hereunder will terminate automatically upon any breach by You of the terms of this License. Individuals or entities who have received Collections from You under this License, however, will not have their licenses terminated provided such individuals or entities remain in full compliance with those licenses. Sections 1, 2, 5, 6, 7, and 8 will survive any termination of this License.

b. Subject to the above terms and conditions, the license granted here is perpetual (for the duration of the applicable copyright in the Work). Notwithstanding the above, Licensor reserves the right to release the Work under different license terms or to stop distributing the Work at any time; provided, however that any such election will not serve to withdraw this License (or any other license that has been, or is required to be, granted under the terms of this License), and this License will continue in full force and effect unless terminated as stated above.

8. Miscellaneous

a. Each time You Distribute or Publicly Perform the Work or a Collection, the Licensor offers to the recipient a license to the Work on the same terms and conditions as the license granted to You under this License.

b. If any provision of this License is invalid or unenforceable under applicable law, it shall not affect the validity or enforceability of the remainder of the terms of this License, and without further action by the parties to this agreement, such provision

shall be reformed to the minimum extent necessary to make such provision valid and enforceable.

c. No term or provision of this License shall be deemed waived and no breach consented to unless such waiver or consent shall be in writing and signed by the party to be charged with such waiver or consent.

d. This License constitutes the entire agreement between the parties with respect to the Work licensed here. There are no understandings, agreements or representations with respect to the Work not specified here. Licensor shall not be bound by any additional provisions that may appear in any communication from You. This License may not be modified without the mutual written agreement of the Licensor and You.

e. The rights granted under, and the subject matter referenced, in this License were drafted utilizing the terminology of the Berne Convention for the Protection of Literary and Artistic Works (as amended on September 28, 1979), the Rome Convention of 1961, the WIPO Copyright Treaty of 1996, the WIPO Performances and Phonograms Treaty of 1996 and the Universal Copyright Convention (as revised on July 24, 1971). These rights and subject matter take effect in the relevant jurisdiction in which the License terms are sought to be enforced according to the corresponding provisions of the implementation of those treaty provisions in the applicable national law. If the standard suite of rights granted under applicable copyright law includes additional rights not granted under this License, such additional rights are deemed to be included in the License; this License is not intended to restrict the license of any rights under applicable law.

Creative Commons Notice

Creative Commons is not a party to this License, and makes no warranty whatsoever in connection with the Work. Creative Commons will not be liable to You or any party on any legal theory for any damages whatsoever, including without limita-

tion any general, special, incidental or consequential damages arising in connection to this license. Notwithstanding the foregoing two (2) sentences, if Creative Commons has expressly identified itself as the Licensor hereunder, it shall have all rights and obligations of Licensor.

Except for the limited purpose of indicating to the public that the Work is licensed under the CCPL, Creative Commons does not authorize the use by either party of the trademark "Creative Commons" or any related trademark or logo of Creative Commons without the prior written consent of Creative Commons. Any permitted use will be in compliance with Creative Commons' then-current trademark usage guidelines, as may be published on its website or otherwise made available upon request from time to time. For the avoidance of doubt, this trademark restriction does not form part of this License.

Creative Commons may be contacted at `http://creativecommons.org/`.

References

[1] R. Siegel, E. Ward, O. Brawley, and A. Jemal, "Cancer statistics, 2011," *CA: a cancer journal for clinicians*, 2011.

[2] D. Barocas, J. Cowan, J. Smith Jr, P. Carroll, *et al.*, "What percentage of patients with newly diagnosed carcinoma of the prostate are candidates for surveillance? an analysis of the capsure (tm) database," *The Journal of urology*, vol. 180, no. 4, pp. 1330–1335, 2008.

[3] A. Bill-Axelson, L. Holmberg, M. Ruutu, M. Häggman, S. Andersson, S. Bratell, A. Spångberg, C. Busch, S. Nordling, H. Garmo, *et al.*, "Radical prostatectomy versus watchful waiting in early prostate cancer," *New England Journal of Medicine*, vol. 352, no. 19, pp. 1977–1984, 2005.

[4] R. van den Bergh, M. Essink-Bot, M. Roobol, T. Wolters, F. Schröder, C. Bangma, and E. Steyerberg, "Anxiety and distress during active surveillance for early prostate cancer," *Cancer*, vol. 115, no. 17, pp. 3868–3878, 2009.

[5] A. Roth, B. Rosenfeld, A. Kornblith, C. Gibson, H. Scher, T. Curley-Smart, J. Holland, and W. Breitbart, "The memorial anxiety scale for prostate cancer," *Cancer*, vol. 97, no. 11, pp. 2910–2918, 2003.

[6] M. R. Cooperberg, J. M. Broering, P. W. Kantoff, and P. R. Carroll, "Contemporary trends in low risk prostate cancer: risk assessment and treatment," *J Urol*, vol. 178, no. 3 Pt 2, pp. S14–9, 2007. Cooperberg, Matthew R Broering, Jeannette M Kantoff, Philip W Carroll, Peter R United States The Journal of urology S0022-5347(07)00823-3 J Urol. 2007 Sep;178(3 Pt 2):S14-9. Epub 2007 Jul 20.

[7] S. Sriprasad, M. Feneley, and P. Thompson, "History of prostate cancer treatment," *Surgical Oncology*, vol. 18, no. 3, pp. 185–191, 2009.

[8] W. Catalona, J. Richie, F. Ahmann, M. Hudson, P. Scardino, R. Flanigan, J. Dekernion, T. Ratliff, L. Kavoussi, B. Dalkin, *et al.*, "Comparison of digital rectal examination and serum prostate specific antigen in the early detection of prostate cancer: results of a multicenter clinical trial of 6,630 men.," *The Journal of urology*, vol. 151, no. 5, p. 1283, 1994.

[9] J. Smith, P. Scardino, M. Resnick, A. Hernandez, S. Rose, M. Egger, *et al.*, "Transrectal ultrasound versus digital rectal examination for the staging of carcinoma of the prostate: results of a prospective, multi-institutional trial," *The Journal of urology*, vol. 157, no. 3, pp. 902–906, 1997.

[10] D. Smith and W. Catalona, "Interexaminer variability of digital rectal examination in detecting prostate cancer," *Urology*, vol. 45, no. 1, pp. 70–74, 1995.

[11] R. Ferguson, "Prostatic neoplasms:: Their diagnosis by needle puncture and aspiration," *The American Journal of Surgery*, vol. 9, no. 3, pp. 507–511, 1930.

[12] S. Franzen, G. Giertz, and J. Zajicek, "Cytological diagnosis of prostatic tumours by transrectal aspiration biopsy: a preliminary report," *British journal of urology*, vol. 32, no. 2, pp. 193–196, 1960.

[13] A. Astraldi, "Diagnosis of cancer of the prostate: biopsy by rectal route," *Urol Cutan Rev*, vol. 41, p. 421, 1937.

[14] I. Silverman, "A new biopsy needle," *The American Journal of Surgery*, vol. 40, no. 3, pp. 671–672, 1938.

[15] H. Grabstald and J. Elliott, "Transrectal biopsy of the prostate," *Journal of the American Medical Association*, vol. 153, no. 6, p. 563, 1953.

[16] J. Kaufman, M. Rosenthal, W. Goodwin, *et al.*, "Methods of diagnosis of carcinoma of the prostate: a comparison of clinical impression, prostatic smear, needle biopsy, open perineal biopsy and transurethral biopsy.," *The Journal of urology*, vol. 72, no. 3, p. 450, 1954.

[17] W. Hendry and J. Williams, "Transrectal prostatic biopsy," *British medical journal*, vol. 4, no. 5787, pp. 595–597, 1971.

[18] J. Kaufman and J. Schultz, "Needle biopsy of the prostate: a re-evaluation.," *The Journal of urology*, vol. 87, p. 164, 1962.

[19] J. Kaufman, B. Ljung, P. Walther, and J. Waisman, "Aspiration biopsy of prostate," *Urology*, vol. 19, no. 6, pp. 587–591, 1982.

[20] J. Eble and P. Angermeier, "The roles of fine needle aspiration and needle core biopsies in the diagnosis of primary prostatic cancer," *Human pathology*, vol. 23, no. 3, pp. 249–257, 1992.

[21] K. Hodge, J. McNeal, M. Terris, and T. Stamey, "Random systematic versus directed ultrasound guided transrectal core biopsies of the prostate.," *The Journal of urology*, vol. 142, no. 1, p. 71, 1989.

[22] G. Murphy and W. Whitmore Jr, "A report of the workshops on the current status of the histologic grading of prostate cancer," *Cancer*, vol. 44, no. 4, pp. 1490–1494, 1979.

[23] D. Gleason, "Classification of prostatic carcinomas.," *Cancer chemotherapy reports. Part 1*, vol. 50, no. 3, p. 125, 1966.

[24] D. Gleason and G. Mellinger, "The veterans administration cooperative urological research group: Prediction of prognosis for prostatic adenocarcinoma by combined histological grading and clinical staging," *J Urol*, vol. 111, pp. 58–64, 1974.

[25] J. Oesterling, C. Brendler, J. Epstein, A. Kimball Jr, P. Walsh, *et al.*, "Correlation of clinical stage, serum prostatic acid phosphatase and preoperative gleason grade with final pathological stage in 275 patients with clinically localized adenocarcinoma of the prostate.," *The Journal of urology*, vol. 138, no. 1, p. 92, 1987.

[26] D. Gleason, "Histologic grading of prostate cancer: a perspective," *Human pathology*, vol. 23, no. 3, pp. 273–279, 1992.

[27] F. Schröder, P. Hermanek, L. Denis, W. Fair, M. Gospodarowicz, and M. Pavone-Macaluso, "The tnm classification of prostate cancer," *The Prostate*, vol. 21, no. S4, pp. 129–138, 1992.

[28] H. Watanabe, H. Kato, T. Kato, M. Morita, and M. Tanaka, "Diagnostic application of ultrasonotomography to the prostate," *Nippon Hinyōkika Gakkai zasshi. The japanese journal of urology*, vol. 59, no. 4, p. 273, 1968.

[29] H. Watanabe, D. Igari, Y. Tanahashi, K. Harada, and M. Saitoh, "Measurements of size and weight of prostate by means of transrectal ultrasonotomography," *The Tohoku Journal of Experimental Medicine*, vol. 114, no. 3, pp. 277–85, 1974.

[30] F. Lee, R. McLeary, G. Kumasaka, G. Borlaza, W. Straub, J. Gray, T. Meadows, F. Lee Jr, M. Solomon, T. McHugh, *et al.*, "Transrectal ultrasound in the diagnosis of prostate cancer: location, echogenicity, histopathology, and staging," *The Prostate*, vol. 7, no. 2, pp. 117–29, 1985.

[31] K. Shinohara, T. Wheeler, and P. Scardino, "The appearance of prostate cancer on transrectal ultrasonography: correlation of imaging and pathological examinations.," *The Journal of urology*, vol. 142, no. 1, pp. 76–82, 1989.

[32] M. Rifkin, E. Zerhouni, C. Gatsonis, L. Quint, D. Paushter, J. Epstein, U. Hamper, P. Walsh, and B. McNeil, "Comparison of magnetic resonance imaging and ultrasonography in staging early prostate cancer," *New England Journal of Medicine*, vol. 323, no. 10, pp. 621–626, 1990.

[33] F. Cornud, X. Belin, D. Piron, Y. Chretien, T. Flam, J. Casanova, and O. Helenon, "Color Doppler-guided prostate biopsies in 591 patients with an elevated serum PSA level: impact on Gleason score for nonpalpable lesions," *Urology*, vol. 49, no. 5, pp. 709–715, 1997.

[34] J. Newman, R. Bree, and J. Rubin, "Prostate cancer: diagnosis with color Doppler sonography with histologic correlation of each biopsy site.," *Radiology*, vol. 195, no. 1, pp. 86–90, 1995.

[35] M. Rifkin, G. Sudakoff, and A. Alexander, "Prostate: techniques, results, and potential applications of color Doppler US scanning.," *Radiology*, vol. 186, no. 2, pp. 509–13, 1993.

[36] E. Trabulsi, D. Sackett, L. Gomella, and E. Halpern, "Enhanced Transrectal Ultrasound Modalities in the Diagnosis of Prostate Cancer," *Urology*, vol. 76, no. 5, pp. 1025–33, 2010.

[37] E. Halpern, F. Frauscher, S. Strup, L. Nazarian, P. O'Kane, and L. Gomella, "Prostate: High-Frequency Doppler US Imaging for Cancer Detection1," *Radiology*, vol. 225, no. 1, p. 71, 2002.

[38] O. Akin and H. Hricak, "Imaging of prostate cancer," *Radiologic Clinics of North America*, vol. 45, no. 1, pp. 207–22, 2007.

[39] E. Halpern, J. Ramey, S. Strup, F. Frauscher, P. McCue, and L. Gomella, "Detection of prostate carcinoma with contrast-enhanced sonography using intermittent harmonic imaging," *Cancer*, vol. 104, no. 11, pp. 2373–83, 2005.

[40] T. Stamey, F. Freiha, J. McNeal, E. Redwine, A. Whittemore, and H. Schmid, "Localized prostate cancer. Relationship of tumor volume to clinical significance for treatment of prostate cancer," *Cancer*, vol. 71, no. S3, pp. 933–938, 1993.

[41] J. Afnan and C. Tempany, "Update on Prostate Imaging," *Urologic Clinics of North America*, vol. 37, no. 1, pp. 23–5, 2010.

[42] M. Kuriyama, M. Wang, L. Papsidero, C. Killian, T. Shimano, L. Valenzuela, T. Nishiura, G. Murphy, and T. Chu, "Quantitation of prostate-specific antigen in serum by a sensitive enzyme immunoassay," *Cancer research*, vol. 40, no. 12, p. 4658, 1980.

[43] M. Wang, L. Papsidero, M. Kuriyama, L. Valenzuela, G. Murphy, and T. Chu, "Prostate antigen: a new potential marker for prostatic cancer," *The Prostate*, vol. 2, no. 1, pp. 89–96, 1981.

[44] J. Myrtle, P. Klimley, L. Ivor, J. Bruni, *et al.*, "Clinical utility of prostate specific antigen (psa) in the management of prostate cancer," *Advances in cancer diagnostics*, vol. 1, pp. 1–7, 1986.

[45] G. Draisma, R. Boer, S. Otto, I. Van Der Cruijsen, R. Damhuis, F. Schröder, and H. De Koning, "Lead times and overdetection due to prostate-specific antigen screening: estimates from the european randomized study of screening for prostate cancer," *Journal of the National Cancer Institute*, vol. 95, no. 12, pp. 868–878, 2003.

[46] T. A. Stamey, M. Caldwell, J. E. McNeal, R. Nolley, M. Hemenez, and J. Downs, "The prostate specific antigen era in the united states is over for prostate cancer: what happened in the last 20 years?," *J Urol*, vol. 172, no. 4 Pt 1, pp. 1297–301, 2004. 0022-5347 (Print) Journal Article.

[47] T. Stamey, N. Yang, A. Hay, J. McNeal, F. Freiha, and E. Redwine, "Prostate-specific antigen as a serum marker for adenocarcinoma of the prostate," *New England Journal of Medicine*, vol. 317, no. 15, pp. 909–916, 1987.

[48] A. Partin, J. Yoo, H. Carter, J. Pearson, D. Chan, J. Epstein, P. Walsh, *et al.*, "The use of prostate specific antigen, clinical stage and gleason score to predict pathological stage in men with localized prostate cancer.," *The Journal of urology*, vol. 150, no. 1, p. 110, 1993.

[49] L. Marks, Y. Fradet, I. Lim Deras, A. Blase, J. Mathis, S. Aubin, A. Cancio, M. Desaulniers, W. Ellis, H. Rittenhouse, *et al.*, "Pca3 molecular urine assay for prostate cancer in men undergoing repeat biopsy," *Urology*, vol. 69, no. 3, pp. 532–535, 2007.

[50] P. Sutcliffe, S. Hummel, E. Simpson, T. Young, A. Rees, A. Wilkinson, F. Hamdy, N. Clarke, and J. Staffurth, "Use of classical and novel biomarkers as prognostic risk factors for localised prostate cancer: a systematic review," *Health Technol Assess*, vol. 13, no. 5, pp. 1–219, 2009. Sutcliffe, P Hummel, S Simpson, E Young, T Rees, A Wilkinson, A Hamdy, F Clarke, N Staffurth, J Review England Health technology assessment (Winchester, England) Health Technol Assess. 2009 Jan;13(5):iii, xi-xiii 1-219.

[51] C. Roehrborn, G. John Pickens, and J. Sanders, "Diagnostic yield of repeated transrectal ultrasound-guided biopsies stratified by specific histopathologic diagnoses and prostate-specific antigen levels," *Urology*, vol. 47, no. 3, pp. 347–352, 1996.

[52] J. Wei, "Limitations of a contemporary prostate biopsy: The blind march forward," *Urologic Oncology*, vol. 28, no. 5, pp. 546–549, 2010.

[53] C. Bolenz, A. Gupta, T. Hotze, R. Ho, J. Cadeddu, C. Roehrborn, and Y. Lotan, "Cost comparison of robotic, laparoscopic, and open radical prostatectomy for prostate cancer," *European urology*, vol. 57, no. 3, pp. 453–458, 2010.

[54] A. Corcoran, P. Peele, and R. Benoit, "Cost comparison between watchful waiting with active surveillance and active treatment of clinically localized prostate cancer," *Urology*, vol. 76, no. 3, pp. 703–707, 2010.

[55] C. Bolenz, A. Gupta, C. Roehrborn, and Y. Lotan, "Predictors of costs for robotic-assisted laparoscopic radical prostatectomy," *Urologic Oncology: Seminars and Original Investigations*, vol. 29, no. 3, pp. 325–329, 2011.

[56] L. Wilson, R. Tesoro, E. Elkin, N. Sadetsky, J. Broering, D. Latini, J. DuChane, R. Mody, and P. Carroll, "Cumulative cost pattern comparison of prostate cancer treatments," *Cancer*, vol. 109, no. 3, pp. 518–527, 2007.

[57] A. Konski, D. Watkins-Bruner, S. Feigenberg, A. Hanlon, S. Kulkarni, J. Beck, E. Horwitz, and A. Pollack, "Using decision analysis to determine the cost-effectiveness of intensity-modulated radiation therapy in the treatment of intermediate risk prostate cancer," *International Journal of Radiation Oncology* Biology* Physics*, vol. 66, no. 2, pp. 408–415, 2006.

[58] A. Konski, W. Speier, A. Hanlon, J. Beck, and A. Pollack, "Is proton beam therapy cost effective in the treatment of adenocarcinoma of the prostate?," *Journal of Clinical Oncology*, vol. 25, no. 24, pp. 3603–3608, 2007.

[59] G. Dooms and H. Hricak, "Magnetic resonance imaging of the pelvis: prostate and urinary bladder," *Urol Radiol*, vol. 8, no. 1, pp. 156–65, 1986.

[60] P. Narayan, D. Vigneron, P. Jajodia, C. Anderson, M. Hedgcock, E. Tanagho, and T. James, "Transrectal probe for 1H MRI and 31P MR spectroscopy of the prostate gland," *Magnetic Resonance in Medicine*, vol. 11, no. 2, pp. 209–220, 1989.

[61] E. Outwater, R. Petersen, E. Siegelman, L. Gomella, C. Chernesky, and D. Mitchell, "Prostate carcinoma: assessment of diagnostic criteria for capsular penetration on endorectal coil MR images.," *Radiology*, vol. 193, no. 2, pp. 333–9, 1994.

[62] G. Brown, D. Macvicar, V. Ayton, and J. Husband, "The role of intravenous contrast enhancement in magnetic resonance imaging of prostatic carcinoma," *Clin Radiol*, vol. 50, no. 9, pp. 601–606, 1995.

[63] G. Jager, E. Ruijter, C. Van de Kaa, J. De la Rosette, G. Oosterhof, J. Thornbury, S. Ruijs, and J. Barentsz, "Dynamic TurboFLASH subtraction technique for contrast-enhanced MR imaging of the prostate: correlation with histopathologic results," *Radiology*, vol. 203, no. 3, pp. 645–52, 1997.

[64] M. Engelbrecht, H. Huisman, R. Laheij, G. Jager, G. van Leenders, C. Hulsbergen-Van De Kaa, J. de la Rosette, J. Blickman, and J. Barentsz, "Discrimination of Prostate Cancer from Normal Peripheral Zone and Central Gland Tissue by Using Dynamic Contrast-enhanced MR Imaging1," *Radiology*, vol. 229, no. 1, p. 248, 2003.

[65] L. Quint, J. Van Erp, P. Bland, E. Del Buono, S. Mandell, H. Grossman, and P. Gikas, "Prostate cancer: correlation of MR images with tissue optical density at pathologic examination," *Radiology*, vol. 179, no. 3, pp. 837–42, 1991.

[66] R. Alonzi, A. Padhani, and C. Allen, "Dynamic contrast enhanced MRI in prostate cancer," *European Journal of Radiology*, vol. 63, no. 3, pp. 335–350, 2007.

[67] I. Ocak, M. Bernardo, G. Metzger, T. Barrett, P. Pinto, P. Albert, and P. Choyke, "Dynamic contrast-enhanced MRI of prostate cancer at 3 T: a study of pharmacokinetic parameters," *Am J Roentgenol*, vol. 189, no. 4, pp. W192–201, 2007.

[68] F. van Dorsten, M. van der Graaf, M. Engelbrecht, G. van Leenders, A. Verhofstad, M. Rijpkema, J. de la Rosette, J. Barentsz, and A. Heerschap, "Combined quantitative dynamic contrast-enhanced MR imaging and 1H MR spectroscopic imaging of human prostate cancer," *Journal of Magnetic Resonance Imaging*, vol. 20, no. 2, pp. 279–287, 2004.

[69] A. Padhani, C. Gapinski, D. Macvicar, G. Parker, J. Suckling, P. Revell, M. Leach, D. Dearnaley, and J. Husband, "Dynamic contrast enhanced MRI of prostate cancer: correlation with morphology and tumour stage, histological grade and PSA," *Clinical radiology*, vol. 55, no. 2, pp. 99–109, 2000.

[70] J. Fütterer, M. Engelbrecht, H. Huisman, G. Jager, C. Hulsbergen-van De Kaa, J. Witjes, and J. Barentsz, "Staging Prostate Cancer with Dynamic Contrast-enhanced Endorectal MR Imaging prior to Radical Prostatectomy: Experienced versus Less Experienced Readers1," *Radiology*, vol. 237, no. 2, pp. 541–49, 2005.

[71] N. Girouin, F. Mege-Lechevallier, A. Tonina Senes, A. Bissery, M. Rabilloud, J. Marechal, M. Colombel, D. Lyonnet, and O. Rouviere, "Prostate dynamic contrast-enhanced MRI with simple visual diagnostic criteria: is it reasonable?," *European Radiology*, vol. 17, no. 6, pp. 1498–1509, 2007.

[72] A. Tanimoto, J. Nakashima, H. Kohno, H. Shinmoto, and S. Kuribayashi, "Prostate cancer screening: The clinical value of diffusion-weighted imaging and dynamic MR imaging in combination with T2-weighted imaging," *J Magn Reson*, vol. 25, no. 1, pp. 146–152, 2007.

[73] K. Kitajima, Y. Kaji, Y. Fukabori, K. Yoshida, N. Suganuma, and K. Sugimura, "Prostate cancer detection with 3 T MRI: Comparison of diffusion-weighted imaging and dynamic contrast-enhanced MRI in combination with T2-weighted imaging," *J Magn Reson*, vol. 31, no. 3, pp. 625–631, 2010.

[74] S. Sinha and U. Sinha, "In vivo diffusion tensor imaging of the human prostate," *Magn Reson Med*, vol. 52, no. 3, pp. 530–537, 2004.

[75] M. Pickles, P. Gibbs, M. Sreenivas, and L. Turnbull, "Diffusion-weighted imaging of normal and malignant prostate tissue at 3.0 T," *J Magn Reson*, vol. 23, no. 2, pp. 130–134, 2006.

[76] P. Gibbs, G. Liney, M. Pickles, B. Zelhof, G. Rodrigues, and L. Turnbull, "Correlation of ADC and T2 measurements with cell density in prostate cancer at 3.0 Tesla," *Investigative radiology*, vol. 44, no. 9, pp. 572–6, 2009.

[77] M. Haider, T. van der Kwast, J. Tanguay, A. Evans, A. Hashmi, G. Lockwood, and J. Trachtenberg, "Combined T2-weighted and diffusion-weighted MRI for localization of prostate cancer," *Am J Roentgenol*, vol. 189, no. 2, pp. 323–28, 2007.

[78] N. van As, E. Charles-Edwards, A. Jackson, S. Jhavar, S. Reinsberg, N. Desouza, D. Dearnaley, M. Bailey, A. Thompson, T. Christmas, *et al.*, "Correlation of diffusion-weighted MRI with whole mount radical prostatectomy specimens," *Br J Radiol*, vol. 81, no. 966, pp. 456–62, 2008.

[79] K. Yoshimitsu, K. Kiyoshima, H. Irie, T. Tajima, Y. Asayama, M. Hirakawa, K. Ishigami, S. Naito, and H. Honda, "Usefulness of apparent diffusion coefficient map in diagnosing prostate carcinoma: correlation with stepwise histopathology," *J Magn Reson*, vol. 27, no. 1, pp. 132–139, 2008.

[80] Y. Mazaheri, H. Hricak, S. Fine, O. Akin, A. Shukla-Dave, N. Ishill, C. Moskowitz, J. Grater, V. Reuter, K. Zakian, *et al.*, "Prostate Tumor Volume Measurement with Combined T2-weighted Imaging and Diffusion-weighted MR: Correlation with Pathologic Tumor Volume," *Radiology*, vol. 252, no. 2, pp. 449–57, 2009.

[81] C. Woodfield, G. Tung, D. Grand, J. Pezzullo, J. Machan, and J. Renzulli, "Diffusion-Weighted MRI of Peripheral Zone Prostate Cancer: Comparison of

Tumor Apparent Diffusion Coefficient With Gleason Score and Percentage of Tumor on Core Biopsy," *Am J Roentgenol*, vol. 194, no. 4, pp. W316–22, 2010.

[82] N. de Souza, S. Reinsberg, E. Scurr, J. Brewster, and G. Payne, "Magnetic resonance imaging in prostate cancer: the value of apparent diffusion coefficients for identifying malignant nodules," *Br J Radiol*, vol. 80, no. 950, pp. 90–5, 2007.

[83] N. de Souza, S. Riches, N. Vanas, V. Morgan, S. Ashley, C. Fisher, G. Payne, and C. Parker, "Diffusion-weighted magnetic resonance imaging: a potential non-invasive marker of tumour aggressiveness in localized prostate cancer," *Clin Radiol*, vol. 63, no. 7, pp. 774–82, 2008.

[84] N. van As, N. de Souza, S. Riches, V. Morgan, S. Sohaib, D. Dearnaley, and C. Parker, "A study of diffusion-weighted magnetic resonance imaging in men with untreated localised prostate cancer on active surveillance," *European urology*, vol. 56, no. 6, pp. 981–988, 2009.

[85] P. Kozlowski, S. Chang, E. Jones, K. Berean, H. Chen, and S. Goldenberg, "Combined diffusion-weighted and dynamic contrast-enhanced MRI for prostate cancer diagnosis—Correlation with biopsy and histopathology," *J Magn Reson*, vol. 24, no. 1, pp. 108–113, 2006.

[86] A. Oto, A. Kayhan, Y. Jiang, M. Tretiakova, C. Yang, T. Antic, F. Dahi, A. Shalhav, G. Karczmar, and W. Stadler, "Prostate Cancer: Differentiation of Central Gland Cancer from Benign Prostatic Hyperplasia by Using Diffusion-weighted and Dynamic Contrast-enhanced MR Imaging," *Radiology*, vol. 257, no. 3, pp. 715–23, 2010.

[87] B. Turkbey, S. Xu, J. Kruecker, J. Locklin, Y. Pang, M. Bernardo, M. Merino, B. Wood, P. Choyke, and P. Pinto, "Documenting the location of prostate biopsies with image fusion," *BJU international*, vol. 107, no. 1, pp. 53–57, 2010.

[88] D. Langer, T. van der Kwast, A. Evans, A. Plotkin, J. Trachtenberg, B. Wilson, and M. Haider, "Prostate Tissue Composition and MR Measurements: Investigating the Relationships between ADC, T2, Ktrans, ve, and Corresponding Histologic Features1," *Radiology*, vol. 255, no. 2, pp. 485–494, 2010.

[89] B. Park, H. Lee, C. Kim, H. Choi, and J. Park, "Lesion localization in patients with a previous negative transrectal ultrasound biopsy and persistently elevated prostate specific antigen level using diffusion-weighted imaging at three Tesla before rebiopsy," *Invest Radiol*, vol. 43, no. 11, pp. 789–93, 2008.

[90] S. Xu, J. Kruecker, B. Turkbey, N. Glossop, A. Singh, P. Choyke, P. Pinto, and B. Wood, "Real-time MRI-TRUS fusion for guidance of targeted prostate biopsies," *Comp Aid Surg*, vol. 13, no. 5, pp. 255–264, 2008.

[91] N. Lawrentschuk and N. Fleshner, "The role of magnetic resonance imaging in targeting prostate cancer in patients with previous negative biopsies and elevated prostate-specific antigen levels," *BJU international*, vol. 103, no. 6, pp. 730–3, 2009.

[92] J. Fütterer, S. Heijmink, T. Scheenen, J. Veltman, H. Huisman, P. Vos, C. de Kaa, J. Witjes, P. Krabbe, A. Heerschap, *et al.*, "Prostate Cancer Localization with Dynamic Contrast-enhanced MR Imaging and Proton MR Spectroscopic Imaging1," *Radiology*, vol. 241, no. 2, pp. 449–58, 2006.

[93] M. Chen, H. Dang, J. Wang, C. Zhou, S. Li, W. Wang, W. Zhao, Z. Yang, C. Zhong, and G. Li, "Prostate cancer detection: comparison of T2-weighted imaging, diffusion-weighted imaging, proton magnetic resonance spectroscopic imaging, and the three techniques combined," *Acta Radiologica*, vol. 49, no. 5, pp. 602–610, 2008.

[94] S. Riches, G. Payne, V. Morgan, S. Sandhu, C. Fisher, M. Germuska, D. Collins, A. Thompson, and N. deSouza, "MRI in the detection of prostate cancer: combined apparent diffusion coefficient, metabolite ratio, and vascular parameters," *Am J Roentgenol*, vol. 193, no. 6, pp. 1583–91, 2009.

[95] J. Weinreb, J. Blume, F. Coakley, T. Wheeler, J. Cormack, C. Sotto, H. Cho, A. Kawashima, C. Tempany-Afdhal, K. Macura, *et al.*, "Prostate Cancer: Sextant Localization at MR Imaging and MR Spectroscopic Imaging before Prostatectomy—Results of ACRIN Prospective Multi-institutional Clinicopathologic Study," *Radiology*, vol. 251, no. 1, pp. 122–33, 2009.

[96] S. Heijmink, J. Fütterer, T. Hambrock, S. Takahashi, T. Scheenen, H. Huisman, C. Hulsbergen-Van de Kaa, B. Knipscheer, L. Kiemeney, J. Witjes, *et al.*, "Prostate Cancer: Body-Array versus Endorectal Coil MR Imaging at 3 T—Comparison of Image Quality, Localization, and Staging Performance1," *Radiology*, vol. 244, no. 1, pp. 184–95, 2007.

[97] B. Park, B. Kim, C. Kim, H. Lee, and G. Kwon, "Comparison of phased-array 3.0-T and endorectal 1.5-T magnetic resonance imaging in the evaluation of local staging accuracy for prostate cancer," *J Comput Assist Tomogr*, vol. 31, no. 4, pp. 534–8, 2007.

[98] T. Hambrock, D. Somford, C. Hoeks, S. Bouwense, H. Huisman, D. Yakar, I. van Oort, J. Witjes, J. F

"utterer, and J. Barentsz, "Magnetic resonance imaging guided prostate biopsy in men with repeat negative biopsies and increased prostate specific antigen," *J Urol*, vol. 183, no. 2, pp. 520–8, 2010.

[99] K. Pondman, J. Fütterer, B. ten Haken, L. Schultze Kool, J. Witjes, T. Hambrock, K. Macura, and J. Barentsz, "MR-guided biopsy of the prostate: an overview of techniques and a systematic review," *European urology*, vol. 54, no. 3, pp. 517–527, 2008.

[100] A. D'amico, C. Tempany, R. Cormack, N. Hata, M. Jinzaki, K. Tuncali, M. Weinstein, and J. Richie, "Transperineal magnetic resonance image guided prostate biopsy," *The Journal of urology*, vol. 164, no. 2, pp. 385–387, 2000.

[101] R. Cormack, A. D'Amico, N. Hata, S. Silverman, M. Weinstein, and C. Tempany, "Feasibility of transperineal prostate biopsy under interventional magnetic resonance guidance," *Urology*, vol. 56, no. 4, pp. 663–664, 2000.

[102] S. DiMaio, S. Pieper, K. Chinzei, N. Hata, S. Haker, D. Kacher, G. Fichtinger, C. Tempany, and R. Kikinis, "Robot-assisted needle placement in open mri: system architecture, integration and validation.," *Computer aided surgery: official journal of the International Society for Computer Aided Surgery*, vol. 12, no. 1, p. 15, 2007.

[103] G. Fichtinger, A. Krieger, R. Susil, A. Tanacs, L. Whitcomb, and E. Atalar, "Transrectal prostate biopsy inside closed MRI scanner with remote actuation, under real-time image guidance," *Medical Image Computing and Computer-Assisted Intervention—MICCAI 2002*, pp. 91–98, 2002.

[104] G. Fichtinger, T. DeWeese, A. Patriciu, A. Tanacs, D. Mazilu, J. Anderson, K. Masamune, R. Taylor, and D. Stoianovici, "System for Robotically Assisted Prostate Biopsy and Therapy with Intraoperative CT Guidance* 1," *Academic Radiology*, vol. 9, no. 1, pp. 60–74, 2002.

[105] A. Krieger, R. Susil, C. Ménard, J. Coleman, G. Fichtinger, E. Atalar, and L. Whitcomb, "Design of a novel MRI compatible manipulator for image guided prostate interventions," *Biomedical Engineering, IEEE Transactions on*, vol. 52, no. 2, pp. 306–313, 2005.

[106] A. Krieger, C. Csoma, I. Iordachita, P. Guion, A. Singh, G. Fichtinger, and L. Whitcomb, "Design and preliminary accuracy studies of an mri-guided transrectal prostate intervention system," *Medical Image Computing and Computer-Assisted Intervention–MICCAI 2007*, pp. 59–67, 2007.

[107] A. Krieger, I. Iordachita, P. Guion, A. Singh, A. Kaushal, C. Menard, P. Pinto, K. Camphausen, G. Fichtinger, and L. Whitcomb, "An mri-compatible robotic system with hybrid tracking for mri-guided prostate intervention," *Biomedical Engineering, IEEE Transactions on*, no. 99, pp. 1–1, 2011.

[108] H. Tadayyon, A. Lasso, A. Kaushal, P. Guion, and G. Fichtinger, "Target motion tracking in mri-guided transrectal robotic prostate biopsy," *Biomedical Engineering, IEEE Transactions on*, no. 99, pp. 1–1, 2011.

[109] R. Susil, C. Ménard, A. Krieger, J. Coleman, K. Camphausen, P. Choyke, G. Fichtinger, L. Whitcomb, C. Coleman, and E. Atalar, "Transrectal prostate biopsy and fiducial marker placement in a standard 1.5 t magnetic resonance imaging scanner," *The Journal of urology*, vol. 175, no. 1, pp. 113–120, 2006.

[110] A. Singh, A. Krieger, J. Lattouf, P. Guion, R. Grubb, P. Albert, G. Metzger, K. Ullman, S. Smith, G. Fichtinger, *et al.*, "Patient selection determines the prostate cancer yield of dynamic contrast-enhanced magnetic resonance imaging-guided transrectal biopsies in a closed 3-tesla scanner," *BJU international*, vol. 101, no. 2, pp. 181–185, 2008.

[111] D. Beyersdorff, A. Winkel, B. Hamm, S. Lenk, S. Loening, and M. Taupitz, "Mr imaging–guided prostate biopsy with a closed mr unit at 1.5 t: Initial results1," *Radiology*, vol. 234, no. 2, pp. 576–581, 2005.

[112] T. Franiel, C. Stephan, A. Erbersdobler, E. Dietz, A. Maxeiner, N. Hell, A. Huppertz, K. Miller, R. Strecker, and B. Hamm, "Areas suspicious for prostate cancer: Mr–guided biopsy in patients with at least one transrectal us-guided biopsy with a negative finding—multiparametric mr imaging for detection and biopsy planning," *Radiology*, vol. 259, no. 1, pp. 162–172, 2011.

[113] C. Hoeks, J. Barentsz, T. Hambrock, D. Yakar, D. Somford, S. Heijmink, T. Scheenen, P. Vos, H. Huisman, I. van Oort, *et al.*, "Prostate cancer: Multiparametric mr imaging for detection, localization, and staging," *Radiology*, vol. 261, no. 1, pp. 46–66, 2011.

[114] T. Hara, N. Kosaka, H. Kishi, *et al.*, "Pet imaging of prostate cancer using carbon-11-choline.," *Journal of nuclear medicine: official publication, Society of Nuclear Medicine*, vol. 39, no. 6, p. 990, 1998.

[115] M. Picchio, A. Briganti, S. Fanti, A. Heidenreich, B. Krause, C. Messa, F. Montorsi, S. Reske, and G. Thalmann, "The role of choline positron emission tomography/computed tomography in the management of patients with prostate-specific antigen progression after radical treatment of prostate cancer," *European urology*, vol. 59, no. 1, pp. 51–60, 2011.

[116] N. Takahashi, T. Inoue, J. Lee, T. Yamaguchi, and K. Shizukuishi, "The roles of PET and PET/CT in the diagnosis and management of prostate cancer," *Oncology*, vol. 72, no. 3-4, pp. 226–233, 2008.

[117] M. Moman, U. Van Der Heide, A. Kotte, R. Van Moorselaar, G. Bol, S. Franken, and M. Van Vulpen, "Long-term experience with transrectal and transperineal implantations of fiducial gold markers in the prostate for position verification in external beam radiotherapy; feasibility, toxicity and quality of life," *Radiotherapy and Oncology*, vol. 96, no. 1, pp. 38–42, 2010.

[118] C. Hofer, H. Kübler, R. Hartung, J. Breul, and N. Avril, "Diagnosis and monitoring of urological tumors using positron emission tomography.," *European urology*, vol. 40, no. 5, p. 481, 2001.

[119] K. Yu and H. Hricak, "Imaging prostate cancer," *Radiologic Clinics of North America*, vol. 38, no. 1, pp. 59–85, 2000.

[120] B. Porter, D. Rubens, J. Strang, J. Smith, S. Totterman, and K. Parker, "Three-dimensional registration and fusion of ultrasound and mri using major vessels as fiducial markers," *Medical Imaging, IEEE Transactions on*, vol. 20, no. 4, pp. 354–359, 2001.

[121] J. Schlaier, J. Warnat, U. Dorenbeck, M. Proescholdt, K. Schebesch, and A. Brawanski, "Image fusion of MR images and real-time ultrasonography: evaluation of fusion accuracy combining two commercial instruments, a neuronavigation system and a ultrasound system," *Acta Neurochirurgica*, vol. 146, no. 3, pp. 271–277, 2004.

[122] C. Reynier, J. Troccaz, P. Fourneret, A. Dusserre, C. Gay-Jeune, J. Descotes, M. Bolla, and J. Giraud, "MRI/TRUS data fusion for prostate brachytherapy. Preliminary results," *Medical physics*, vol. 31, p. 1568, 2004.

[123] V. Daanen, J. Gastaldo, J. Giraud, P. Fourneret, J. Descotes, M. Bolla, D. Collomb, and J. Troccaz, "Mri/trus data fusion for brachytherapy," *The International Journal of Medical Robotics and Computer Assisted Surgery*, vol. 2, no. 3, pp. 256–261, 2006.

[124] C. Selli, D. Caramella, S. Giusti, A. Conti, A. Tognetti, A. Mogorovich, M. De Maria, and C. Bartolozzi, "Value of image fusion in the staging of prostatic carcinoma," *La Radiologia Medica*, vol. 112, no. 1, pp. 74–81, 2007.

[125] S. Xu, J. Kruecker, P. Guion, N. Glossop, Z. Neeman, P. Choyke, A. Singh, and B. Wood, "Closed-loop control in fused MR-TRUS image-guided prostate

biopsy," in *Proceedings of the 10th international conference on Medical image computing and computer-assisted intervention-Volume Part I*, pp. 128–135, Springer-Verlag, 2007.

[126] S. Kadoury, P. Yan, S. Xu, N. Glossop, P. Choyke, B. Turkbey, P. Pinto, B. Wood, and J. Kruecker, "Realtime trus/mri fusion targeted-biopsy for prostate cancer: a clinical demonstration of increased positive biopsy rates," *Prostate Cancer Imaging. Computer-Aided Diagnosis, Prognosis, and Intervention*, pp. 52–62, 2010.

[127] A. Rastinehad, A. Baccala, P. Chung, J. Proano, J. Kruecker, S. Xu, J. Locklin, B. Turkbey, J. Shih, G. Bratslavsky, *et al.*, "D'Amico Risk Stratification Correlates With Degree of Suspicion of Prostate Cancer on Multiparametric Magnetic Resonance Imaging," *J Urol*, vol. 185, pp. 815–20, 2011.

[128] T. Miyagawa, S. Ishikawa, T. Kimura, T. Suetomi, M. Tsutsumi, T. Irie, M. Kondoh, and T. Mitake, "Real-time virtual sonography for navigation during targeted prostate biopsy using magnetic resonance imaging data," *International journal of urology*, vol. 17, no. 10, pp. 855–860, 2010.

[129] O. Ukimura, N. Hirahara, A. Fujihara, T. Yamada, T. Iwata, K. Kamoi, K. Okihara, H. Ito, T. Nishimura, and T. Miki, "Technique for a hybrid system of real-time transrectal ultrasound with preoperative magnetic resonance imaging in the guidance of targeted prostate biopsy," *International journal of urology*, vol. 17, no. 10, pp. 890–893, 2010.

[130] I. Kaplan, N. Oldenburg, P. Meskell, M. Blake, P. Church, and E. Holupka, "Real time MRI-ultrasound image guided stereotactic prostate biopsy," *Magnetic resonance imaging*, vol. 20, no. 3, pp. 295–299, 2002.

[131] G. Andriole, T. Bullock, J. Belani, E. Traxel, Y. Yan, D. Bostwick, and P. Humphrey, "Is there a better way to biopsy the prostate? prospects for a novel transrectal systematic biopsy approach," *Urology*, vol. 70, no. 6, pp. S22–S26, 2007.

[132] I. Megwalu, G. Ferguson, J. Wei, V. Mouraviev, T. Polascik, S. Taneja, L. Black, G. Andriole, and A. Kibel, "Evaluation of a novel precision template-guided biopsy system for detecting prostate cancer," *BJU international*, vol. 102, no. 5, pp. 546–550, 2008.

[133] S. Taneja, G. Godoy, A. Kibel, D. Penson, and J. Wei, "Prostate cancer detection using a novel computerized three-dimensional prostate biopsy template (targetscan¡sup¿™¡/sup¿): Results of a multicenter prospective data registry," *The Journal of Urology*, vol. 181, no. 4, p. 712, 2009.

[134] M. Baumann, P. Mozer, V. Daanen, and J. Troccaz, "Towards 3d ultrasound image based soft tissue tracking: A transrectal ultrasound prostate image alignment system," *Medical Image Computing and Computer-Assisted Intervention–MICCAI 2007*, pp. 26–33, 2007.

[135] M. Baumann, P. Mozer, V. Daanen, and J. Troccaz, "Prostate biopsy assistance system with gland deformation estimation for enhanced precision," *Medical Image Computing and Computer-Assisted Intervention–MICCAI 2009*, pp. 67–74, 2009.

[136] M. Baumann, P. Mozer, V. Daanen, and J. Troccaz, "Prostate biopsy tracking with deformation estimation," *Medical Image Analysis*, 2011.

[137] O. Ukimura, M. Desai, S. Palmer, S. Valencerina, M. Gross, A. Abreu, M. Aron, and I. Gill, "3-dimensional elastic registration system of prostate biopsy location by real-time 3-dimensional transrectal ultrasound guidance with magnetic resonance/transrectal ultrasound image fusion," *The Journal of Urology*, 2012.

[138] B. Hadaschik, T. Kuru, C. Tulea, P. Rieker, I. Popeneciu, T. Simpfendörfer, J. Huber, P. Zogal, D. Teber, S. Pahernik, *et al.*, "A novel stereotactic prostate biopsy system integrating pre-interventional magnetic resonance imaging and live ultrasound fusion," *The Journal of Urology*, 2011.

[139] J. Bax, D. Cool, L. Gardi, K. Knight, D. Smith, J. Montreuil, S. Sherebrin, C. Romagnoli, and A. Fenster, "Mechanically assisted 3D ultrasound guided prostate biopsy system," *Medical physics*, vol. 35, pp. 5397–410, 2008.

[140] R. Narayanan, P. Werahera, A. Barqawi, E. Crawford, K. Shinohara, A. Simoneau, and J. Suri, "Adaptation of a 3D prostate cancer atlas for transrectal ultrasound guided target-specific biopsy," *Phys Med Biol*, vol. 53, pp. N397–406, 2008.

[141] J. Bax, J. Williams, D. Cool, L. Gardi, J. Montreuil, V. Karnik, S. Sherebrin, C. Romagnoli, and A. Fenster, "Mechanically assisted 3D prostate ultrasound imaging and biopsy needle-guidance system," in *Proceedings of SPIE*, vol. 7625, p. 76252Q, 2010.

[142] D. Cool, J. Bax, C. Romagnoli, A. Ward, L. Gardi, V. Karnik, J. Izawa, J. Chin, and A. Fenster, "Fusion of mri to 3d trus for mechanically-assisted targeted prostate biopsy: system design and initial clinical experience," *Prostate Cancer Imaging. Image Analysis and Image-Guided Interventions*, pp. 121–133, 2011.

[143] L. Marks, A. Ward, L. Gardi, R. Bentley, D. Kumar, S. Gupta, M. Macairan, and A. Fenster, "Tracking of prostate biopsy sites using a 3D ultrasound device (Artemis)," *The Journal of Urology*, vol. 183, no. 4, p. e832, 2010.

[144] F. Cornud, N. Delongchamps, P. Mozer, F. Beuvon, A. Schull, N. Muradyan, and M. Peyromaure, "Value of multiparametric mri in the work-up of prostate cancer," *Current Urology Reports*, pp. 1–11, 2011.

[145] A. Singh, J. Kruecker, S. Xu, N. Glossop, P. Guion, K. Ullman, P. Choyke, and B. Wood, "Initial clinical experience with real-time transrectal ultrasonography-magnetic resonance imaging fusion-guided prostate biopsy," *BJU international*, vol. 101, no. 7, pp. 841–845, 2008.

[146] S. Xu, B. Turkbey, J. Kruecker, P. Yan, J. Locklin, P. Pinto, P. Choyke, and B. Wood, "Multi-parametric MRI-Pathologic correlation of prostate cancer using tracked biopsies," in *Proceedings of SPIE*, vol. 7625, p. 76252R, 2010.

[147] B. Turkbey, S. Xu, J. Kruecker, J. Locklin, Y. Pang, V. Shah, M. Bernardo, A. Baccala, A. Rastinehad, C. Benjamin, *et al.*, "Documenting the location of systematic transrectal ultrasound-guided prostate biopsies: correlation with multi-parametric mri.," *Cancer imaging: the official publication of the International Cancer Imaging Society*, vol. 11, p. 31, 2011.

[148] P. Pinto, P. Chung, A. Rastinehad, A. Baccala Jr, J. Kruecker, C. Benjamin, S. Xu, *et al.*, "Magnetic resonance imaging/ultrasound fusion guided prostate biopsy improves cancer detection following transrectal ultrasound biopsy and correlates with multiparametric magnetic resonance imaging," *The Journal of urology*, 2011.

[149] D. Cool, S. Sherebrin, J. Izawa, J. Chin, and A. Fenster, "Design and evaluation of a 3D transrectal ultrasound prostate biopsy system," *Medical physics*, vol. 35, p. 4695, 2008.

[150] Y. Hu, T. Carter, H. Ahmed, M. Emberton, C. Allen, D. Hawkes, and D. Barratt, "Modelling prostate motion for data fusion during image-guided interventions.," *IEEE transactions on medical imaging*, 2011.

[151] H. Ahmed, Y. Hu, T. Carter, N. Arumainayagam, E. Lecornet, A. Freeman, D. Hawkes, D. Barratt, and M. Emberton, "Characterizing clinically significant prostate cancer using template prostate mapping biopsy," *The Journal of urology*, 2011.

[152] P. Emiliozzi, A. Corsetti, B. Tassi, G. Federico, M. Martini, and V. Pansadoro, "Best approach for prostate cancer detection: a prospective study on transperineal versus transrectal six-core prostate biopsy," *Urology*, vol. 61, no. 5, pp. 961–966, 2003.

[153] R. Hara, Y. Jo, T. Fujii, N. Kondo, T. Yokoyoma, Y. Miyaji, and A. Nagai, "Optimal approach for prostate cancer detection as initial biopsy: prospective randomized study comparing transperineal versus transrectal systematic 12-core biopsy," *Urology*, vol. 71, no. 2, pp. 191–195, 2008.

[154] J. Barentsz, J. Richenberg, R. Clements, P. Choyke, S. Verma, G. Villeirs, O. Rouviere, V. Logager, and J. Fütterer, "Esur prostate mr guidelines 2012," *European Radiology*, pp. 1–12, 2012.

[155] J. I. Epstein, P. C. Walsh, M. Carmichael, and C. B. Brendler, "Pathologic and clinical findings to predict tumor extent of nonpalpable (stage t1c) prostate cancer," *JAMA*, vol. 271, no. 5, pp. 368–74, 1994. Epstein, J I Walsh, P C Carmichael, M Brendler, C B United states JAMA : the journal of the American Medical Association JAMA. 1994 Feb 2;271(5):368-74.

[156] P. Tofts, G. Brix, D. Buckley, J. Evelhoch, E. Henderson, M. Knopp, H. Larsson, T. Lee, N. Mayr, G. Parker, *et al.*, "Estimating kinetic parameters from dynamic contrast-enhanced t 1-weighted mri of a diffusable tracer: standardized quantities and symbols," *Journal of Magnetic Resonance Imaging*, vol. 10, no. 3, pp. 223–232, 1999.

[157] A. Rosset, L. Spadola, and O. Ratib, "OsiriX: an open-source software for navigating in multidimensional DICOM images," *J Digit Imag*, vol. 17, no. 3, pp. 205–16, 2004.

[158] V. Kumar, N. Jagannathan, R. Kumar, S. Thulkar, S. Gupta, A. Hemal, and N. Gupta, "Transrectal ultrasound-guided biopsy of prostate voxels identified as suspicious of malignancy on three-dimensional 1h mr spectroscopic imaging in patients with abnormal digital rectal examination or raised prostate specific antigen level of 4–10 ng/ml," *NMR in Biomedicine*, vol. 20, no. 1, pp. 11–20, 2007.

[159] K. Shigemura, S. Motoyama, and M. Yamashita, "Do additional cores from mri cancer-suspicious lesions to systematic 12-core transrectal prostate biopsy give better cancer detection?," *Urologia internationalis*, 2012.

[160] D. Shen and C. Davatzikos, "An adaptive-focus deformable model using statistical and geometric information," *Pattern Analysis and Machine Intelligence, IEEE Transactions on*, vol. 22, no. 8, pp. 906–913, 2000.

[161] D. Shen, E. Herskovits, and C. Davatzikos, "An adaptive-focus statistical shape model for segmentation and shape modeling of 3-d brain structures," *Medical Imaging, IEEE Transactions on*, vol. 20, no. 4, pp. 257–270, 2001.

[162] R. Narayanan, J. Kurhanewicz, K. Shinohara, E. Crawford, A. Simoneau, and J. Suri, "MRI-ultrasound registration for targeted prostate biopsy," *IEEE Intl Symp Biomed Imag 2009*, pp. 991–994, 2009.

[163] V. Karnik, A. Fenster, J. Bax, D. Cool, L. Gardi, I. Gyacskov, C. Romagnoli, and A. Ward, "Assessment of image registration accuracy in three-dimensional transrectal ultrasound guided prostate biopsy," *Med Phys*, vol. 37, pp. 802–13, 2010.

[164] V. Karnik, A. Fenster, J. Bax, D. Cool, L. Gardi, I. Gyacskov, C. Romagnoli, and A. Ward, "Assessment of registration accuracy in three-dimensional transrectal ultrasound images of prostates," in *Proceedings of SPIE*, vol. 7625, p. 762516, 2010.

[165] P. Langfelder and S. Horvath, "Wgcna: an r package for weighted correlation network analysis," *BMC bioinformatics*, vol. 9, no. 1, p. 559, 2008.

[166] J. Silletti, G. Gordon, R. Bueno, M. Jaklitsch, and K. Loughlin, "Prostate biopsy: past, present, and future," *Urology*, vol. 69, no. 3, pp. 413–416, 2007.

[167] B. Djavan, V. Ravery, A. Zlotta, P. Dobronski, M. Dobrovits, M. Fakhari, C. Seitz, M. Susani, A. Borkowski, L. Boccon-Gibod, *et al.*, "Prospective evaluation of prostate cancer detected on biopsies 1, 2, 3 and 4: when should we stop?," *The Journal of urology*, vol. 166, no. 5, pp. 1679–1683, 2001.

[168] O. Zaytoun and J. Jones, "Prostate cancer detection after a negative prostate biopsy: Lessons learnt in the cleveland clinic experience," *International Journal of Urology*, 2011.

[169] H. Fukuhara, "Editorial comment to prostate cancer detection after a negative prostate biopsy: Lessons learnt in the cleveland clinic experience," *International Journal of Urology*, 2011.

[170] T. Wolters, M. Roobol, P. Van Leeuwen, R. Van Den Bergh, R. Hoedemaeker, G. Van Leenders, F. Schröder, and T. Van Der Kwast, "A critical analysis of the tumor volume threshold for clinically insignificant prostate cancer using a data set of a randomized screening trial," *The Journal of urology*, vol. 185, no. 1, pp. 121–125, 2011.

[171] W. van de Ven, G. Litjens, J. Barentsz, T. Hambrock, and H. Huisman, "Required accuracy of mr-us registration for prostate biopsies," *Prostate Cancer Imaging. Image Analysis and Image-Guided Interventions*, pp. 92–99, 2011.

[172] H. Ahmed, M. Emberton, G. Kepner, and J. Kepner, "A biomedical engineering approach to mitigate the errors of prostate biopsy," *Nature Reviews Urology*, 2012.

[173] Y. Hu, H. Ahmed, T. Carter, N. Arumainayagam, E. Lecornet, W. Barzell, A. Freeman, P. Nevoux, D. Hawkes, A. Villers, *et al.*, "A biopsy simulation study to assess the accuracy of several transrectal ultrasonography (trus)-biopsy strategies compared with template prostate mapping biopsies in patients who have undergone radical prostatectomy," *BJU international*, 2012.

[174] G. Kepner and J. Kepner, "Transperineal prostate biopsy: analysis of a uniform core sampling pattern that yields data on tumor volume limits in negative biopsies," *Theoretical Biology and Medical Modelling*, 2010.

[175] D. Cool, M. Connolly, S. Sherebrin, R. Eagleson, J. Izawa, J. Amann, C. Romagnoli, W. Romano, and A. Fenster, "Repeat Prostate Biopsy Accuracy: Simulator-based Comparison of Two-and Three-dimensional Transrectal US Modalities1," *Radiology*, vol. 254, no. 2, p. 587, 2010.

[176] D. Chang, C. Kim, H. Kim, D. Petrisor, M. Han, and D. Stoianovici, "Measurement of spatial distribution in sextant prostate biopsy," *Journal of Endourology*, vol. 25, no. 9, p. 37, 2011.

[177] S. Natarajan, L. Marks, D. Margolis, J. Huang, M. Macairan, P. Lieu, and A. Fenster, "Clinical application of a 3d ultrasound-guided prostate biopsy system," *Urologic Oncology*, vol. 29, no. 3, pp. 334–342, 2011.

[178] B. Turkbey, V. Shah, Y. Pang, M. Bernardo, S. Xu, J. Kruecker, J. Locklin, A. Baccala, A. Rastinehad, M. Merino, *et al.*, "Is apparent diffusion coefficient associated with clinical risk scores for prostate cancers that are visible on 3-t mr images?," *Radiology*, vol. 258, no. 2, pp. 488–495, 2011.

[179] M. So, S. Haker, K. Zou, A. Barnes, R. Cormack, J. Richie, A. D'Amico, and C. Tempany, "Clinical evaluation of mr-guided prostate biopsy," in *ISMRM 13th Scientific Meeting and Exhibition*, p. 264, 2005.

[180] C. Tempany, S. Straus, N. Hata, and S. Haker, "MR-guided prostate interventions," *Journal of Magnetic Resonance Imaging*, vol. 27, no. 2, pp. 356–367, 2008.

[181] L. Dickinson, H. Ahmed, C. Allen, J. Barentsz, B. Carey, J. Futterer, S. Heijmink, P. Hoskin, A. Kirkham, A. Padhani, *et al.*, "Magnetic resonance imaging for the detection, localisation, and characterisation of prostate cancer: recommendations from a european consensus meeting," *European urology*, 2010.

[182] N. Delongchamps, F. Beuvon, D. Eiss, T. Flam, N. Muradyan, M. Zerbib, M. Peyromaure, and F. Cornud, "Multiparametric mri is helpful to predict tumor focality, stage, and size in patients diagnosed with unilateral low-risk prostate cancer," *Prostate Cancer and Prostatic Diseases*, vol. 14, no. 3, pp. 232–237, 2011.

[183] B. Turkbey, H. Mani, V. Shah, A. Rastinehad, M. Bernardo, T. Pohida, Y. Pang, D. Daar, C. Benjamin, Y. McKinney, *et al.*, "Multiparametric 3t prostate magnetic resonance imaging to detect cancer: Histopathological correlation using prostatectomy specimens processed in customized magnetic resonance imaging based molds," *The Journal of Urology*, 2011.

[184] B. Weiss, A. Wein, S. Malkowicz, and T. Guzzo, "Comparison of prostate volume measured by transrectal ultrasound and magnetic resonance imaging: Is transrectal ultrasound suitable to determine which patients should undergo active surveillance?," in *Urologic Oncology: Seminars and Original Investigations*, Elsevier, 2012.

[185] A. Ayvaci, P. Yan, S. Xu, S. Soatto, and J. Kruecker, "Biopsy needle detection in transrectal ultrasound," *Computerized Medical Imaging and Graphics*, 2011.

[186] T. De Silva, A. Fenster, J. Bax, C. Romagnoli, J. Izawa, J. Samarabandu, and A. Ward, "Quantification of prostate deformation due to needle insertion during trus-guided biopsy: Comparison of hand-held and mechanically stabilized systems," *Medical Physics*, vol. 38, p. 1718, 2011.

[187] H. Holm, A. Northeved, *et al.*, "A transurethral ultrasonic scanner.," *The Journal of urology*, vol. 111, no. 2, p. 238, 1974.

[188] J. Gammelgaard, H. Holm, *et al.*, "Transurethral and transrectal ultrasonic scanning in urology.," *The Journal of urology*, vol. 124, no. 6, p. 863, 1980.

[189] Y. Komine, A. Kimura, M. Niizuma, S. Nakamura, K. Kawabe, and T. Niijima, "Transurethral ultrasonotomography of the prostate," *The Prostate*, vol. 2, no. S1, pp. 53–57, 1981.

[190] H. Watanabe, D. Igari, Y. Tanahashi, K. Harada, and M. Saitoh, "Transrectal ultrasonotomography of the prostate," *The Journal of urology*, vol. 114, no. 5, p. 734, 1975.

[191] M. Devonec, J. Chapelon, H. Codas, J. Dubernard, J. Revillard, and D. Cathignol, "Evaluation of bladder cancer with a miniature high frequency transurethral ultrasonography probe," *British journal of urology*, vol. 59, no. 6, pp. 550–553, 1987.

[192] M. Resnick and E. Kursh, "Transurethral ultrasonography of the urinary bladder," *World Journal of Urology*, vol. 6, no. 1, pp. 22–26, 1988.

[193] S. Schulze, A. Holm-Nielsen, and P. Mogensen, "Transurethral ultrasound scanning in the evaluation of invasive bladder cancer.," *Scandinavian journal of urology and nephrology*, vol. 25, no. 3, p. 215, 1991.

[194] M. Koraitim, B. Kamal, N. Metwalli, and Y. Zaky, "Transurethral ultrasonographic assessment of bladder carcinoma: its value and limitation," *The Journal of urology*, vol. 154, no. 2, pp. 375–378, 1995.

[195] K. Nishimura, S. Hida, Y. Nishio, K. Ohishi, Y. Okada, K. Okada, O. Yoshida, K. Nishimura, and S. Nishibuchi, "The validity of magnetic resonance imaging (mri) in the staging of bladder cancer: Comparison with computed tomography (ct) and transurethral ultrasonography (us)," *Japanese Journal of Clinical Oncology*, vol. 18, no. 3, p. 217, 1988.

[196] H. Strasser, F. Frauscher, G. Helweg, K. Colleselli, A. Reissigl, and G. Bartsch, "Transurethral ultrasound: evaluation of anatomy and function of the rhabdosphincter of the male urethra," *The Journal of urology*, vol. 159, no. 1, pp. 100–105, 1998.

[197] R. Kirschner-Hermanns, H. Klein, U. M
"uller, W. Sch
"afer, and G. Jakse, "Intra-urethral ultrasound in women with stress incontinence.," *British journal of urology*, vol. 74, no. 3, p. 315, 1994.

[198] D. Holmes III, B. Davis, C. Bruce, T. Wilson, and R. Robb, "Transurethral ultrasound of the prostrate for applications in prostrate brachytherapy: analysis of phantom and in-vivo data," in *Proceedings of SPIE*, vol. 4319, p. 46, 2001.

[199] M. Mitterberger, G. Pinggera, T. Mueller, F. Frauscher, L. Pallwein, J. Gradl, R. Peschel, G. Bartsch, and H. Strasser, "Dynamic transurethral sonography and 3-dimensional reconstruction of the rhabdosphincter and urethra," *Journal of ultrasound in medicine*, vol. 25, no. 3, pp. 315–320, 2006.

[200] S. Matin, A. Kamat, and H. Grossman, "High-frequency endoluminal ultrasonography as an aid to the staging of upper tract urothelial carcinoma: imaging findings and pathologic correlation.," *Journal of ultrasound in medicine: official journal of the American Institute of Ultrasound in Medicine*, vol. 29, no. 9, p. 1277, 2010.

[201] A. Shkel, S. Natarajan, S. Schimpf, M. Culjat, A. Brose, A. Boese, B. Schmidt, P. Schulam, H. Lee, W. Grundfest, *et al.*, "A transurethral catheter-based ultrasound system for multi-modal fusion.," *Studies in health technology and informatics*, vol. 173, p. 463, 2012.

[202] N. Bom, H. Ten Hoff, C. Lancee, W. Gussenhoven, and J. Bosch, "Early and recent intraluminal ultrasound devices," *The International Journal of Cardiac Imaging*, vol. 4, no. 2, pp. 79–88, 1989.

[203] E. Light, R. Davidsen, J. Fiering, T. Hruschka, and S. Smith, "Progress in two-dimensional arrays for real-time volumetric imaging," *Ultrasonic Imaging*, vol. 20, no. 1, pp. 1–16, 1998.

[204] J. Liu and B. Goldberg, "Catheter-based intraluminal sonography," *Journal of Ultrasound in Medicine*, vol. 23, no. 2, pp. 145–160, 2004.

[205] R. Martin and C. Johnson, "Design characteristics for intravascular ultrasonic catheters," *The International Journal of Cardiac Imaging*, vol. 4, no. 2, pp. 201–216, 1989.

[206] J. Tardif, O. Bertrand, R. Mongrain, J. Lespérance, J. Grégoire, P. Paiement, and R. Bonan, "Reliability of mechanical and phased-array designs for serial intravascular ultrasound examinations," *The International Journal of Cardiac Imaging*, vol. 16, no. 5, pp. 365–375, 2000.

[207] B. Kimura, V. Bhargava, W. Palinski, R. Russo, and A. DeMaria, "Distortion of intravascular ultrasound images because of nonuniform angular velocity of mechanical-type transducers," *American heart journal*, vol. 132, no. 2, pp. 328–336, 1996.

[208] M. O'Donnell and L. Thomas, "Efficient synthetic aperture imaging from a circular aperture with possible application to catheter-based imaging.," *IEEE transactions on ultrasonics, ferroelectrics, and frequency control*, vol. 39, no. 3, p. 366, 1992.

[209] S. Nissen and P. Yock, "Intravascular ultrasound: novel pathophysiological insights and current clinical applications," *Circulation*, vol. 103, no. 4, pp. 604–616, 2001.

[210] G. Rodriguez-Granillo, E. Fadden, J. Aoki, C. van Mieghem, E. Regar, N. Bruining, and P. Serruys, "In vivo variability in quantitative coronary ultrasound and tissue characterization measurements with mechanical and phased-array catheters," *The International Journal of Cardiovascular Imaging (formerly Cardiac Imaging)*, vol. 22, no. 1, pp. 47–53, 2006.

[211] S. O'Malley, J. Granada, S. Carlier, M. Naghavi, and I. Kakadiaris, "Image-based gating of intravascular ultrasound pullback sequences," *Information Technology in Biomedicine, IEEE Transactions on*, vol. 12, no. 3, pp. 299–306, 2008.

[212] M. Tanabe, S. Xie, N. Tagawa, and T. Moriya, "Driving the coiled stator ultrasonic motor using traveling wave generated by superimposing two standing waves," *Japanese Journal of Applied Physics*, vol. 47, p. 4262, 2008.

[213] M. Grasso, J. Liu, B. Goldberg, and D. Bagley, "Submucosal calculi: endoscopic and intraluminal sonographic diagnosis and treatment options," *The Journal of urology*, vol. 153, no. 5, pp. 1384–1389, 1995.

[214] D. Bagley and J. Liu, "Three-dimensional endoluminal ultrasonography of the ureter," *Journal of endourology/Endourological Society*, vol. 12, no. 5, p. 411, 1998.

[215] K. Horiuchi, N. Tsuboi, H. Shimizu, I. Matsuzawa, G. Kimura, K. Yoshida, and M. Akimoto, "High-frequency endoluminal ultrasonography for staging transitional cell carcinoma of the bladder," *Urology*, vol. 56, no. 3, pp. 404–407, 2000.

[216] D. Holmes III and R. Robb, "Trans-urethral ultrasound (tuus) imaging for visualization and analysis of the prostate and associated tissues," in *Proceedings of SPIE*, vol. 3976, p. 22, 2000.

[217] D. Holmes, *Trans-urethral Catheter-based Ultrasound Image Acquisition, Processing and Visualization for Applications in the Prostate*. PhD thesis, Biomedical Sciences–Biomedical Imaging–Mayo Graduate School, 2002.

[218] D. Holmes, B. Davis, C. Bruce, and R. Robb, "3d visualization, analysis, and treatment of the prostate using trans-urethral ultrasound," *Computerized medical imaging and graphics*, vol. 27, no. 5, pp. 339–349, 2003.

[219] D. Holmes III and R. Robb, "Improved automated brachytherapy seed localization in trans-urethral ultrasound data," in *Proceedings of SPIE*, vol. 5367, p. 353, 2004.

[220] N. Bom, C. Lancee, and F. Van Egmond, "An ultrasonic intracardiac scanner," *Ultrasonics*, vol. 10, no. 2, pp. 72–76, 1972.

[221] J. Hodgson, S. Graham, A. Savakus, S. Dame, D. Stephens, P. Dhillon, D. Brands, H. Sheehan, and M. Eberle, "Clinical percutaneous imaging of coronary anatomy using an over-the-wire ultrasound catheter system," *The International Journal of Cardiac Imaging*, vol. 4, no. 2, pp. 187–193, 1989.

[222] M. O'Donnell, B. Shapo, M. Eberle, and D. Stephens, "Experimental studies on an efficient catheter array imaging system.," *Ultrasonic imaging*, vol. 17, no. 2, p. 83, 1995.

[223] M. O'Donnell, M. Eberle, D. Stephens, J. Litzza, K. San Vicente, and B. Shapo, "Synthetic phased arrays for intraluminal imaging of coronary arteries," *Ultrasonics, Ferroelectrics and Frequency Control, IEEE Transactions on*, vol. 44, no. 3, pp. 714–721, 2002.

[224] J. Huber, Q. Peng, and W. Moses, "Multi-modality phantom development," *Nuclear Science, IEEE Transactions on*, vol. 56, no. 5, pp. 2722–2727, 2009.

[225] M. Culjat, A. Dann, M. Lee, D. Bennett, P. Schulam, H. Lee, W. Grundfest, and R. Singh, "Transurethral ultrasound catheter-based transducer with flexible polyimide joints," in *Ultrasonics Symposium (IUS), 2009 IEEE International*, pp. 2209–2212, IEEE, 2009.

[226] M. O. Culjat, R. S. Singh, C. D. Utley, S. P. Vampola, B. Sharareh, H. Lee, E. R. Brown, and W. S. Grundfest, "A flexible, conformal ultrasound array for medical imaging," *Studies in Health TechnoI. and Inf.*, vol. 132, pp. 95–97, 2008.

[227] M. Lee, R. Singh, M. Culjat, S. Natarajan, B. Cox, E. Brown, W. Grundfest, and H. Lee, "Space-time image reconstruction algorithm for diverse ultrasound transducer element distributions," in *Biomedical Imaging: From Nano to Macro, 2009. ISBI'09. IEEE International Symposium on*, pp. 177–180, IEEE, 2009.

[228] S. Natarajan, R. Singh, M. Lee, B. Cox, M. Culjat, W. Grundfest, and H. Lee, "Accurate step-fmcw ultrasound ranging and comparison with pulse-echo signaling methods," in *Proceedings of SPIE*, vol. 7629, p. 76290D, 2010.

[229] S. Natarajan, R. Singh, M. Lee, B. Cox, M. Culjat, H. Lee, and W. Grundfest, "Step-fmcw signaling and target detection for ultrasound imaging systems with conformal transducer arrays," in *Proceedings of SPIE*, vol. 7555, p. 75550M, 2010.

[230] U. Lindner, N. Lawrentschuk, R. Weersink, S. Davidson, O. Raz, E. Hlasny, D. Langer, M. Gertner, T. Van der Kwast, M. Haider, *et al.*, "Focal laser ablation for prostate cancer followed by radical prostatectomy: validation of focal therapy and imaging accuracy," *European urology*, vol. 57, no. 6, pp. 1111–1114, 2010.

[231] E. Lecornet, C. Moore, H. Ahmed, and M. Emberton, "Focal therapy for prostate cancer: Fact or fiction?," *Urologic Oncology*, vol. 28, no. 5, pp. 550–556, 2010.

[232] H. Ahmed, *Focal Therapy in Prostate Cancer*. Wiley-Blackwell, 2012.